Determination of the fracture strength of brittle material thin films at high temperature using MEMS

by

Alex Axel Navarrete Gonzalez

A thesis
presented to the University of Waterloo
in fulfillment of the
thesis requirement for the degree of
Doctor of Philosophy
in
Mechanical and Mechatronics Engineering

Waterloo, Ontario, Canada, 2019

Examining Committee Membership

The following served on the Examining Committee for this thesis. The decision of the Examining Committee is by majority vote.

External Examiner	NAME	Dr. Peter Schiavone
	Title	Professor
Supervisor(s)	NAME	Dr. Patricia Nieva
	Title	Professor
Internal Member	NAME	Dr. Clifford Butcher
	Title	Assistant Professor
Internal Member	NAME	Dr. Eihab Abdel-Rahman
	Title	Professor
Internal-external Member	NAME	Dr. Stanislav Potapenko
	Title	Associate Professor

AUTHOR'S DECLARATION

This thesis consists of material all of which I authored or co-authored: see Statement of Contributions included in the thesis. This is a true copy of the thesis, including any required final revisions, as accepted by my examiners.

I understand that my thesis may be made electronically available to the public.

Statement of contributions

This thesis contains fragments of a previously published manuscripts. Chapters 3 and 5 contain fragments of this manuscript:

Published:

- A. N. Gonzalez, E. Brace, and P. Nieva, "Size and Shape Effect in the Determination of the Fracture Strength of Silicon Nitride in MEMS Structures at High Temperatures," in 2018 IEEE 68th Electronic Components and Technology Conference (ECTC), 2018, pp. 2457–2463.

A. Navarrete wrote this manuscript with support of E. Brace in the analytical modeling of the silicon nitride MEMS structures. A. Navarrete processd experimental data and performed the analysis for the fracture strength determination of silicon nitride thin films and the probabilistic analysis of the fracture data. A Navarrete designed figures 1 – 4 with the support of E. Brace. A. Navarrete worked on the analytical modeling of the equations used to study the fracture strength with the support of E. Brace. Dr. P. Nieva supervised the project

Abstract

Brittle materials are widely used as structural materials in microelectromechanical systems (MEMS). Their mechanical properties make them suitable for high-temperature environments where MEMS are exposed to different types of failure modes such as fractures and fast aging. A fracture happens when the material splits into two or more pieces due to exceeding the material's maximum strength. High temperature accelerates fracture in materials leading to premature failure due to crack growth. Thus, it is crucial to understand the relationship between temperature and fracture strength in MEMS materials. Researchers have measured fracture strength for brittle materials using different structures and methodologies, but there is still not a standard accepted methodology to measure it in microstructures.

In this research, a new methodology using MEMS devices to determine fracture strength at high temperatures is developed. The methodology is designed to address three significant aspects that are currently a drawback in MEMS fracture strength testing. The first aspect is the simplicity of the test setup. The methodology reduces sources of error and variables involved in the measurement of the fracture strength using stress due to thermal mismatch. The tested structures are designed using a silicon substrate and a silicon nitride thin film directly deposited onto the substrate. The thin film is patterned into a suspended dog-bone shaped bridge and it has a stress concentration section right in the middle of the bridge. The coefficient of thermal expansion (CTE) mismatch between the materials provides the stress to break the thin film as the materials expand due to the temperature change. By applying stress directly to the device, a test setup composed of a reduced amount of elements is implemented, which makes the experiment accessible and straightforward for its replication. The second aspect is the speed of the test methodology. The stress concentration section makes it possible for the thin film to fracture in minutes as the temperature is increased. Increasing or decreasing the ramping of the temperature controls the speed of the test and opens the possibility for this methodology to be accelerated. The third aspect is the number of samples that are tested at the same time. The

structures providing their stress allow for the testing of several devices arrays at a time, where each device will break as the temperature is increased.

The material tested in this study a silicon nitride thin film deposited using low-pressure chemical vapor deposition (CVD), which is patterned into three different shapes with different lengths to test the effect of geometry variation in the fracture strength. During testing, the temperature of the devices was increased from room temperature to 1000 °C using a furnace with a ramp of 98 °C/minute for 10 minutes. The breaking temperature of each device was recorded during the experiment with its respective length and shape. The fracture strength is determined using finite element analysis (FEA) in COMSOL multi-physics for the devices of each shape. The FEA study models the behavior of the structures as the temperature increases and simulates the stress up to the breaking temperature of the device, which is recorded at the concentration section of the thin film. The fracture changed from 0.24 GPa to 2.84 GPa for devices of shape #1, from 0.26 GPa to 2.98 GPa for devices of shape #2 and from 0.22 GPa to 2.1 GPa for devices of shape #3. These values are used to plot the fracture strength of the thin film as a function of temperature. A Weibull statistical approach used to determine the probability of failure of the material predicted ~80% at stresses ranging from 0.37 GPa to 0.44 GPa. From the results, it is concluded that although there is an effect from the geometry, it is secondary to the impact the temperature has on the fracture strength. As for the increasing fracture strength as temperature rises, this is attributed to the deformation of the silicon substrate attenuating the effect of the CTE mismatch, which is not accounted for in the current simulation setup.

The analytical model used to determine the fracture strength of each device was constructed from the displacement on the thin film due to the stress and the influence of temperature and geometry change in the material properties of the material. The experimental data is used as input and the plotted results show a similar trend as the one observed for the simulation results.

The data follows exponential growth for every shape at 400 °C when a decrease in the fracture strength is expected. The fracture changed from 0.704 GPa to 6.48 GPa for devices of shape #1, from 0.838 GPa to 9.54 GPa for devices of shape #2 and from 0.764 GPa to 7.5 GPa for devices of shape #3. Although the trend matched in both analytical and FEA simulation with the exponential growth of the fracture strength, the magnitudes showed a discrepancy. The reasons for the differences are mainly due to the significance given to the geometry change of the film in the analytical model, which is shown by how the only shape that is not symmetrical has a remarkably increased value of fracture strength compared to the other two shapes. It is also essential to have in mind that the analytical model is constructed based on a uniaxial model, while the FEA simulation does consider the stress the device is submitted to from every direction.

Lastly, this work presents an improved methodology, which incorporates additional structures to characterize material properties for the thin film material that are involved in the fracture strength determination. All the structures are fabricated together using the same process to produce a high-temperature MEMS testing chip. The varying parameters of the first tested structures is reduced by decreasing the geometrical variation of the different shapes. From the previous results, the need to monitor strain throughout the experiment is determined. The new devices implement the deposition of metallic markers near a stress concentration section for optical measurements, which are used to monitor the strain of the thin films. Measuring the strain allows for the incorporation of the creep effect in the involved materials and understand its interaction with the fracture. The strain is also useful as an indicator of thermal buckling or deformation in the substrate. Hence, the presented work paves the way for future research that will improve the testing of fracture strength on brittle thin films for MEMS devices. Based on the knowledge acquired, the new proposed devices will be of great help to understand the relationship between temperature and the mechanics of materials as well as to perform rapid testing materials at high temperatures.

Acknowledgments

I want to thank Dr. Patricia Nieva for her fruitful guidance and continued support. Additionally, I would like to thank the thesis examining committee Dr. Stanislav Potapenko, Dr. Clifford Butcher, Dr. Eihab Abdel-Rahman, and Dr. Peter Schiavone, for their contributions and support through this valuable process.

I want to thank the University of Waterloo for providing an excellent environment for leading minds to work together. I want to thank the exceptional institutions within the university that helped me get to this point in my academic career, such as the SimsLab, the CIRFE, and the Giga-to Nanoelectronics Centre. Among the remarkable people that helped me through this journey, I would like to thank Dr. Luis Gutierrez, Dr. Czang-Ho Lee, Richard Barber, Krishna Iyer, Dr. AbdulRahman Ghannoum, Eric Brace, Dr. Ali Najafi Sohi, and many others. I would also like to thank my friends for their support and wish them all a bright future.

Finally, I would like to thank my mother, Magali Gonzalez, for the support and love that she has given me since my birth. I would also like to thank my siblings, Isaias Navarrete and Magali Navarrete, for their valuable advice and love. Lastly, I would like to thank my cousins Jorge Mireles and Rolando Mireles and his family for being there during difficult times.

This work was partly financially supported by the “Consejo Nacional de Ciencia y Tecnologia” (CONACYT).

Table of Contents

List of Figures

List of Tables

List of Abbreviations

MEMS	Micro Electromechanical Systems
FEA	Finite Element Analysis
Si	Silicon
CTE	Coefficient of Thermal Expansion
Si_3N_4	Silicon Nitride
PolySi	Polysilicon
SiC	Silicon Carbide
IC	Integrated Circuits
Cu	Copper
Ni	Nickel
BDT	Brittle to Ductile Transition
SCS	Single Crystal Silicon
XRD	X-Ray Diffraction
SEM	Scanning Electron Microscope
Al	Aluminum
Zn	Zinc
GBS	Grain Boundary Sliding
Si_xN_y	Rich Silicon Nitride
LPCVD	Low-Pressure Chemical Vapor Deposition
TMAH	Tetramethylammonium hydroxide
CAD	Computer Assisted Design
BC	Boundary Conditions
ISDG	Interferometric Strain\Displacement Gage
RCA	Radio Corporation America

UV	Ultraviolet
DRIE	Deep Reaction Ion Etching
PECVD	Plasma-enhanced Chemical Vapor Deposition
CMP	Chemical Mechanical Polishing
RIE	Reactive Ion Etching
HF	Hydrofluoric Acid

List of Symbols

P_f	Probability distribution function
σ_0	Weibull characteristic life
γ	Weibull location
m	Weibull dispersion of data
r	Residual from the linear Weibull fitting
$\dot{\varepsilon}$	Creep strain rate
ε	Strain
t	Time
$\dot{\varepsilon}_{primary}$	Primary creep strain rate
A	Primary creep experimental constant
n	Primary creep experimental constant
α	Logarithmic creep constant
ε_0	Initial strain
β	Primary creep strain rate decrease constant
m	Andrade's exponent
$\dot{\varepsilon}_{secondary}$	Secondary creep strain rate
B	Secondary creep material constant
η	Secondary creep exponent
R	Gas constant
Q	Creep activation energy
T	Temperature
$t_{tertiarycreep}$	Time for tertiary creep to happen
t_r	Rupture time
C	Empirical tertiary creep material constant

μ	Empirical tertiary creep material constant
σ	Stress
L	Length
W	Width
L_{Gage}	Length of the bridge's gage
W_{Gage}	Width of the bridge's gage
CTE_{Si}	Coefficient of thermal expansion of silicon
$CTE_{Si_xN_y}$	Coefficient of thermal expansion of silicon nitride
E_{Si}	Young's modulus of silicon
k_B	Boltzmann Constant
$E_{Si_xN_y}$	Young's modulus of silicon nitride
E_0	Young's modulus at high temperature
ε_{Total}	Total strain
$\varepsilon_{Mechanical}$	Mechanical strain
$\varepsilon_{Thermal}$	Thermal strain
σ_{Film}	Stress on the thin film bridge
E_{Film}	Young's modulus of the thin film
ε_{Thfilm}	The thermal strain of the thin film
ε_{ThSubs}	The thermal strain of the substrate
F	Distributed force through the thin film
$A(x)$	The variable cross-sectional area of the thin film
α_{Film}	Coefficient of thermal expansion of the thin film
α_{Subs}	Coefficient of thermal expansion of the substrate
T_0	Initial temperature
b	Y-axis distance between the radius of tangency and the gage center

h	Length of the flat segment of the width of the thin film bridge
$f(x)$	Variable width of the thin film bridge
$f1\ to\ f5$	Functions that describe each geometry of the width of the thin film
r_a	The radius of the outside edge of the thin film bridge
x	Position on the x-axis of the thin film bridge
σ_{Max}	Maximum stress at gage section
σ_{Fr}	Fracture strength
σ_{res}	Residual stress
I	Laser intensity
I_0	Initial laser intensity
β_0	ISDG diffraction variable
b	Marker width
λ	Wavelength
θ	Diffraction angle
γ_1	ISDG interference variable
d	Distance between reflective markers
$\Delta\varphi$	Interferometric fringes phase shift
d_0	Reflective markers initial separation distance
R	Reflection
k	Extinction coefficient
m_0	Interference integral number
n_{mat}	Refractive index of the material
$\theta_{incidentbeam}$	Laser beam incident angle
d_n	Distance between the reflective markers from the center to center
f_n	Distance between the reflective markers from their furthest edge

w_n	Width of the second gage section
D	Distance between the markers and the optical sensors
x	Percentage resolution of the optical system
ρ	Density
$t_{cantilever}$	Cantilever beam thickness
f	Resonant frequency

Chapter 1
Introduction

1.1 Motivation

Microelectromechanical systems (MEMS) are widely used due to their size and unique properties, which are beneficial for a wide range of applications. As the MEMS fabrication technologies and their integration to several industries increase, more industries seek in MEMS a solution for their sensing needs, which include high-temperature applications. Industries such as automotive, space, oil, mining, among others, would improve their existing high-temperature processes with the implementation of MEMS. In particular, silicon (Si) based MEMS, which is a brittle material, would improve their cost and efficiency. Brittle material MEMS devices like accelerometers, pressure sensors, gyroscopes, among others, have been fabricated at micro scales. Thus, making Si be the most worldwide known material to work in MEMS at a reasonable cost and high functionality. However, high temperature affects the mechanical and electrical properties of MEMS, which is a hurdle for the use of these devices at a bigger scale in these environments. Young's modulus, coefficient of thermal expansion (CTE) and fracture strength of the material are some examples of properties vulnerable to the effect of temperature. To be able to produce lasting and reliable brittle material MEMS for these environments, knowing how these properties change with temperature is fundamental, thus, it is crucial to design methodologies to study these effects. From the mentioned properties, fracture strength is of very high importance when developing a new device. When a device fractures it becomes unusable and has to be replaced, thus, the fracture strength is an indicator of the device's life cycle. Existing methodologies to determine fracture strength in the microscale use highly customized approaches to quantify it, which are hard to replicate. More straightforward test methodologies that can be widely replicated by different research facilities are a need for micro materials. This research is motivated to design the foundations of a simple yet reliable testing methodology to determine fracture strength at high temperatures in MEMS brittle materials. The methodology is adaptable to different materials and variable temperatures while being repeatable. The methodology aims to solve the current shortcomings of micro materials tensile testing, which include handling of specimens, data points obtained per test and repeatability. The early stages of the methodology are developed in this research

and a roadmap for the future steps are laid out for its improvement.

1.2 Objectives

The objective of this project is the design of a testing methodology to measure the fracture strength of thin films at high temperatures. This research allows for a better understanding of the relationship between temperature and the variation of material properties. The fracture strength of the material is profoundly affected by temperature, thus adequate methodologies that facilitate the quantification of this effect. The objectives of this research can be divided into two sections, proof of concept and the improvement of the proposed methodology. The goals include:

- Adaptation of an array of MEMS devices for high-temperature testing.
- To achieve the accelerated testing of several devices in one experimental run.
- To develop a finite element model of the experiment to determine the fracture strength of the thin film.
- The effect of geometry and temperature in the fracture strength of materials is investigated.
- An analytical model describes the mechanical interaction in the MEMS devices exposed to high temperatures.
- The conclusions from the comparison of the analytical and simulated results are used to propose modifications in the devices and test methodology to obtain results that match the literature used as a reference.
- The proposed modifications are implemented in the device design.

1.3 Organization of thesis

In chapter 1, the motivation of this study and the objectives of this research are presented. The contents of the five main sections of this work are briefly described in the first part of the work. The work performed from chapters 2 to 6 includes reprinted fragments from one published peer-reviewed conference paper [48] and three manuscripts in preparation [1], [2], and [51]. In chapter 2, a literature review relevant to this thesis is covered, with the primary

focus on fracture, the effect of temperature on it, and different testing methodologies used to quantify it. In chapter 3, a detailed explanation of the working conditions and the design of the tested devices is given. The design aspects of the device that fit the methodology advantages concerning the existing approaches are highlighted. In chapter 4, the testing methodology and the data processing to quantify fracture strength are presented, and the results from this research are discussed. In chapter 5, a mechanical analysis that allows the determination of fracture strength is developed to validate the findings from the previous section. A comparison between the results from chapters 4 and 5 is made, and conclusions are made. In chapter 6, the modifications and improvements to the testing devices and methodology are described, preliminary work in these modifications is also presented. Finally, in chapter 7, the conclusions and the future work for this research are presented.

Chapter 2
Background and literature review

Parts of this chapter are an adapted form from manuscripts in preparation [1], [2]:

A. Navarrete, A. Ghannoum, and P. Nieva, "Creep of brittle MEMS structural materials: A review."

A. Navarrete, E. Brace, and P. Nieva, "A study of the fracture strength of silicon nitride thin films at high temperatures by means of the difference of coefficient of thermal expansion.

2.1 Brittle material MEMS devices

Microelectromechanical systems (MEMS) are devices with countless applications in several industries, such as automotive, medical, and communications. Their size provides an advantage in tasks where compactness and robustness are required. When the materials used in their fabrication transition from the macro to the micro-scale, their properties change, allowing for different behaviors. The materials can be metals, composites, ceramics, and polymers and they are selected based on the intended function and working environment of the device. The most commonly used type of material is ceramics, which are cataloged as brittle materials, which do not deform when a crack happens due to an absence of stress relief mechanisms in the material when the crack grows, and it does it freely until a fracture occurs [3]. However, ceramics still have properties that make them attractive for a variety of applications that other types of materials do not have. Unique dielectric properties, good insulation, excellent resistance to temperature and stress, robustness, resistance to harsh environmental conditions, and high fracture strength are some of the advantages they provide [3]. Due to their brittleness, semiconductors are considered as ceramic materials, therefore widely used in MEMS. These materials include silicon (Si), polysilicon (PolySi), silicon nitride (Si3N4), and silicon carbide (SiC), among others. Si and PolySi provide an extra advantage due to their compatibility with the fabrication techniques used to develop integrated circuits (IC) [4]–[6]. Thus semiconductor materials are ideal to be used as structural components in MEMS.

Ceramic material MEMS are used in a wide range of environments, one of which is harsh environments. A harsh environment is defined as a media where one or more of the following

conditions can be found: high temperature, intense vibrations, erosive flows, pressure, radiation, or corrosive environments [7]. Some of the industries that implement MEMS technology in this type of environment include the automotive, military, medical, aero defense, space, and medical sectors [7]. However, these environmental conditions have a significant impact on the material properties and the reliability of MEMS devices. In this work, high temperature will be the target environment for which the built and tested devices presented are focused. At the same time, "high temperature" will be considered as the temperature at which Si begins to degrade [8]. The electrical degradation of Si occurs at 150 °C, and its mechanical degradation starts at approximately 500 °C [9], [10]. Thus, any application that works over 150 °C will be considered as a high temperature.

2.2 High-temperature effects on the reliability and mechanical properties of MEMS materials

The reliability of a device is defined as its probability to fulfill the task it was designed for throughout its lifetime [11]. The lifetime of a device is referred to as the period during which it meets its objective and functions within its expected output specifications [12]. Reliability in MEMS is one of the most significant obstacles for them to be used on a massive scale; improving it is one of the most critical priorities for the development of microengineering [13]. The correct prediction of the lifetime of a device is also of great interest for estimations of when to replace a MEMS device. Thus, understanding these two concepts is vital for the further expansion and success of MEMS devices.

The most commonly used MEMS devices are accelerometers, pressure sensors, gyroscopes, thermal actuators, and chemical sensors [13]. All of these devices are used under many operating conditions. However, their successful operation at high temperatures is still minimal due to a lack of understanding of the limitations of their material properties want these harsh environments. For MEMS devices used in these environments, the characterization of their reliability is profoundly affected by temperature, leading them to faster aging, premature malfunction, and ultimate failure. These effects include the reduction of the materials fracture strength, reduction of Young's modulus, change in their CTE, and the rise of plastic

deformation to mention some [7], [11].

In the literature, evidence of these changes in properties can be found through several research groups. Jeong, J. et al. studied the variation of Young's modulus of Si micro resonators from 25 °C up to 600 °C observing a decrease from 168 GPa to 161 GPa as temperature increased [7]. The change might seem negligible; however, it happened after only 20 minutes of dwelling at high temperature. For devices that are expected to function thousands of hours in these conditions, this impact will be more altering. Burkhardt and Marvel studied the thermal mismatch between Si and Si_3N_4, obtaining the variation of the CTE of each material with respect to temperature. They developed equations reflecting the change based on their experimental data [14]. In the case of fracture strength, Sharpe, W. et al. tested the effect of temperature in the fracture strength of polysilicon specimens. These researchers observed small changes in the fracture strength of PolySi up to 250 °C [15]. The slight difference can be explained due to PolySi having a similar structure as Si; thus, more impactful changes are expected as the temperature gets close to 500 °C. As temperature increases and the material properties change, the effects that reduce the lifetime of the material become more detectable. Thus, it is essential to identify these effects and how they manifest in the materials.

2.3 Failure modes and failure mechanisms at high temperatures

The first step to study the reliability of MEMS devices is to determine the possible failure (failure mechanisms) of the device, and through which effects (failure modes) they make themselves present. Failure modes are defined as the apparent failure of the device; it is what can be visually observed to be the failure (i.e., a stuck beam, a broken component, or a worn-out element) [16]. The failure mechanism is the cause behind the failure mode, the physical explanation that caused the failure to happen (i.e., delamination, stiction, or wear out) [16]. These two elements need to be studied simultaneously to understand the whole process of failure.

The best approach to detect failure modes and mechanisms is to test the materials to their limits while measuring their physical properties and their change as the test progresses [7].

Examples of these tests include stress cycling, thermal shock, thermal cycling, and vibration testing [17]. The tests are designed to target a particular failure mechanism and observe its corresponding failure modes and effects on the material properties. For MEMS devices that operate at room temperature, some of the most common failure mechanisms are stiction, wear out, fatigue, and fracture. However, high temperature introduces failure mechanisms that are exclusive to these environmental conditions and changes the behavior of those observed at room temperature.

In their work, Spengen et al. enlist some high-temperature failure mechanisms, which include delamination, fatigue, package failure, thermal buckling, fracture, and creep:

- **Delamination**. - It takes place in the interface of stacked layers of different materials. It characterizes by the separation of the layers that compose the stack. Some of the causes are fabrication processing defects and high-stress levels at the interface. The stress at the interface comes from a difference in the CTE between the material layers [18]. Maligno, A.R. et al. studied the influence of thermal cycling in multilayered MEMS, the devices had both metallic and ceramic layers, such as copper (Cu), PolySi, Si, oxide, and nickel (Ni). They observed delamination at the interface of PolySi and Cu during thermal cycles up to 200 °C, which led to the conclusion that high temperature accelerated the delayering of the stack [19].

- **Fatigue**. – Fatigue is the gradual degradation of the materials of the device when they are submitted to cyclic stress; the stress source can be mechanical or thermal [20]. Kamiya, S. et al. studied the fatigue damage in PolySi by applying a load with a load cell in a nitrogen environment at two different temperatures, 22 °C and 180 °C. Experimenting with the same conditions except for the temperature helped to decouple its effect in the study of the fatigue damage in the sample. Their findings showed more significant fatigue damage in the samples exposed to a higher temperature [21].

- **Package failure**. – This failure mechanism is of particular interest for MEMS devices, since every device has to be contained inside a package to enhance its reliability, protect it from the environment and integrate it with its correspondent electronic circuitry [22].

High temperatures can damage the package, especially when metallic components are included, like solder joints. The interaction of the materials in the package generates a thermal mismatch, which leads to the fracture of the packaging, leaving the device vulnerable to the environment [23].

- **Thermal Buckling**. – It is associated with the instability of the device components when a load that surpasses a critical point; in this case, thermal is applied [24]. Once this critical point is reached, the element will bend out of the plane with respect to the axis where the load is applied. This effect will become a source of compressive stress in the device, which can accelerate other failure mechanisms, such as a fracture. Thermal buckling is highly dependent on the geometry of the component and the stiffness of the material that composes it. Ettouhami, A. et al. characterized the thermal behavior of a capacitive Si membrane-based pressure sensor. They observed the effect of the geometry of the membrane, size, and shape, on the temperature at which thermal buckling happens. A thicker substrate, made of Pyrex, resulted in a higher temperature needed for thermal buckling [25].

- **Creep**. – Creep can be defined as a time-dependent deformation when a load is applied [16]. It is affected and accelerated by high temperatures and high loads. It cannot be reversed, for which it is considered a plastic deformation. The effect of temperature and stress on the tested sample depends on the material composition and time of exposure to these elements [8]. Tuck, K. et al. used PolySi structures to observe the evolution of creep deformation up to rupture when the temperature changed at constant stress and when stress changed at constant temperature (Figure 1). The results showed that creep was influenced more by the temperature changes than from the stress variation [26].

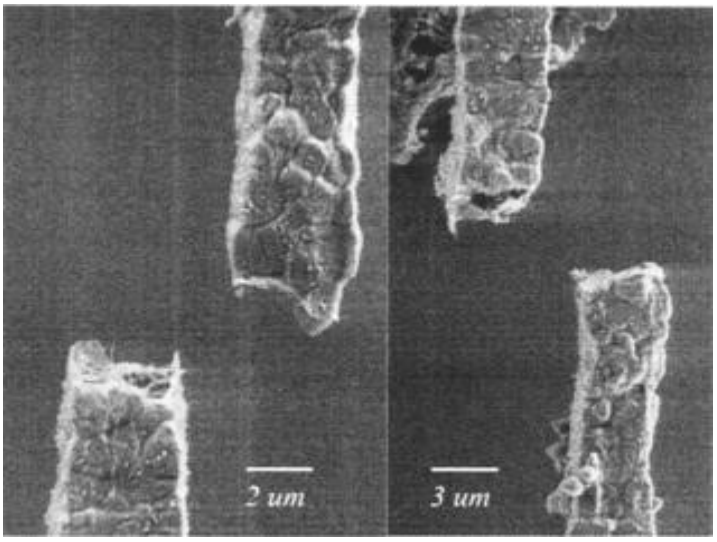

Figure 1. – Creep rupture of PolySi beams tested by Tuck et al. at high temperatures, the beams present necking, which suggests plasticity before their failure. Reprinted by permission from [26]. Copyright (2005) American Society of Mechanical Engineers ASME.

- **Fracture**. – Fracture is the separation of materials in two or more pieces. In brittle materials, it is originated due to the extension of a crack across the whole component ending its lifetime [11]. DelRio, F. et al. presented an extensive review of the fracture of Si and PolySi MEMS. They discussed the work of a few research groups that measured the dependence of fracture on the temperature in diverse materials and sizes. The results showed a decrease in the mechanical strength of structures leading to a faster fracture as temperature increased [11].

What most of these failure mechanisms have in common is the deformation of the material and their dependence on stress and temperature. These high-temperature deformations can be labeled as creep or material plasticity, which contribute to the fracture of device components. In the work of DelRio, F. et al., where temperature reduces the strength of the material, it can be speculated that creep and plasticity affected the fracture strength. Making fracture and creep the most predominant failure modes at high temperature. In this work, a focus on the fracture of micro materials at high temperature is taken. Therefore, in the following sections of this chapter, a more in-depth discussion of fracture, testing methods at high temperatures, and conditions that affect fracture will be presented.

2.4 Fracture strength

As mentioned in the previous section, the fracture is defined as the separation of an object, material, or system in two or more pieces. It is known as the ultimate failure mechanism due to the device becoming non-operational once it happens. Thus, materials have to be chosen with a strength that is higher than the stress values under which they will operate. Other causes of accelerating factors for fracture are fatigue, shock, wear out, and creep [27]. There are different types of fractures based on the breaking mechanics of the material. Fonseca and Sequera described this classification:

- **Brittle fracture**. – This fracture happens along the crystallographic planes of the material. It only takes a small crack to form in the material for it to expand rapidly until the component breaks.

- **Ductile fracture**. – This fracture is characteristic of ductile materials. As the material stress increases, a continuous plastic deformation appears in the stress concentration area of the component. This deformation is known as necking.

- **Creep rupture. –** It is found on brittle materials; it is highly similar to a ductile fracture, with the only difference of it being time and temperature-dependent [28].

- **Intercrystalline fracture**. – Characteristics of polycrystalline materials with a starting point in the boundaries of the crystal grains when a large number of impurities accumulate in them.

A schematic is shown for different types of fractures in Figure 2. For materials like Si, PolySi, and Si_3N_4, a brittle type of fracture is expected. Therefore, the focus of this study will be on brittle fracture.

2.4.1 Fracture strength of brittle materials at high temperature

Brittle fracture takes place when the material is exposed to stress strong enough to break the chemical bonds in its atomic structure [3]. Brittle materials tend to have high-stress tolerance.

However, if there is a high amount of flaws in the material, they help the stress to concentrate and become high enough to fracture it [3]. A definition of flaw is needed for a better explanation. Flaws are any small cracks or defects that can be present in the material due to fabrication, processing, or handling of the devices. As stress concentrates on these flaws, they grow until material breaks. When designing MEMS devices, a margin is left between the material's fracture strength and the operation stress; however, factors like temperature will accelerate fracture.

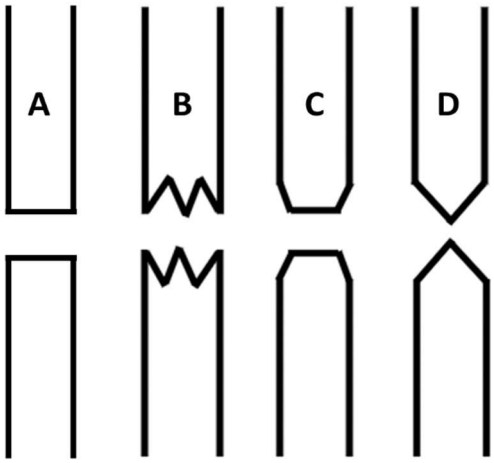

Figure 2. – Types of fractures on materials. A shows how a brittle material fractures, B shows the fracture of a moderately ductile material, C shows the fracture of a semi-ductile material, and D shows the fracture of a perfectly ductile material, also known as rupture [29].

The effect temperature has on the fracture stress of ceramic materials is directly related to their brittle to ductile transition temperature (BDT). As temperature increases, some ceramic materials begin to change their phase and display behavior of a ductile material, such as necking and no immediate fracture, which is known as the onset of plasticity [11]. Plasticity happens due to temperature reducing the activation energy of dislocation motion in the material, which is high at room temperature. Dislocations appear when a stress is applied to the material, and slip planes are spaces between crystals where the dislocations can move to as the material is stressed. Dislocation motion is the phenomenon where dislocations slip or climb through these spaces [30]. Temperature increase facilitates for the movement of these dislocations allowing them to accumulate and make the material harder to break, through a

healing process. This process counters the deformation and cracks propagation, causing the observed plasticity in the ceramic. However, even if the temperature increases the ductility of ceramics, it does not stop the atoms of the material to distance themselves from one another, decreasing the fracture strength of the material. Thus, as the temperature increases, the fracture strength of a material tends to decrease, making it a crucial design parameter that needs attention when creating a new device. Therefore, the relationship between temperature and fracture has to be studied closely. In the following section the work of several research groups that have studied this decrease and their proposed testing methods will be discussed.

2.4.2 Fracture strength testing methodologies

The study of how the temperature changes the properties of a material is of vital importance to be able to commercialize and produce sensors that work in these environments. A miscalculation or dismissal on any reducing effect temperature has in a mechanical property can cause a negative result when testing a device. Thus, several methodologies to measure the fracture strength of materials at high temperatures have been proposed. The challenge of these methodologies is not only to implement a heating element into their test but also handle and adapt to the dimensions MEMS devices have. There are two types of approaches when testing MEMS, one is to use macroscale testing methodologies and scale them to the size of MEMS, and the other is to create entirely new setups and methods. Another characteristic of the traditional approaches for fracture strength measuring is how the results obtained are processed. The results for fracture strength testing present commonly a scatter in the data, which is explained by how fracture works in brittle materials. As mentioned before, brittle fracture is dependent on flaws; however, these flaws are not consistent from one device to the other, even if they were fabricated in the same process and are virtually identical. Thus, statistical approaches are used to analyze the data; in particular, a Weibull distribution is used [31].

2.4.2.1 Weibull distribution

The Weibull provides a wide distribution that generates “best fits” for reliability data due to the many shapes the distribution can characterize and its ability to analyze small sample sizes.

The Weibull probability distribution function gives the probability for a structure to break when it is submitted to a stress σ is provided by (1) and is characterized by three parameters:

$$P_f(\sigma) = 1 - e^{[-(\frac{\sigma-\gamma}{\sigma_0})^m]} \quad (1)$$

Where m, σ_0, and γ are the Weibull parameters of dispersion of the data, the characteristic life, and location, respectively [32]. The dispersion parameter m indicates the grade of scattering of the data, and the characteristic life parameter σ_0 indicates the stress at which 63.2% of the samples will have failed, and the location parameter γ indicates the stress at which there will be zero failures [33]. The location parameter can be assumed as zero to reduce the number of parameters of the Weibull distribution to two. Therefore, a two-parameter Weibull distribution is used to analyze the fracture strength values obtained from the experiments.

$$P_f(\sigma) = 1 - e^{[-(\frac{\sigma}{\sigma_0})^m]} \quad (2)$$

The two-parameter Weibull equation given in (2) is solved using the values of the parameters m and σ_0. These parameters can be determined by applying linear regression to both sides of the equation. The linear regression is used to relate the temperature of the breaking of the thin film to the fracture strength of the material at said temperature. The linear regression in (3) is obtained by applying logarithm properties to both sides of (2):

$$\ln\left[\ln\left(\frac{1}{1-P_f(\sigma)}\right)\right] = mln(\sigma) - mln(\sigma_0) \quad (3)$$

Where using a methodology named "median ranks," the value of the distribution function is determined in (4). The values of fracture strength have to be ordered from the smallest to the largest and are assigned to the value of i, while n is the number of samples that constitute the studied population:

$$P_f(\sigma(i)) = \frac{(i-.3)}{(n+.4)} \quad (4)$$

Using the results from the left side of (3) as the Y-axis and the natural logarithm of the left side of (4) as the X-axis, a Weibull plot is formed. This plot is fitted with a straight line, and the value of the slope determines the m parameter. The expression given in (5) is used to

determine the σ_0 parameter:

$$\sigma_0 = e^{\left(-\frac{r}{m}\right)} \quad (5)$$

Where r is the residual from the straight line fitted into the equation, the parameters are used in (2) for the determination of the survival rate of the material. In the following section, diverse testing methods to determine fracture strength at high temperatures are outlined and reviewed.

2.4.2.2 Fracture strength characterization at high temperatures

In recent years, different attempts have been presented to characterize high-temperature fracture of ceramic materials. In 2001, Sharpe, W. et al. conducted studies on the stress-strain behavior of PolySi micro samples at high temperatures. They used two different specimens to do their research (Figure 3). The first specimen is called the wide device; this specimen consisted of a patterned suspended PolySi bridge and wide ended to facilitate its handling. The suspended bridge works as a stress concentration point with dimensions of 4000 µm length, 600 µm width, and 3.5 µm thickness. The narrow devices consist of a cantilever beam anchored to the substrate on one side and with a wide suspended end on the other. The beam connecting both ends is the stress concentration section and has dimensions of 50 µm width, 3.5 µm thickness, and unspecified length. Both devices have gold lines (markers) deposited on their stress concentration sections, and the lines are 20 µm wide, 0.5 µm thick, and of an undetermined length. The markers are set apart 200 µm and are necessary for the use of laser-based interferometry, which allows for in-situ strain measurements by monitoring this distance. A laser beam reflects onto the gold, creating fringe patterns, which position is dependent on the separation of the markers [15]. The test is performed by mounting the devices, according to their type, to set them up for stress application. The wide device was glued from its wide ends to the grips of the test setup. One of these grips is attached to an air bearing connected to a load cell that measures the load provided by a piezoelectric actuator. For the narrow devices, one end of a SiC fiber is glued to the wide free end of the device, and the other end is attached to a load cell that measures the load provided by a piezoelectric actuator. Both specimens were tested up to 250 °C, and the results for the narrow devices showed an expected scatter and a negligible variation in the results. For the wide devices, there

is only one data point available; thus, any conclusion on them would not be supported with enough evidence. From work done in this research, it is possible to draw some conclusions. The first observation is how useful it is to have a resource like interferometry to do in-situ measurements that are non-invasive to the test devices. It also allows for the continuous analysis of the strain throughout the whole experiment. Another observation to be made is on the handling of the devices. Handling micro devices without breaking them is complicated, and Sharpe et al. came up with an ingenious solution to address this. However, the use of adhesives would need to consider any thermal expansion mismatch between the glue and the glued material, also for any softening of the glue, which could loosen the grip on the device. Lastly, concerning the results and the negligible change on the fracture strength, it is expected for there not to be a considerable change due to the low temperatures at which these tests were conducted. Thus, higher temperatures are needed to study the temperature effect on the fracture strength of ceramics.

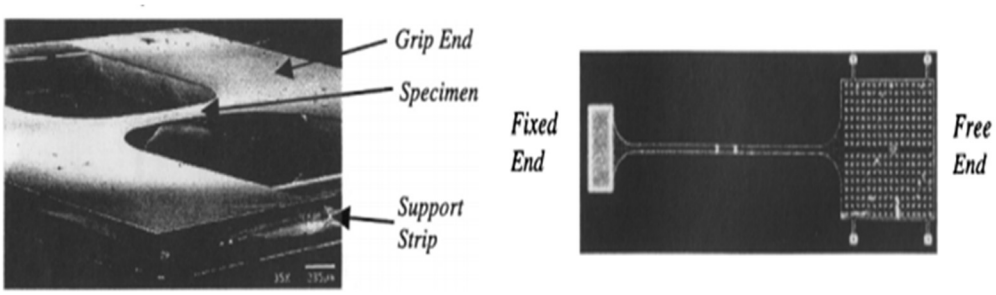

Figure 3. – On the left, the PolySi "Wide device" tested by Sharpe et al. to study the effect of temperature on material properties. On the right, the PolySi "Narrow device" used for the same study. Reprinted by permission from [15]. Copyright (2001) Springer Nature.

Higher temperatures are required to see the change in fracture strength, as shown by the previous study; thus, elevated temperature methodologies emerged in the following years. In 2008, Nakao, S. et al. studied the fracture strength of single-crystal silicon (SCS) from room temperature up to 500 °C. In Figure 4, their device and test setup are presented. Their device was composed of a support frame attached by the stress concentration beam to a load lever supported on torsion bars to apply tensile stress onto the test beam [34]. The test beams have lengths of 50 μm and 100 μm, a width of 45 μm and thickness of 4 μm. The way the devices

work is by applying a load onto the load lever, it rotates supported by the torsion bars and pulls on one end of the stress concentration beam. The tensile force is determined from the applied load. The experimental setup used to apply load and temperature has a stainless steel chamber with a heating stage in the middle, on the sides of the chamber, a thermocouple, and a cartridge heater. The load is applied on the load lever with a double cantilever spring, which is attached to the side of the chamber, and the displacement provided is measured with a capacitive resolution sensor.

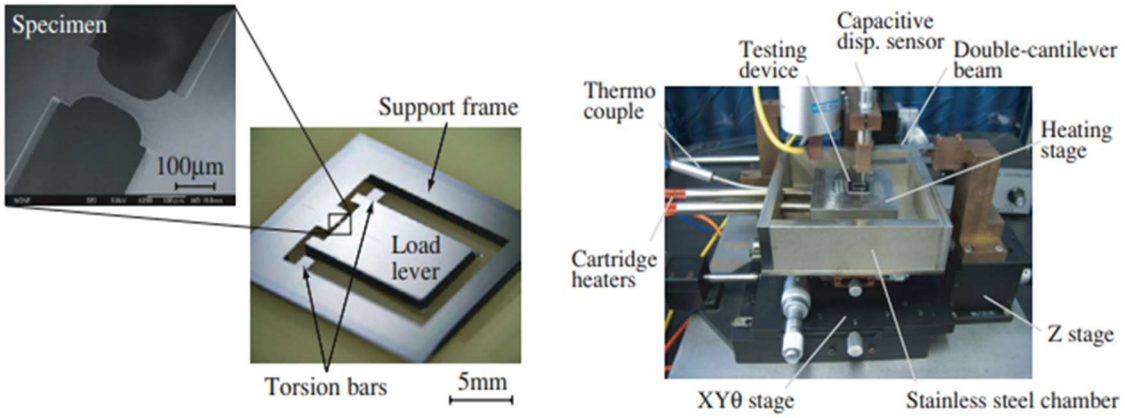

Figure 4. – On the left, the device used by Nakao, S. et al. to study the fracture of SCS at high temperature with its components is displayed. On the right, their custom test setup is shown with all the elements needed to perform their tests. Reprinted by permission from [34]. Copyright (2006) Journal of Micromechanics and Microengineering.

The stage is pre-heated to 500 °C, and once it is stabilized, the capacitive sensor and the double beam are activated to take measurements. At room temperature, the fracture strength of SCS was measured to be 5.73 GPa, and when measured at 500 °C, the fracture strength was determined to be 1.84 GPa. The authors attribute this decrease to the vibrations between atoms caused by the high temperatures. It is also worthy of mentioning that the authors observed plasticity in the beams at temperatures between 400 °C and 500 °C. In this experiment, it is essential to make emphasis on the drastic change the fracture strength of SCS had, which is expected in materials as their temperature is increased at high values. The more samples, the more a variation, and a better average of the value of fracture strength will be obtained. One of the short comes of many of these studies is the number of samples that are tested due to

financial concerns or capabilities of the setup. Better methodologies with high volumes of data at low costs are needed.

The previous studies characterize for a low volume of data points; thus, better tests that allow a more significant amount of tests are required. When the number of data increases, statistical methods become to study it. In 2009, Namazu and Isono conducted a study on the fatigue of SCS at temperatures up to 300 °C. For their studies, a reference fracture strength was required, thus using three different devices and two different test methodologies that characterized SCS fracture. The testing devices were classified as nano bending, micro bending, and tensile devices and tested with an AFM machine, a nanoindentation tester, and a custom tensile test setup, respectively [35]. In this review, the focus will be only on the nano bending and the tensile devices due to a lack of high-temperature testing on the micro bending devices. The nano bending devices were fabricated using a custom microfabrication methodology. The devices had a trapezoidal cross-section with the long width ranging between 0.37 µm to 0.98 µm, the short width from 0.2 µm to 0.8 µm, 6 µm length and 0.25 µm thickness. The tensile devices were fabricated using standard microfabrication processes. Their cross-sectional area was rectangular, and their dimensions were 76 µm to 250 µm of width, 4 µm to 24.5 µm of thickness and 100 µm to 3000 µm of length. The nano bending devices are tested on top of a heater that takes it to 300 °C using an AFM tip made of diamond. A periodic force is applied to the device using a piezoelectric actuator, and the force and deflection are calculated and used to determine the fracture strength. In Figure 5, the AFM bending test setup used by Namazu e Isono is shown. The tensile devices are tested with a custom tester consisting of a piezoelectric actuator built in a case alongside a linear variable displacement transducer, a load cell, and a specimen holder. The actuator loads the device, and the setup is placed in an X-ray diffraction equipment (XRD), and the X-ray characterizes the strain Young's modulus and Poisson's ratio. The results for every device were plotted, and a Weibull statistical approach used to obtain their average value. For the nano bending devices, the fracture oscillated from 17.63 GPa to 10.64 GPa; these results showed a trend of a higher fracture strength the smaller the device, and the lower the temperature. The change between two geometrically identical devices was of 1.85 GPa, with a fracture strength at room temperature of 17.63 GPa and a fracture strength at 300 °C of 15.78 GPa. For the micro bending devices, the fracture oscillated

from 7.68 GPa to 3.70 GPa; however, these devices only were varied in geometry and not temperature. For the tensile fractures, the fracture varied from 1.71 GPa to 1.31 GPa; these results also showed a trend of a higher fracture strength, the smaller the device, and the lower the temperature. The change between two geometrically identical devices was of 0.28 GPa, with a fracture strength at room temperature of 1.71 GPa and a fracture strength at 300 °C of 1.43 GPa. A trend can be observed with these experiments, which show as size decreases, the fracture strength increases and as the temperature increases, the fracture strength decreases. An observation from this study is all these data points due to how the devices are configured were done one at a time, which would take a long time and a long preparation of the samples. Testing more of one device during the same test run is an improvement that test designers should be aiming to achieve.

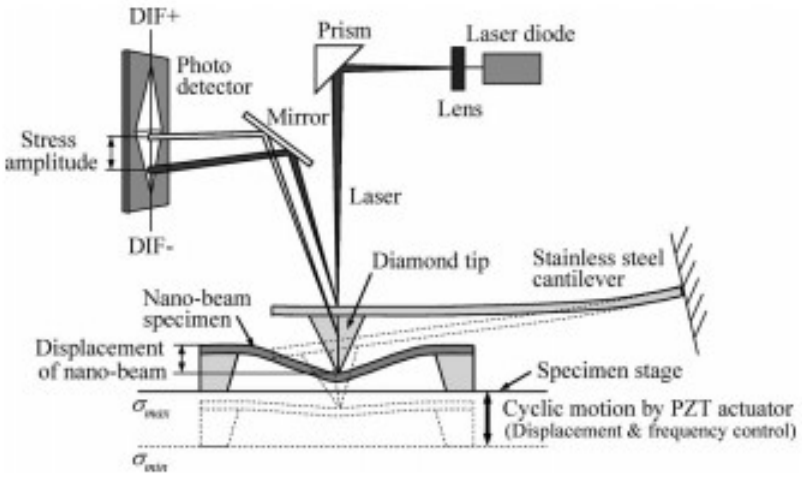

Figure 5. – AFM bending test setup designed by Namazu and Isono for the study of fracture and fatigue in nano specimens [35]. © [2009] IEEE. Reprinted, with permission, from [T. Namazu et al; Evaluation of size effect on mechanical properties of single crystal silicon by nanoscale bending test using AFM; Journal of Microelectromechanical Systems; February 2009].

Lastly, a review of the most recent work on fracture strength at high temperatures in micro-ceramic materials is presented to observe the current state of the methodologies. In 2018, Elhebeary and Saif proposed a new stage to do high in-situ temperature bending tests on Si microbeams (Figure 6). The experimental device is compact and can be placed inside a

scanning electron microscope (SEM) mounted in a testing stage. It is composed of a frame with two pinholes to stretch the frame and provide the bending of the device. The device testing beam is 60 μm long, 40 μm width, and 2.5 μm thick [36]. A series of support beams are used to transmit the force to the device, and a set of force sensing beams record the applied load. The displacement of these two types of beams during the test is measured by placing gauges near them. The testing stage is made of mechanical and thermal components. The mechanical part provides the stretching using a pin connected to a piezo actuator on one end of the device and a micrometer stage on the other, while the thermal part raises the temperature of the stage.

The mechanicals setup is set on a 1000 °C heating stage with a water-based cooling system for other stage components not to overheat. The displacement is measured by using SEM images and tracking the movement of the gauges, using the distance between gauges, and the stiffness of the beam a load can be calculated. Elhebeary and Saif tested their bending beams up to 450 °C, obtaining a fracture strength of 1.8 GPa and observing plasticity in the beam. There are a few things to mention in this experiment. The first one is how interesting it is to see plasticity at temperatures below 500 °C in SCS. The causes for this can be the levels of stress provided by the bending test affecting the device more than tensile testing stresses do. Another aspect to mention from this experiment is how, although innovative, the test setup is extraordinarily complicated and uses elements like pins and posts. While these components might accomplish their function, the more components involved in the testing, the more sources of risks, failures and possible errors. At the same time, the samples need so much support of auxiliary beams for measurements and load application that it only allows for testing a beam at a time, which allows for the conclusion that even most recent works although innovative addressing the handling of microdevices, still need better setups and adaptability to test multiple devices at the same time.

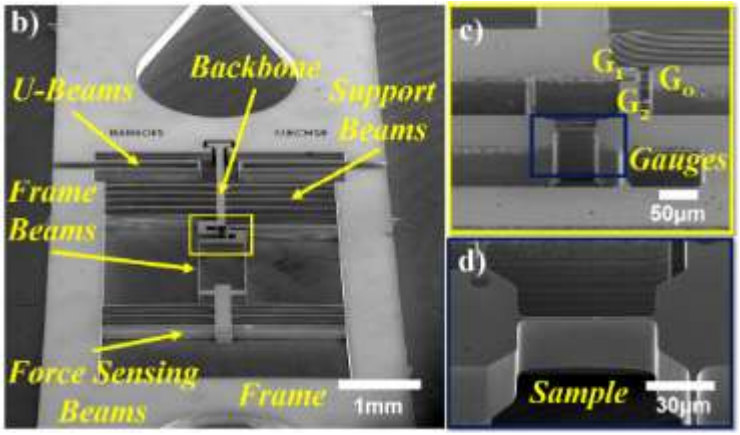

Figure 6. – The testing device used by Elhebeary and Saif, on the left, the frame, and supporting beams to transmit and measure the load in the sample are displayed. Top right, the strain gauge used to determine the force in the sample is shown, while in the bottom right, the test beam is shown. Reprinted by permission from [36]. Copyright (2018) Elsevier

As a conclusion from the review of all these works, it can be determined the ideal improvements a new methodology to measure fracture strength should have:

- Simple, accurate, and reproducible testing setups. Setups need to be able to be put together by other research parties for its improvement or further validation. The number of components should be kept to a minimum to reduce costs and to reduce the number of elements that can fail.
- Accelerated testing. Testing that is done in a matter of minutes, and that is not limited to one sample per test run.
- Testing setup resistant to temperatures over 500 °C
- Better handling of the testing devices to avoid sample destruction.

In all these studies, Si and PolySi MEMS are the focus of interest due to the number of applications that use these materials. However, as time has gone by, materials like SiC and Si_3N_4 have emerged already as the high-temperature alternatives for MEMS. Therefore, their properties with respect temperature need to be characterized due to their resistance to high temperatures makes it harder for them to be affected for additional factors that appear at high temperatures and accelerate fracture.

2.5 Factors that contribute to fracture

2.5.1 Creep

As mentioned before, creep is defined as a time-dependent deformation when a load is applied [16]. It is affected and accelerated by high temperatures and high stress. The effect of temperature and stress depends on the material composition and time of exposure to these elements [8]. It cannot be reversed, for which it is considered a plastic deformation. Although creep is a characteristic of ductile materials, brittle materials have been reported to experience creep when they operate near or beyond their BTD temperature and at high-stress levels for extended times. When creep generates stress for the first time in the material, an elastic deformation is generated alongside with a plastic deformation, as this continues, the dislocations in the material will move generating a strain known as creep strain rate [9]. Creep strain rate is used to quantify creep when the device is tested at a constant stress or a constant load.

Creep is characterized by three stages of deformation, which are primary, secondary (or steady), and tertiary creep [8]. In Figure 7, it is possible to observe how the three stages of creep behave in terms of their strain rate. Creep strain is given by the relationship between strain rate and time shown in (6):

$$\dot{\varepsilon} = \frac{\partial \varepsilon}{\partial t} \tag{6}$$

In the first region, known as primary creep, the creep strain rate increases and then starts to decrease until it stabilizes and reaches a constant rate. The following section is known as the secondary creep region, where the creep strain rate becomes and remains constant throughout the whole stage, and it is the lowest creep strain in the process. Lastly, the tertiary creep region is where the creep strain rate has a steep increase that leads to the fracture of the structure.

Each creep stage has a representative equation and has been applied for different types of materials. In the case of brittle materials, Tuck et al. characterized polysilicon micro samples resulting in plots with a trend that follows the graph shown in Figure 7 [26]. A brief description of the creep stages and their corresponding equations are presented in the following subsection.

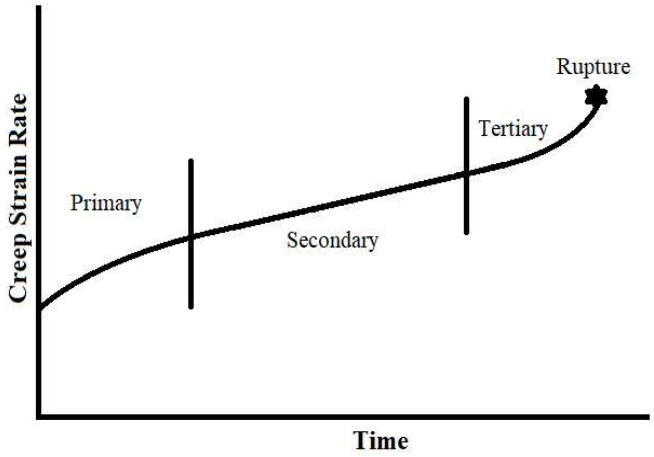

Figure 7. Characteristic plot for the different creep stages in a material submitted to high thermal stresses showing its different stages up to its rupture. The three different stages are primary, secondary, and tertiary [8].

2.5.1.1 Primary creep

Primary creep, also known as transient creep, occurs when the strain rate increases rapidly at a logarithmic scale. However, at the end of the stage, the creep rate slows down quickly [37]. The creep strain rate is represented in most cases by (7):

$$\dot{\varepsilon}_{primary} = At^{-n} \tag{7}$$

Where $\dot{\varepsilon}$ is the creep strain rate, t is the time, and A and n are experimental constants [38]. The constant n value has been found to range between 0 and 1, and each value derived a model. The first variation occurs when n takes the value of 1, which corresponds to the case of logarithmic creep or alpha creep shown in (8):

$$\dot{\varepsilon}_{primary} = \alpha log(t) \tag{8}$$

Where α is a constant observed in the characterization of different materials, such as Cu and aluminum (Al) [39]. The second variation is known as Andrade's law, or beta creep, shown in (9):

$$\varepsilon_{primary} = \varepsilon_0 + \beta t^m \tag{9}$$

In this expression, ε_0 is the initial strain that occurs when the load is applied, β is a constant related to the decrease of the strain rate with respect time, t is the time, and m is the Andrade's exponent. Andrade's exponent was mentioned to have a standard assumed value of 1/3 for several materials, due to how this value fitted the creep data obtained for several materials, such as polycrystalline metals, zinc (Zn) and celluloid [37]. However, Nabarro & Villiers later found that the exponent variation depending on the studied material renders more adequate fittings of data as opposed to always assuming a value of 1/3. Transient creep has been observed in brittle materials as the temperature at which they work is increased. Such is the case of Yao et al. for their study done in SCS membranes where they observed the creep of their devices could be characterized mostly by the primary creep portion of the creep plot [40].

2.5.1.2 Secondary creep

The second stage of creep is called steady creep, and a continuous straight line represents it. The reason for a constant strain rate is the equilibrium between the processes of deformation of the structure with another process of recovery [37]. The temperature and the stress deform the material as they increase, and at the same time, the temperature commences a process of healing of the forming cracks in the material, which balances the strain of the material [41]. The equation that defines the stationary behavior of creep is given by (10):

$$\varepsilon_{primary} = \varepsilon_0 + \beta t^m \tag{10}$$

In this equation, the terms A and n are material constants, and the variable Q is the activation creep energy of the material, R is the gas constant, and T is the temperature at which the device is submitted. The constant A is associated with the crystallographic structure of the material, while η is known as the power-law creep exponent. This constant has been found to take values between 3 or 12 for diverse materials, although there is evidence that attributes the variation of this parameter to the creep mechanism of the material [42]. This segment of the characteristic plot is the most used to study creep due to its stability and linearity. It is an important design parameter due to being the lowest creep strain rate the material will experience. A challenge of characterizing this segment is the variation of the creep parameters as creep progress, and taking them as constant can produce imprecise models of creep. Such is

the case of the creep activation energy, which is associated with the diffusion energy, changing over different ranges of the temperature of the material [43].

2.5.1.3 Tertiary creep

The tertiary stage is the last creep stage, where the creep rate accelerates until the fracture of the material, this fracture known as rupture [20]. Creep rupture is highly similar to a ductile fracture, with the only difference of it being time-dependent [28]. For ceramics, the rupture is caused by voids and micro-cracks that destabilize the structure of the material [30]. These cracks result from boundary separation, internal cracking, cavities, and necking in the material due the elevated stress and temperature [44]. This stage of creep is usually not recorded in experiments due to not be considered as crucial as the steady-state creep stage for device design. However, there is significant data at the beginning of the tertiary stage of creep. Pelleg, J. mentions that the transition between secondary and tertiary stage creep indicates the threshold at which the material will accelerate its decay. Some studies have associated the time of rupture to the time at which the tertiary creep starts to happen, and it is described by the empirical relationship in (11):

$$t_{tertiarycreep} = A * t_r^{\mu} \tag{11}$$

Where C and μ are constants with an empirical value often of 1. However, empirical relationships need further research to prove they are fit to describe various materials or instances. Creep manifests at higher temperatures in brittle materials opposed than in most metals; thus, it is harder to observe tertiary creep occur in them. In the following section, the creep mechanisms in creep and their relationship to fracture are highlighted.

2.5.1.4 Creep in brittle materials

The study of creep on brittle materials, mostly ceramics, was not of particular interest due to how prone they are to thermal shock [30]. However, upon finding their good thermal strength and resistance to corrosion and oxidation, the interest in working with them in high-temperature environments increased. Up to that point, the structure of brittle materials had made the study of the creep mechanisms related to their plastic deformation rather tricky. This

complication has caused for the study of creep in these materials to be ruled and characterized by the existing creep knowledge from alloys and metals. However, presently, brittle material creep mechanisms are known. They are dislocation motion for single crystal materials and grain boundary sliding (GBS) for polycrystalline materials [44].

The most used material in the MEMS industry is SCS. The electrical and mechanical properties of SCS have made it the most predominant material used in MEMS, especially as a substrate for MEMS devices. However, as has been mentioned before, SCS plastically deforms by the effect of high temperatures [10]. Over time this plastic deformation is known as creep. The creep mechanism for this type of material is attributed to the motion of dislocations. In Figure 8, the way a dislocation travels through a material is shown. Another brittle single crystal material is SiC, which is more resistant to creep than other ceramics. This material is one of the preferred materials catching the interest of high-temperature researchers for their applications. However, this material is not exempt from undergoing creep when the temperature and the stress reach very high levels. The temperature at which SiC creeps is found between 1575°C and 1750°C [45].

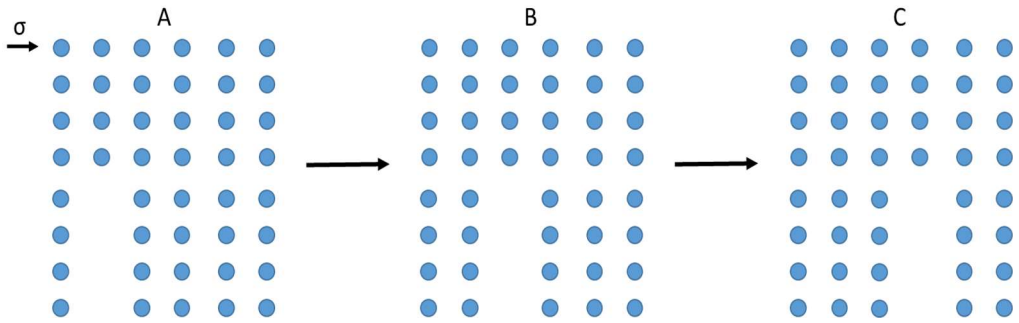

Figure 8. A diagram showing the process of dislocation motion. On A, a crystal lattice with a defect has stress applied to it. On B, as the bonds break due to the stress, causing the planes to rearrange and the defect to move, this is called a slip. On C, the slipping process continues [46].

In the case of polycrystalline materials, their grains slide past each other along their edges causing shear stress at their boundaries. This stress is responsible for GBS, which is responsible for the plastic deformation on the material, and it is caused due to the weakening of the grain boundaries. GBS is associated with a vitreous phase called the “glass phase,” which appears

around the grains as temperature increases and contributes to their sliding. It is believed that GBS is the precursor to the formation of cavities and voids that accelerate the creep rupture of materials. In Figure 9, a diagram showing how GBS works is shown. An example of materials where GBS is the creep mechanism is Si3N4 and its related ceramics. Its multiple applications make it one of the most characterized brittle materials by different research groups, and although it has excellent creep resistance, it is not immune to its effect [44]. Melendez and Rodriguez studied the diverse creep mechanisms affecting silicon nitride, mention that the inclusion of silicon nitride in various ceramic materials is often assumed to be accompanied by the vitreous phase aforementioned, which facilitates GBS, material diffusion and cavity growth during the high-temperature deformation of the material [44]. PolySi is a polycrystalline brittle material that is widely preferred when fabricating MEMS due to its high adaptability to the fabrication processes that work for Si structures. At high temperatures, it also displays a ductile behavior once it reaches its phase change point at 500°C [47]. Its polycrystalline structure makes it susceptible to GBS as it is shown in work by Tuck et al., where they observed grain growth in the fracture of PolySi and concluded its failure mechanism was due to GBS [26].

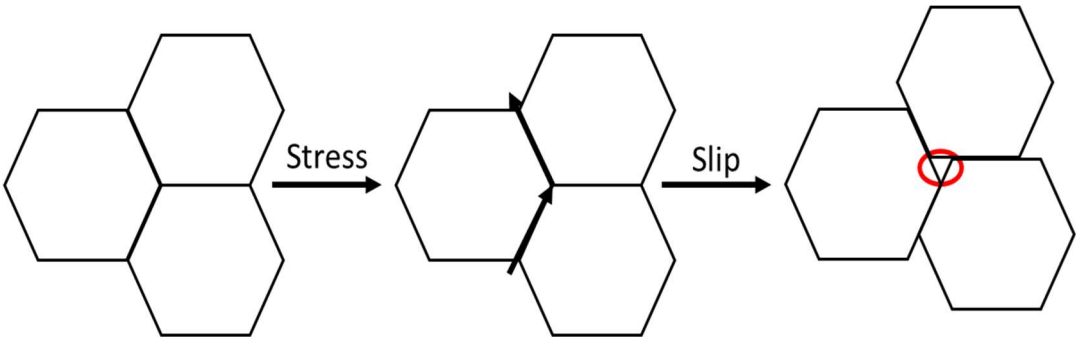

Figure 9. In the diagram, a set of grains is shown; as stress is applied, and the temperature is raised, the boundaries of the grains weaken, and movement is generated. The areas where multiple grain boundaries meet tend to be the most vulnerable to this effect [44].

Different attempts to quantify creep have been made and have had success matching data results with simulations as well as quantifying fracture strength. However, in many cases, the relationship between these material properties is not profoundly discussed, and neither is the effect creep can have in the other component of a test setup when fracture at high temperature

is being studied. More efforts need to be directed to define the interaction between these two failure mechanisms in MEMS.

2.5.2 Thermal buckling

As defined in a previous section, thermal buckling is the instability of a component due to thermal stress. This effect is prevalent on devices with layers of different materials in contact with each other. As temperature rises, the difference of CTE between the materials will generate a mismatch and causing stress to it. The direction of the stress will be dependent on which material is on top and which is at the bottom. If the material on top has a bigger CTE than the one on the bottom, the bottom material will pull the top material inwards, creating compressive stress. If the opposite happens, the bottom material will pull the top material outwards, causing tensile stress. If the mismatch stress is compressive and high enough to surpass the critical load, the structure buckles. The critical load is the point at which the structure becomes unstable, and in the case of thermal buckling, this critical load is associated with temperature called the buckling temperature [25]. Once the structure reaches this stage, any deformation is hard to predict, and even a small force can produce a strain that fractures the structure prematurely. The consequences of buckling in a tensile test device go from accelerated fracture to the device, not breaking necessarily at its stress concentration point or even breaking in more than one location. These effects make the study of the results even more complicated than they already are. Therefore, when designing high-temperature MEMS devices, an aspect of special attention has to be the CTE of the materials involved in the device that are in contact with each other.

2.6 Section summary

In this section, the interest in reliable MEMS that works under high-temperature environments is introduced. The best materials to achieve these MEMS are ceramics due to their high stress and temperature resistance. However, this does not make them immune to the effect high temperature has on material properties. These effects are a reduction of Young's modulus, an increase of the CTE, and a decrease of fracture strength, among others, which cause different failure modes and mechanisms to present at high temperatures. One of the most

predominant failure mechanisms in these environments is a fracture. Fracture is the separation of material in 2 or more pieces. As mentioned before, the fracture strength of a material is reduced as temperature increases, and its relationship with temperature has to be determined to guarantee the reliability of MEMS devices. Diverse approaches to determine fracture strength at high temperatures have been introduced in recent years, and a review of their advantages and disadvantages was presented. The conclusions reached about these tests, were their limitation to one sample per test and the complexity of the studied setups. The need for better and less challenging to recreate test setups to characterize materials at high temperatures rapidly is needed. In this work a methodology to determine the fracture strength of thin films is presented. Using experimental results and an FEA model, the fracture strength of Si_3N_4 thin films is characterized. Weibull analysis is made to determine the fracture strength from the data and the results are compared to an analytical model that describes the behavior of the devices.

Chapter 3
Study of fracture strength at high temperatures with silicon - silicon nitride devices

Parts of this chapter are an adapted form from a manuscript in preparation [2] and parts are an adapted form with permission from [48].

A. Navarrete, E. Brace, and P. Nieva, "A study of the fracture strength of silicon nitride thin films at high temperatures by means of the difference of coefficient of thermal expansion.

A. A. N. Gonzalez, E. Brace, and P. Nieva, "Size and Shape Effect in the Determination of the Fracture Strength of Silicon Nitride in MEMS Structures at High Temperatures," in 2018 IEEE 68th Electronic Components and Technology Conference (ECTC), 2018, pp. 2457–2463.

3.1 Test chip design

A proper device needs to be designed to determine the fracture strength of a material at high temperatures. To develop a functional MEMS device, the conditions under which it will be used have to be defined. In the case of this test, the most crucial parameter to be decided is the temperature of interest. In the previous chapter, the temperature threshold to be referred to as a high temperature was set to 150°C. However, as seen in the literature review, this temperature is not high enough to perceive a significant variation in the fracture strength of ceramics. Based on the literature review, it was possible to observe a substantial drop of fracture strength at 500 °C for SCS; thus, this temperature would be a proper parameter. However, most of the works found during this research were done on SCS or PolySi, which have a BDT at 500 °C. Thus, in this work, there is a higher interest in studying materials that have a higher BDT temperature, which is the case for Si_3N_4. For fabrication advantages and low residual stress in the thin film, a silicon-rich silicon nitride will be used and will be referred to as Si_xN_y. Using this material for the thin films allows for the temperature range of work to be increased due to Si_3N_4 experiencing its BDT at approximately 1100 °C [44]. Therefore, the temperature of testing for these devices is set at 1000 °C. A furnace with camera accessibility is used during the tests to reach the high temperatures needed for the experiment to return meaningful data.

As it was mentioned in the previous chapter, one of the most predominant limitations when

designing a testing method for fracture strength comes from the use of too many components during the testing. Micro-tensile testing commonly uses the support from load cells, connect wires, force measurement equipment, and more, to apply and measure the load in the device during testing. Thus, these devices have to be appropriately incorporated into the device or test setup, which complicates the whole structure. Therefore, for the design presented in this work, one of the most important aspects of it is the ability of the device to supply its stress. The chosen method to achieve this is with the use of thermal stress. Depositing two materials in a stack array and increasing their temperature will cause them to expand. Unless the materials are the same, the rate at which they expand is different, which will create stress in the interface where the materials are in contact. This effect is known as a thermal mismatch. Two materials with different CTE have to be chosen, and to attain tensile stress, the material at the bottom of the stack needs a higher CTE than the material on top. As stated above, the chosen material to work with is Si_3N_4, thus by comparing the nominal value of its CTE with the most common substrate material, Si, it is concluded that a mismatch will exist between both materials. The value for Si_3N_4 has been reported to be as low as $1.7x10^{-6}$ 1/°C depending on the deposition method and for Si is $2.6x10^{-6}$ 1/°C [14] confirming a tensile mismatch. A dog-bone shaped thin film bridge with a stress concentration beam called "gage" is used to maximize the effect of the mismatch and guarantee fracture in the same area of the devices. This stress concentration point allows for localized fracture when a critical temperature that stresses the thin film to fracture is reached.

The self-stressing nature of these devices allows them to be directly placed in a furnace and brought up to the needed temperature, which reduces the number of components required to test the devices. A furnace with camera access, a sample stage, a thermocouple, and a camera are enough to do the testing. It is also possible to fabricate arrays of devices and monitor the breaking of all of them with the camera recollecting data for several devices during a single experiment [49]. At the same time, the array of devices can be positioned within a chip of acceptable size to allow for the secure handling of the devices with tweezers. After defining the characteristics and expectations of the testing chip, the features of the testing devices have to be decided. Dimensions and shapes will determine aspects like the size of the arrays.

3.2 Device design

In tensile testing at the macro scale, it is common to observe specimens in a dog bone shape, as shown in Figure 10. These specimens characterize themselves for a narrow section in the middle intended for stress concentration. As mentioned before, this is called the gage section. The ends of a traditional dog bone shape are wider to allow for gripping and handling of the device when it is fixed in its testing setup, which is the most conventional tensile testing sample shape; therefore, the goal was to recreate this geometry for a thin film.

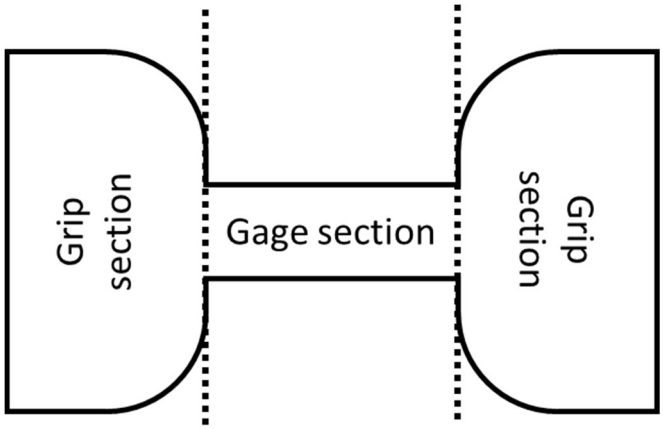

Figure 10. – Traditional dog bone tensile test shape. A gage section designed for breaking and a gripper section intended for fixing the specimen form this geometry.

A similar design to the one in Figure 10 is shown in Figure 11 but adapted to a thin film. The tensile design is achieved by using microfabrication techniques to remove the material underneath the whole thin film bridge. In Figure 11, the lines for length, L, and the width, W, of the bridge are shown, all across this length and width is considered the tensile thin film bridge specimen. The frame around the bridge is also made of Si_xN_y, but this section is not suspended, it is in direct contact with the Si substrate and is where the stress due to thermal mismatch will be created. That stress is assumed to distribute on the thin film uniformly, and due to the film, geometry is expected to focus on the gage. The gage is shown in Figure 11, where its width and length are delimited.

Within the scope of this research is to see the effect a change of shape and size has in the

fracture strength when high temperatures are involved. For this reason, three different shapes were tested for the study. Shape #1 has a trapezoidal-shaped grip section and the dimensions of length and width are of equal magnitude. Shape #2 also has a trapezoidal grip section, but its width is longer concerning its length. Lastly, shape #3 has a rectangular grip section, and just like shape #1, length and width are of equal magnitude. It has to be mentioned that for every device of every shape in this study, the gage section dimensions remain unchanged. In Figure 12, a schematic of the three shapes is shown.

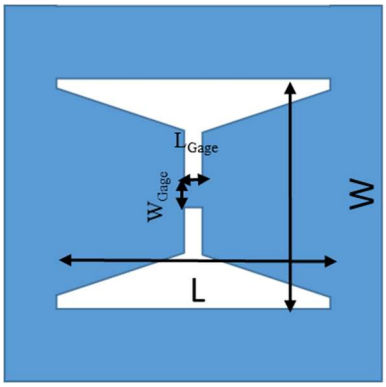

Figure 11. – Design of a dog bone tensile shape adapted as a thin film. Four main dimensions are indicated in the schematic [49].

Not only the shape of these devices was varied, but the length of each device was also modified to form arrays of devices. In the work of Nieva, P., the process followed to define the length variation of the thin films is described [50]. Using a graphical method that solved the geometry dependence on temperature and the length of the film bridges, Nieva determined a graphic relationship between temperature and length. This relationship allowed for the prediction of at which temperature a thin film of a specific length would break [50]. In Table 1, the different lengths and widths used in the fabrication of the thin films are shown. The gage dimensions and the thickness of the thin film are also included in the table.

The lengths chosen are to obtain breaking temperature ranging from 200 °C up to 1000 °C, which is within the target range of this study. All of the devices have the same gage geometry and thickness. The wide range of lengths and different shapes will show the effect of geometry

change. The larger devices are expected to fracture before the shorter ones due to the probability of finding a critical flaw is higher the longer a device is.

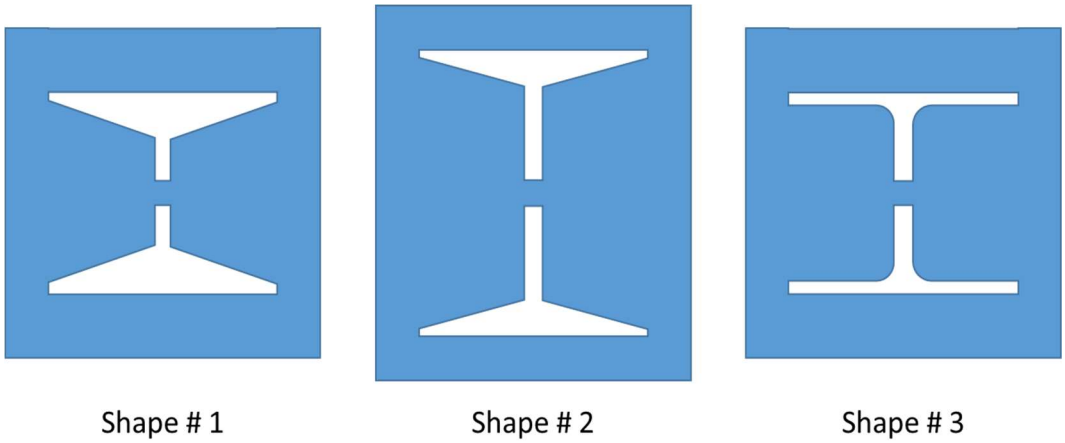

Figure 12. – Schematic of the three shapes used in this study of fracture strength of Si3N4.

Table 1. – Dimension range from the three different shapes fabricated

		Shape #1	Shape #2	Shape #3
Length	L	152 µm – 217 µm	134 µm – 199 µm	98 µm - 172 µm
Width	W	152 µm – 217 µm	187 µm – 252 µm	98 µm - 172 µm
Length of gage	L_{gage}	3 µm	3 µm	3 µm
Width of gage	W_{gage}	3 µm	3 µm	3 µm
Thickness	t_{film}	0.175 µm	0.175 µm	0.175 µm

Now that the devices working conditions and design have been defined, a microfabrication process has to be followed to create them.

3.3 Device Fabrication

The test devices were fabricated depositing a 0.175 µm thick Si_xN_y thin film on top of an n-type Si substrate using a low-pressure chemical vapor deposition (LPCVD) process. The

deposited Si_xN_y thin film is patterned into dog bone shapes using wet bulk micromachining and etched using Tetramethylammonium Hydroxide (TMAH). The fabrication process is at controlled temperature and, to avoid breaking the wafer is rinsed in water and alcohol before drying it. The fabrication process of the test structures used here has been detailed elsewhere [49]. In Figure 13, images of the fabricated devices of each shape are shown.

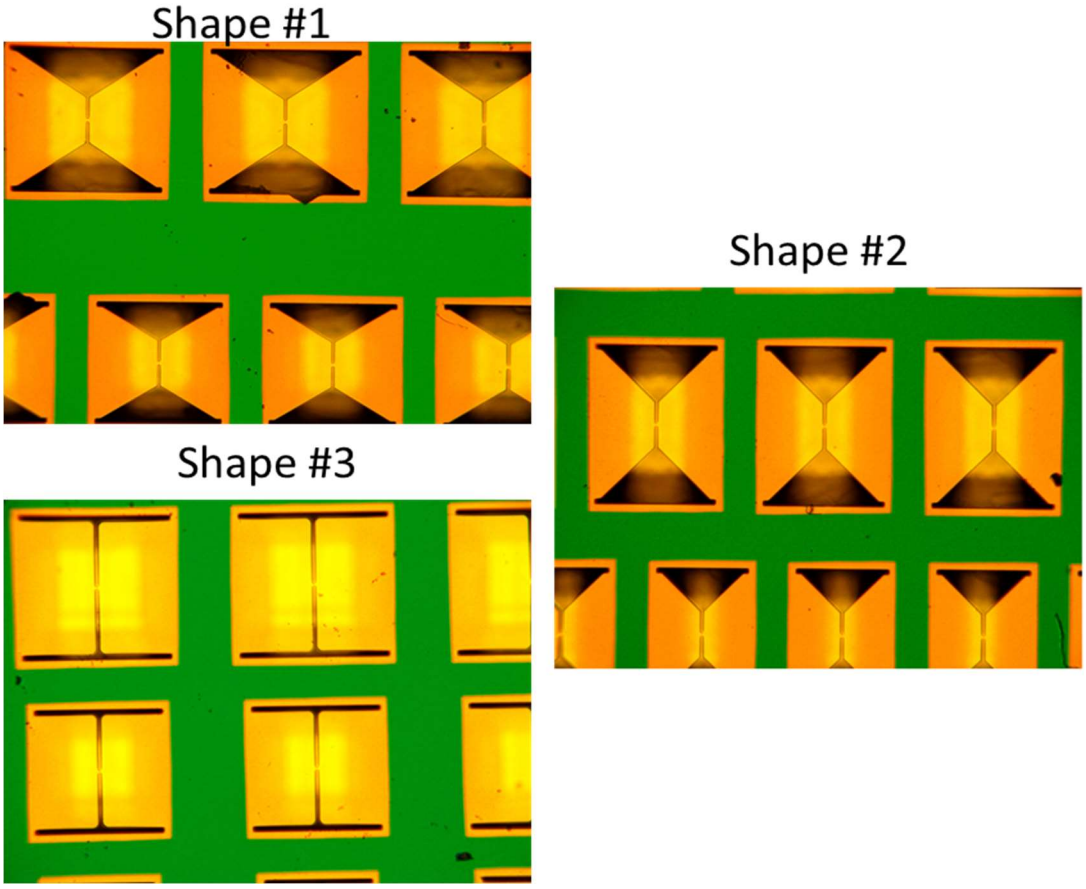

Figure 13. – Fabricated devices using the presented micro sensor process. On the top left, shape #1 devices are shown. On the right, devices of shape #2 are shown. On the bottom left, devices of shape #3 are shown.

The current state of fracture strength testing in micro materials is still in development of a reliable methodology to determine the fracture strength of micro materials. As the dimensions of the samples decrease the complications to handle and apply stress to them, becomes a very difficult task. Thus, these thin films propose a solution to samples breaking during handling

with the thin film being surrounded by hundreds of microns of substrate material. The device to be tested using noninvasive techniques to apply stress, which sets it apart from the current methodologies that rely in complicated attachments to provide stress. The devices are easy to replicate, so they can be available for other research groups as a quick testing tool for their materials.

Chapter 4
Testing and FEA Simulation

Parts of this chapter are an adapted form from a manuscript in preparation [51]

A. Navarrete and P. Nieva, "Determination of the fracture strength of silicon nitride thin films at high temperatures through finite element analysis."

4.1 Methodology objective

The objective of this methodology is the combination of experimental data for it to be used in an FEA model to obtain the fracture strength. The devices are exposed to a heating element that will change their temperature at a steady rate until fracture. The temperature for each device is registered with the respective length and shape of the breaking device. Using a computer-assisted design (CAD) software, Solidworks, the devices are modeled, and these models are imported to an FEA software, COMSOL, which will emulate the behavior of the device during the test by defining appropriate initial and boundary conditions (BC). The temperature in the simulation is set to go from 20 °C to 1000 °C, and through interpolation, the stress at the breaking temperature is simulated and registered. That procedure is repeated for several devices of each shape until a curve of fracture strength against temperature for each is formed. Each plot is processed using a Weibull statistical approach, and the average fracture strength of each shape is obtained. Therefore, the first step for this methodology is the testing of the devices.

4.2 Device testing

The arrays of structures were tested using a tube furnace to provide the thermal stress to them. Different arrays of devices were tested, and every array was composed of one shape at different lengths. The temperature was ramped out at a constant rate of 98 °C/minute during 10 minutes taking the arrays from 20 °C to 1000 °C. A thermocouple is used inside the furnace to keep control of the temperature during the whole experiment. Pairings of breaking temperatures with the length of the device are formed from every study. Compared to current

approaches, reviewed in chapter 2, the testing is straightforward are can be done with a system consisting of a heating element and a video recorder. When compared to other approaches, it is possible to see the advantages such a simple provides for the experiment to be available for anyone that has access to these common elements in research facilities. The devices had no handling issues and there was a meaningful amount of data obtained each time the experiment was ran.

Two sets of arrays were tested for each of the three shapes in this study. In Figure 14 to 16, a plot with the experimental data obtained from each shape is presented. In the X-axis, the temperature at which each device broke is found, and on the Y-axis, the length of the tested device is located. In each of these plots, the trend of an increasing breaking temperature as the devices become smaller is followed, which corresponds with the trends that are shown in the literature. In Figure 17 and 18, all the results with their corresponding linear fitting lines are shown. The linear fitting shows that despite the scattering, the decrease of length causes an increase in the breaking temperature of the devices.

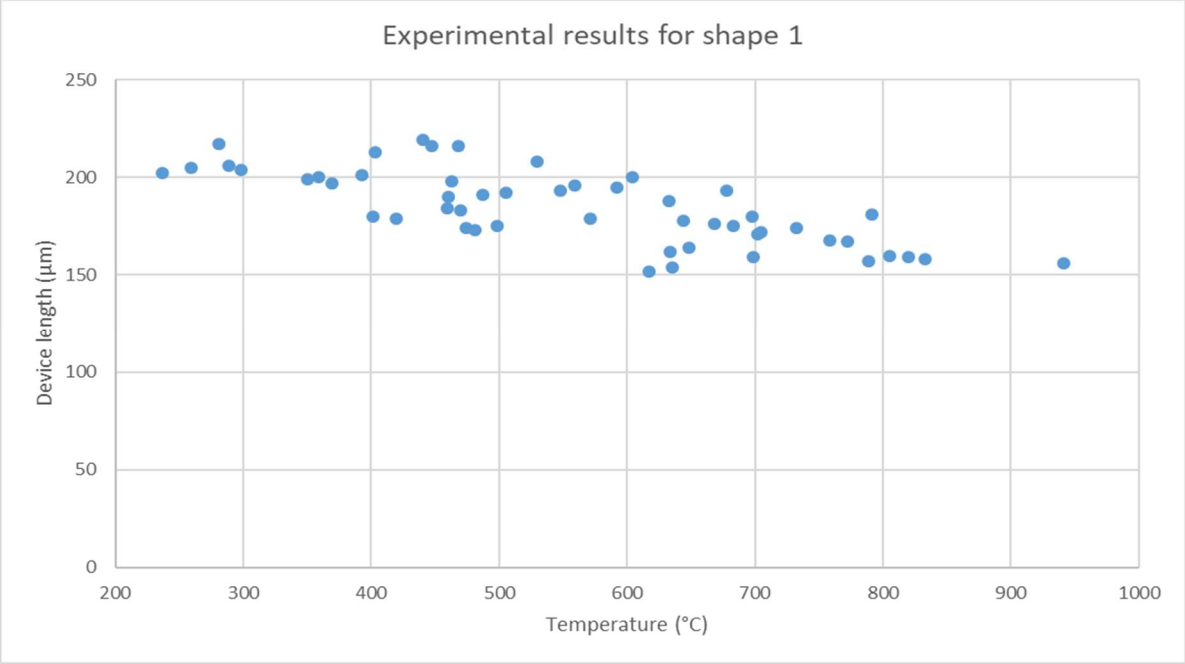

Figure 14. – Experimental results for devices of shape #1. The temperature of breaking increases as the length decreases.

The required applied temperature for fracture of a brittle material is a variable parameter, dependent on the material structure and its flaws. As mentioned previously, the probability of the imperfections in a device to be the same as another device is very low. Therefore, it is reasonable to observe scatter in a relationship that could almost be described as linear. The data is taken and used for the FEA modeling of the fracture strength of the thin films.

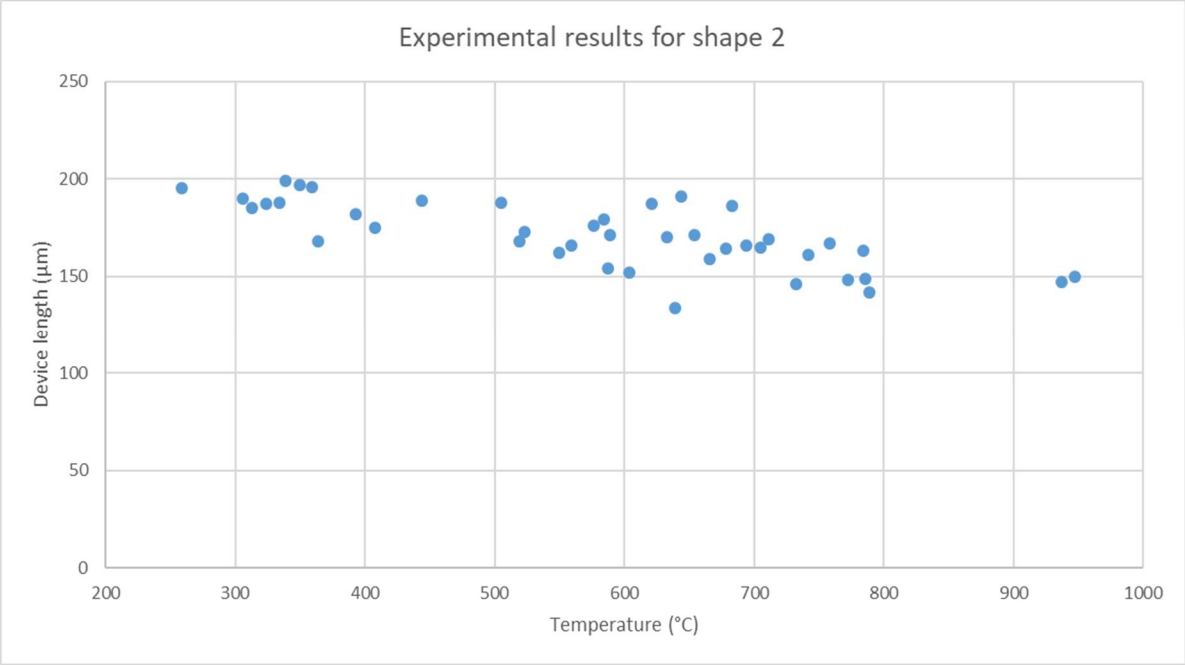

Figure 15. – Experimental results for devices of shape #2. The temperature of breaking increases as the length decreases.

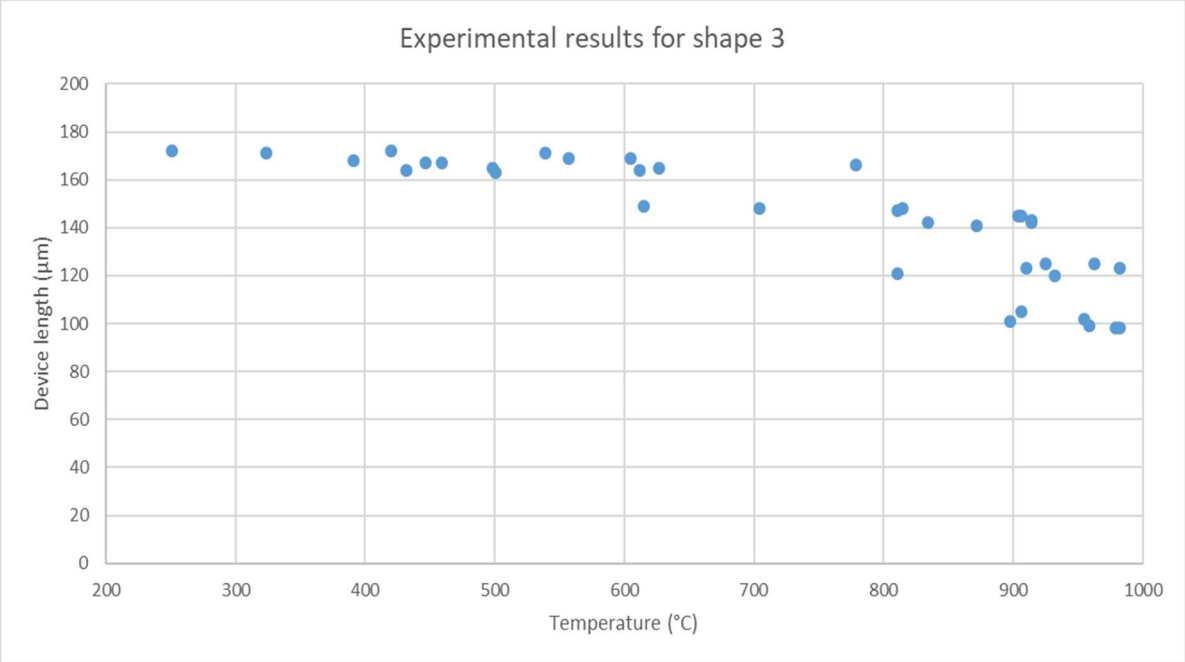

Figure 16. – Experimental results for devices of shape #3. The temperature of breaking increases as the length decreases.

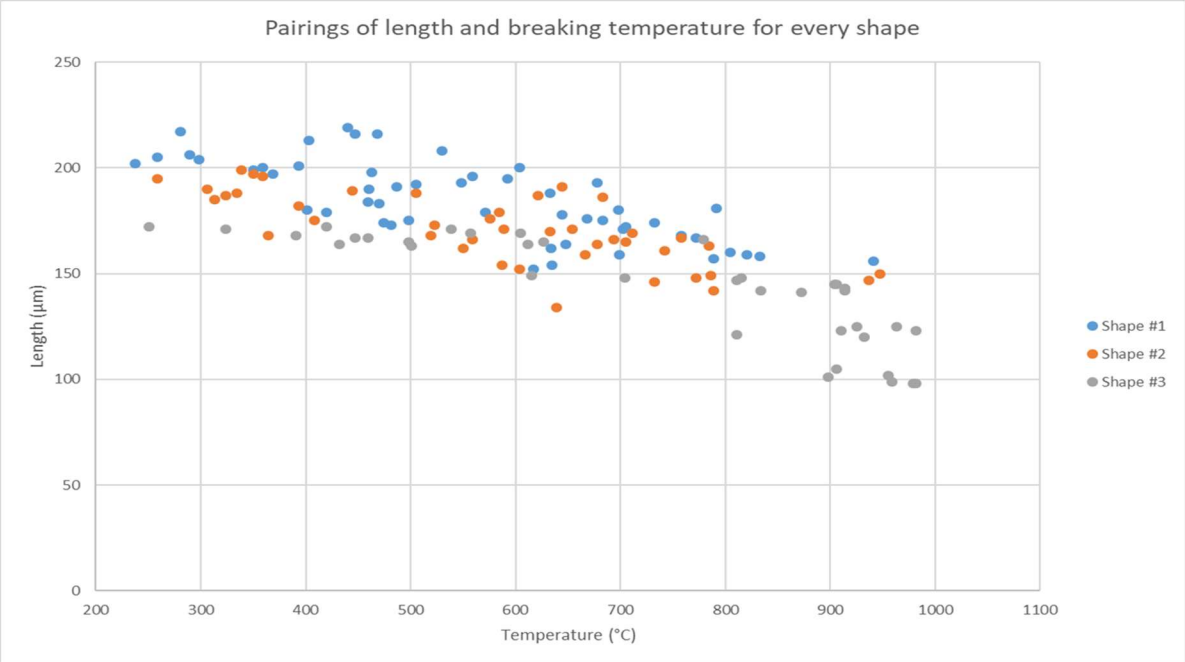

Figure 17. – A plot of the experimental pairings obtained from testing devices of Length L up to their breaking temperature T.

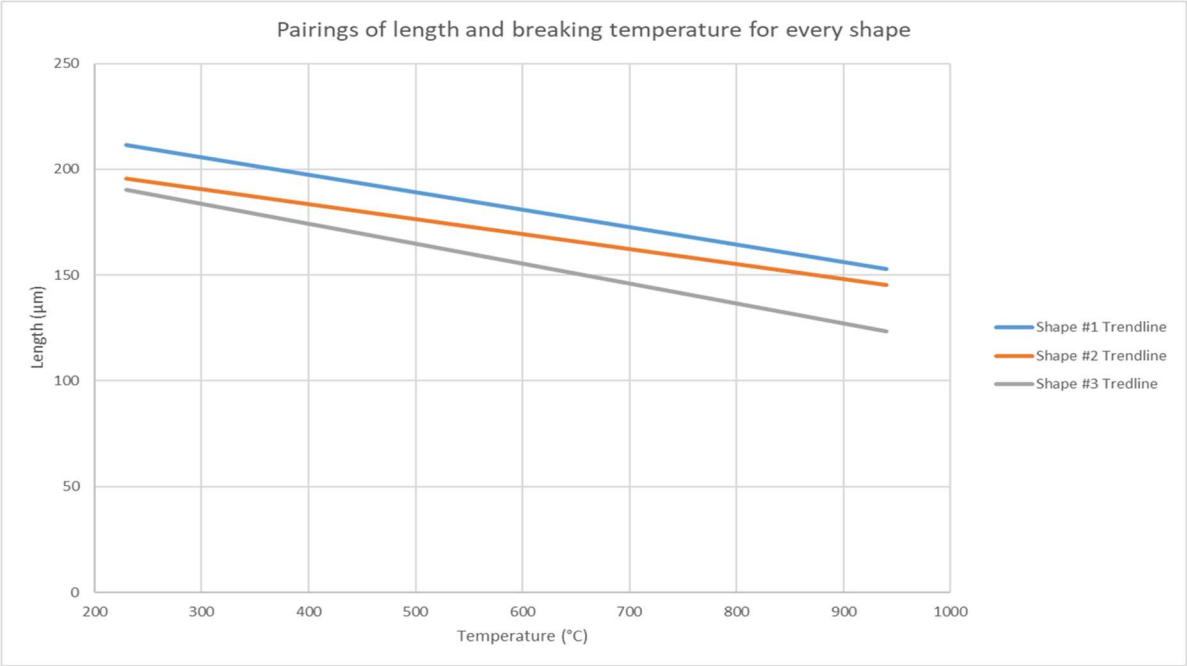

Figure 18. – Trend lines corresponding to the breaking temperature of devices of different length and shape tested.

4.3 FEA simulation

A data point is chosen from the pairings obtained experimentally to set up the simulation to determine the fracture strength of the thin film. The simulations are done in two steps. The first step is a stationary study to simulate the residual stress of thin films. When a device is fabricated, the high-temperature processes and the CTE mismatch creates thermal stress as the finished devices cool down to room temperature. This stress will influence the behavior of the device. The tested thin films in this work had their initial residual stress determined by measuring the substrate deformation using a profilometer [50]. The determined value of the initial residual stress of the films was determined to be 0.36 GPa ± 0.3 GPa. In this work, the value of 0.39 GPa is used for the methodology to be used in the case where the thin film experiences the most applied stress. The second step is a time-dependent study that raises the temperature of the device up to its breaking temperature. For both studies, the setup procedure is identical during the first steps, and it will only change when the boundary conditions (BC) of the model are set. Depending on the shape and the length of the device, a CAD model is made for the device. In Figure 18, a CAD assembly of a device of shape #1 is shown. In this

case, to avoid the simulation to take a long time to be completed, the substrate was made less thick than it is. The value selected for the wafer thickness is 100µm, which is large enough to keep a vast difference with respect to the thin film and avoid torsion effects. In COMSOL multiphysics, the CAD model is imported, and it is configured for the assembly to be treated as a union, which models all the domains to allow for their meshing as if they were one, which is used for interacting domains. A domain is every individual component of an assembly in COMSOL.

The next step consists of assigning materials to the different components of the assembly. The thin-film material is assigned as Si_3N_4 and the substrate as Si. However, for the simulation to reflect the behavior of the device, the material properties affected by temperature have to be characterized as such. As mentioned in chapter 2, Young's modulus and CTE are affected by temperature; thus, they cannot be expressed as constant values when performing simulations in a wide range of temperature values. The first property to be modeled is CTE. Referencing the work of Marvel and Burkhardt, they found expressions that characterized the CTE of both Si and Si_3N_4. For Si, the expression is given by (12) [14]:

$$CTE_{Si} = -5.35x10^{-6} * exp^{-6.83x10^{-4}*T} + 7.81x10^{-6} \quad (12)$$

Where T is the temperature. The expression for Si_3N_4 is given by (13):

$$CTE_{Si_xN_y} = -3.78x10^{-6} * exp^{-5.6x10^{-3}*T} + 4.01x10^{-6} \quad (13)$$

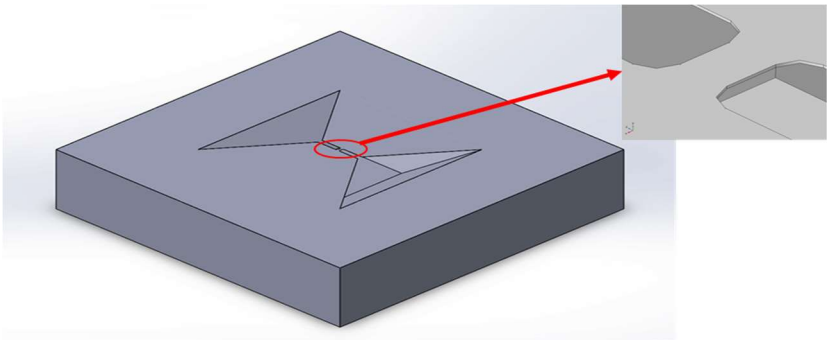

Figure 19. – Assembly to be imported to COMSOL multiphysics. The assembly has a thin film of shape #1 on top of a substrate. In the inset, the stress concentration section of the thin film is shown.

Where T is the temperature, in Figure 20, both expressions are plotted from 0 °C to 1000 °C. The plot shows how both CTEs increase as temperature increases. The separation between both CTEs as temperature increases makes discernible how taking a constant value for these parameters would not reflect the real behavior of the device.

In the case of Young's modulus of the materials. Expressions that characterized the change with temperature of the parameter were researched. For Si, the following expression was found (14) [52]:

$$E = 1.2x10^{5} * exp^{\frac{4.18x10^{-22}}{k_B * T}} \quad (14)$$

Where k_B is the Boltzmann constant, and T is the temperature. Due to a higher difference between Young's modulus than the difference found in CTEs, this property will be shown in individual plots. In Figure 21, The variation of Young's modulus of Si with respect temperature in a range of 0 °C to 1000 °C is shown.

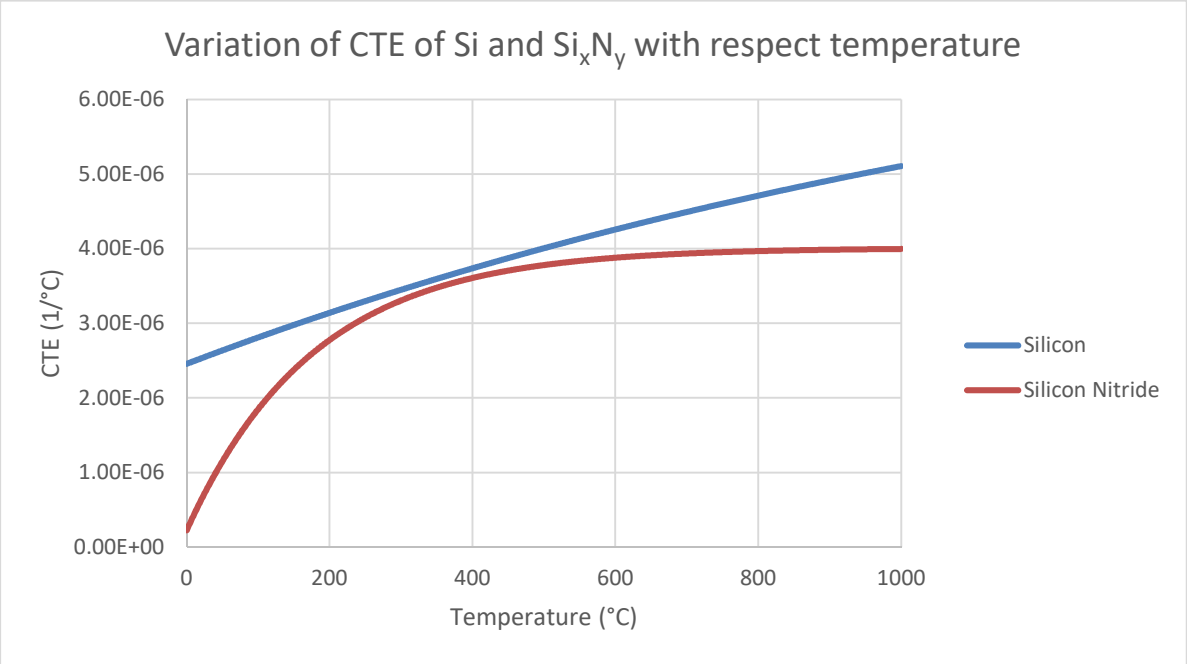

Figure 20. – Variation of the CTE of Si and Si3N4 with respect to temperature from 0 °C to 1000 °C.

The expression for Si_3N_4 is given by (15) [53]:

$$E_{Si_xN_y} = E_0 - .0151T exp^{\frac{-445}{T}} \quad (15)$$

Where E_0 is Young's modulus of Si_xN_y at room temperature, and T is the temperature. In Figure 22, The variation of Young's modulus of Si_xN_y with respect temperature in a range of 0 °C to 1000 °C is shown. It is possible to confirm the decrease of Young's modulus with respect to temperature by observing both plots. While the decrease does not look numerically relevant, it is essential to mention that this decrease is in the magnitude of Gigapascals, which is high. The material properties for the silicon substrate in this study are defined as isotropic since the objective of the simulation is to replicate a uniaxial test. The values for Young's modulus and CTE are those of a Si wafer in the <110> direction [14], [54]. It must be mentioned an anisotropic configuration may be used for the Si substrate for a more complete analysis of the stresses that will act in the thin film, which will affect its elastic properties and its interaction in the boundary with the thin film. Once the material properties are set, and the materials are assigned, the next step is to define the physics and boundary conditions in the model.

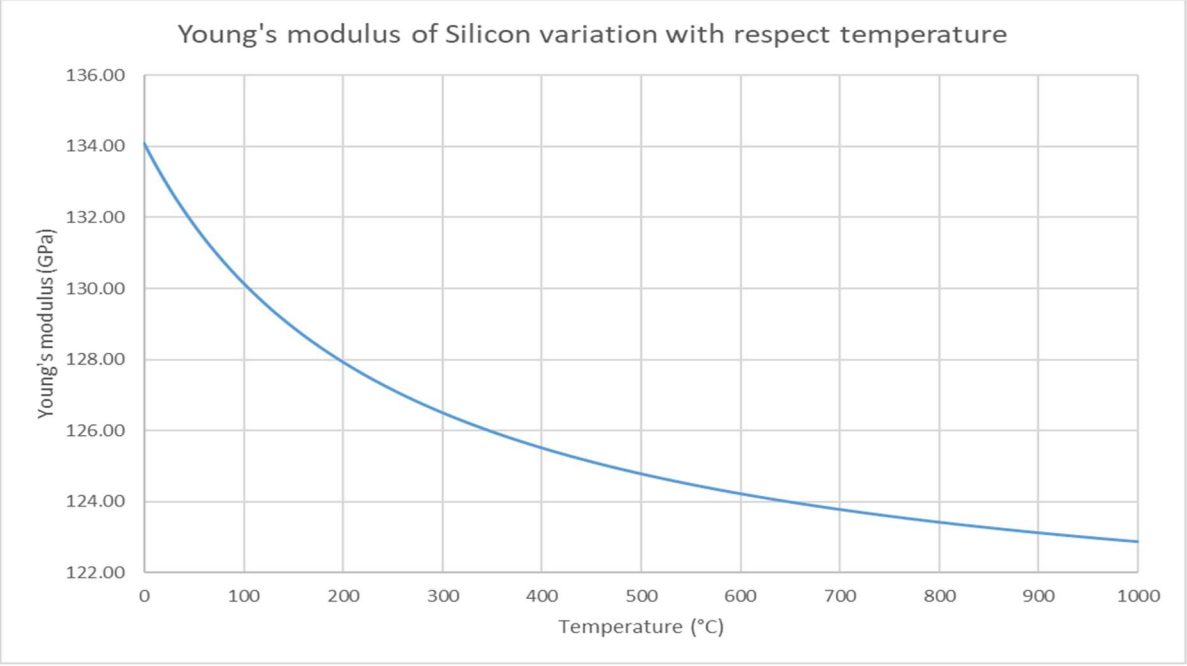

Figure 21. – Change of Youngs modulus of Si with respect to temperature from 0 °C to 1000 °C.

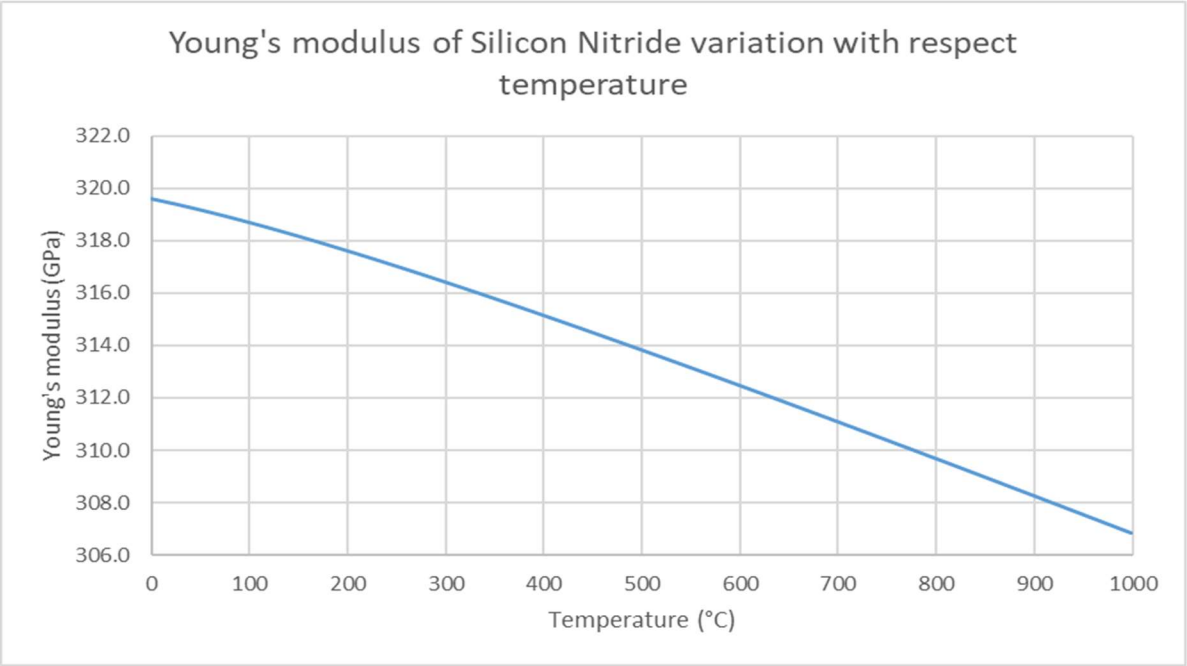

Figure 22. – Variation of Young's modulus of Si_3N_4 with respect to temperature from 0 °C to 1000 °C.

The physics needed to model the behavior of the devices during the experiment are those that generate thermal stress. In COMSOL, there is a prebuilt function for thermal stress that requires mechanical and temperature BC. For each simulation, there are a few similar and a few different BC; thus, the BC will be listed for each study individually. The BC for the first study on the mechanical side is the following:

- The solid is defined as a linear elastic material, which will add two sub-nodes. The material is chosen to be elastical, focusing on the thin film reaction to the difference between the coefficient of thermal expansion. Silicon nitride is a material that does not go through plastic deformation at the temperatures used in this research. The first sub-node will configure the device to be free in every boundary with no loads or constraints. In the case of the studied device, this will not be true for the domains where the thin film and the substrate are constrained, thus that boundary is not free. The second sub-node sets every displacement and the velocity of every boundary as 0. The expression to be solved will be given by the following set of equations:

$$\sigma = \sigma_{ad} + C : \varepsilon_l$$

Where C is the elasticity matrix as a function of Young's modulus and the Poisson

ratio and ε_l is the elastic strain of the system, which is determined from the displacement change through the material.

- The four bottom corners of the substrate are constrained to simulate the conditions of the experiment. The fixed condition is set to just the points at the corners, so the edges of the bottom boundary still can expand as temperature increases.

The BC for this device in the heat transfer side is the following:

- The heat transfer mechanism chosen for the model is that of solids. These settings will create two sub-nodes in the model. The first sub-node will set the initial temperature of the device to a value of choice; in this case, the temperature of 1177 °C is used. The temperature for applying the residual stress varies depending on the device's length. This temperature was searched after the mesh is defined by looking for a temperature that causes 0.39 GPa of stress on the thin film when cooled down to room temperature. The second sub-node is an insulation setting that stops the heat flow of any chosen boundaries.
- The second BC is to apply the temperature to every boundary as the tube furnace does in the experiment. Room temperature is the target temperature of this study, and this is set to 20 °C.

When these two physics nodes are created, a multiphysics node can be created for thermal stress determination. In these nodes, the CTE and the reference temperature for the thermal strain are defined. In this case, the reference strain temperature is the initial temperature of 627 °C, and the CTE is taken from the material configuration.

Once the BC is set, the last step is to set the mesh for the study. A mesh study was done to determine the most optimal mesh size and optimize simulation time. The mesh convergence is done by doing meshes with a different number of elements, and the value of stress that is being looked for is registered. In Figures 23 and 24, the results of the mesh convergence can be observed for the values of residual stress and fracture stress, respectively. In the X-axis is the total number of elements, every mesh unit, and in the Y-axis the values of stress. As the number of elements increases, the precision of the stress measurement increases too. Once the variation

minimizes, the addition of elements becomes negligible; thus, the mesh can be kept at that size. In the residual stress plot, it can be appreciated how the results start to vary less at 600,000 elements; this corresponds to a regular-sized mesh. In the case of the gage section stress plot, it can also be appreciated that the results vary less. Thus, a regular-sized mesh will be used to perform the FEA of the devices. In table 2, the dimensions of the element size in the mesh are shown.

Table 2. – Mesh dimensions for the FEA analysis

Number of elements	682359
Maximum element size	8 µm
Minimum element size	21.2 µm

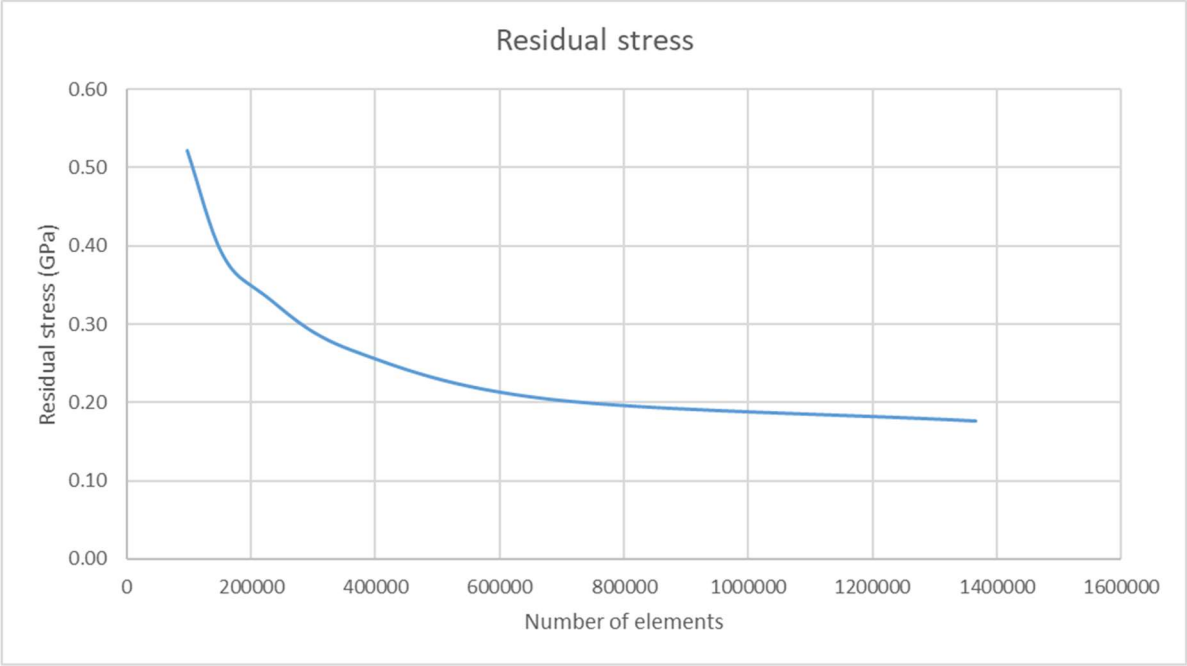

Figure 23. – Mesh convergence plot for the residual stress of the thin films

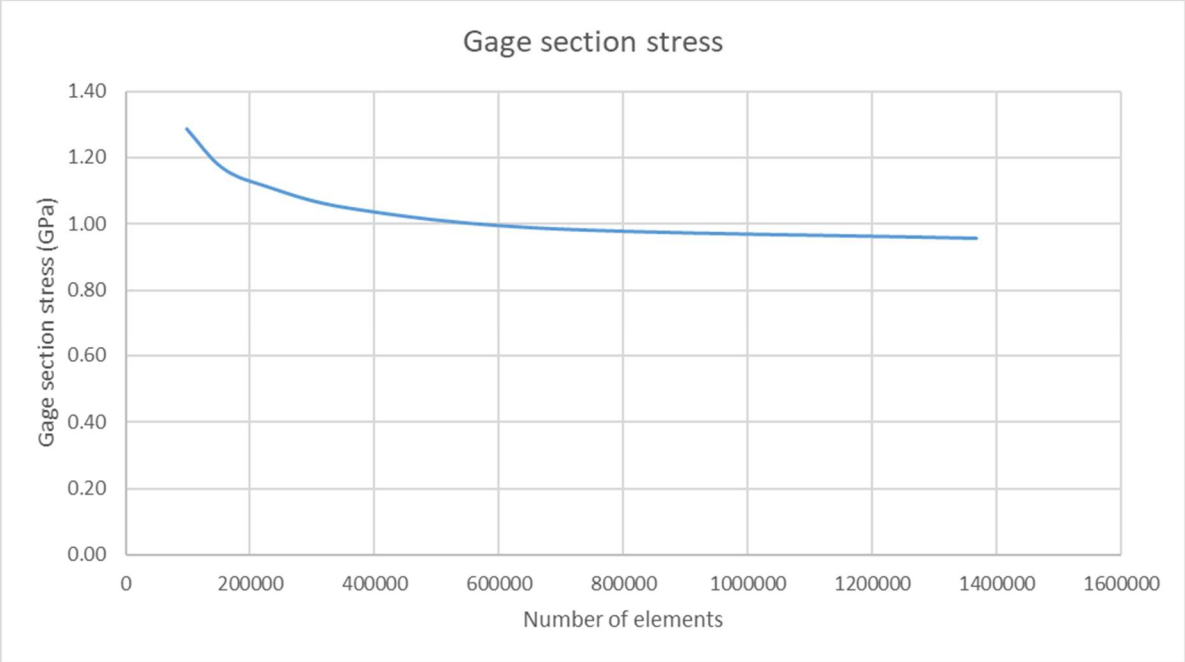

Figure 24 – Mesh convergence plot for the gage section stress of the thin film.

The element shape chosen is tetrahedral due to their adaptability to complex geometries, which is useful for the geometry of the thin film. Once the mesh is determined, the type of study is set to "Stationary," which means not time-dependent. The study is computed, and the results show stress on the thin film that goes from ~0.039 GPa in the gripper section to ~0.39 GPa on the gage section of the thin film. In Figure 25, the FEA results for the residual stress are shown. In them, it can be observed that at the center of the gage section, a stress ~0.39 GPa is present.

After the first study is done, its results are used as input for the second study. The BC for the second study on the mechanical side is the same as they are for study 1. The BC for this device in the heat transfer side is the following:

- The heat transfer mechanism chosen for the model is that of solids. These settings will create two sub-nodes in the model. The first sub-node will set the initial temperature of the device to a value of choice; in this case, room temperature at 20 °C is chosen. The second sub-node is an insulation setting that stops the heat flow of any selected boundaries.

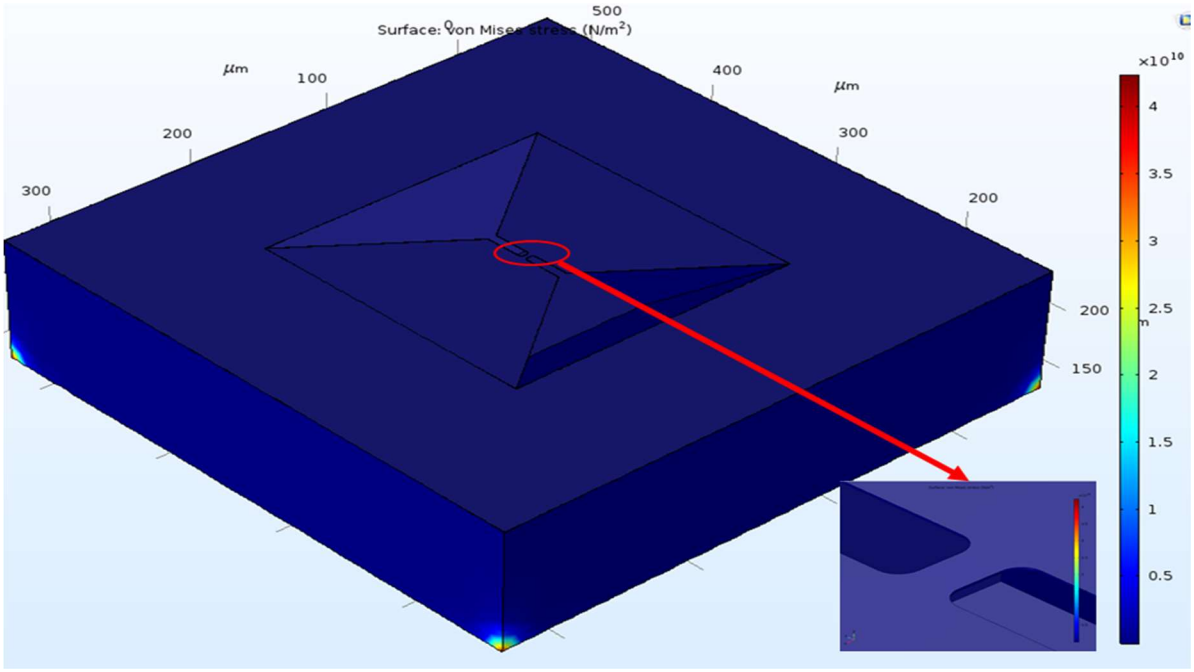

Figure 25. – Simulation results for study 1 to simulate the residual stress of the thin films on a device of shape #1. In the inset, the stress concentration section of the thin film is shown.

- The second BC is to apply the temperature to every boundary as the tube furnace does in the experiment. A temperature increase with time expression is defined for this. The expression used is given by (16):

$$T = 20 + 1.6333 * t \tag{16}$$

Where t is the time, this BC will override the previous insulation sub-node due to the indication of heat being exchanged in the model.

The mesh used for this study is the same mesh used for the previous one. The study is then selected as a "Time-Dependent" study. The time interval is set to go from 0 s to 700 s with increments of 25 s. The results are computed, and when ready, an interpolation for the breaking temperature of the device is done. The initial values and unsolved variables in study 2 are set to be based on the solution of the first study to connect them both. In Figure 26, the results for a device of shape #1, a length of 200 μm, and a breaking temperature of 604 °C.

To corroborate that the results of the first study are being used as initial conditions for the second study, the software is prompted to show the initial conditions of the study, which will display the stress results from study one. The simulation is executed for every device, and the fracture stress can be plotted this way. In this work, due to simulation computation time, ten pairings of each shape will be taken and used for the result analysis. For a better response, every point should be simulated and have its stress included in the curve. A Weibull statistical study is used to analyze this curve.

4.4 Simulation results

Using the values obtained from the FEA simulation, a fracture stress graph is plotted. In Table 2 to 5, the data collected from the simulated devices is presented. The table has the data for stress, length, and breaking temperature of the devices. At the same time, in Figures 27 to 32, the change of the simulated fracture strength with respect to temperature and length is presented. In the X-axis is the breaking temperature or the length of each device, and in the Y-axis is the corresponding stress. The plots show a trend followed by every shape, which is of an exponential increase in the fracture strength.

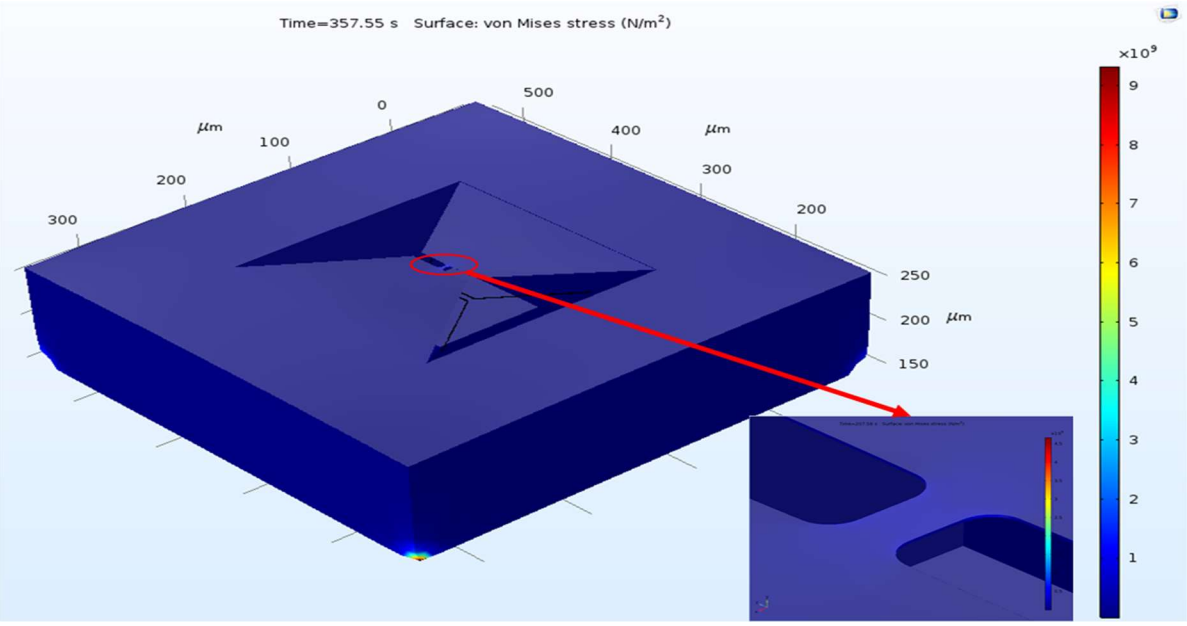

Figure 26. – Simulation results for time-dependent study on a device of shape #1 at a breaking temperature of 604 °C. In the inset, the stress concentration section of the thin film is shown.

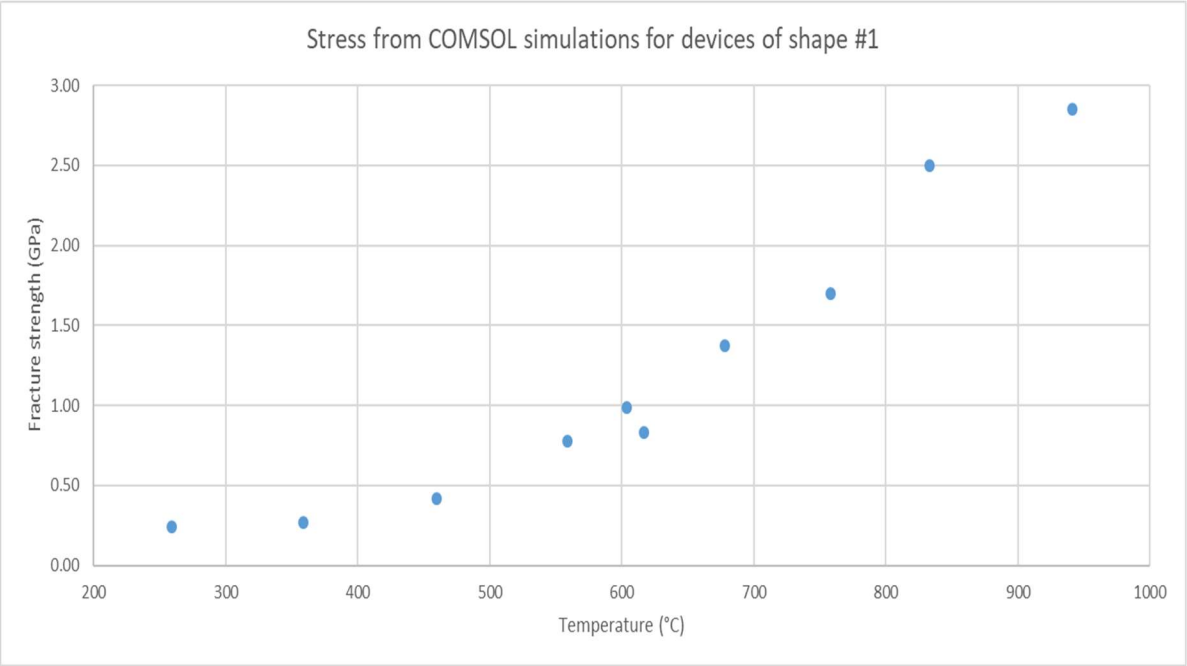

Figure 27. – Variation of the simulated fracture strength of a silicon nitride thin film of shape #1 with respect to temperature.

The results for the fracture strength change with temperature for devices of shape #1 are shown in Figure 27. In these results, it is observed a semi-constant fracture strength up until about 450 °C when the values of fracture strength start to grow exponentially. The values of stress go from 0.245 GPa up to 2.89 GPa. As temperature increases, the change of fracture strength with respect to temperature becomes faster. However, it has to be mentioned that the known trend of descending fracture strength as temperature increases is not observed in this plot.

As for the shape results, in Figure 28, it is possible to observe the change of the fracture with respect to the length of the device. As it was expected, the longer the device is, the lower its fracture strength is; however, it is possible to observe some scattering from this trend. Different from the temperature plot where the change of fracture strength with temperature is smoother and not as scattered, which could be an indicator that although shape and size influence the fracture strength values, the dominant factor is the change in temperature.

Table 3. – Shape #1 devices data used for the Weibull survival plots

Temperature (°C)	Length (µm)	Simulation stress (GPa)
259	205	0.24
359	200	0.27
460	190	0.42
559	196	0.78
604	200	0.99
617	152	0.83
678	193	1.37
758	168	1.70
833	158	2.50
941	156	2.85

The results for the fracture strength change with temperature for devices of shape #1 are shown in Figure 29. In these results, it is observed a semi-constant fracture strength up until about 450 °C, when the values of strength start to grow exponentially. The values of stress go from .260 GPa up to 3 GPa. The same effects observed on shape #1 are applicable for this shape. There is an increase in the fracture strength of the thin films as temperatures increase.

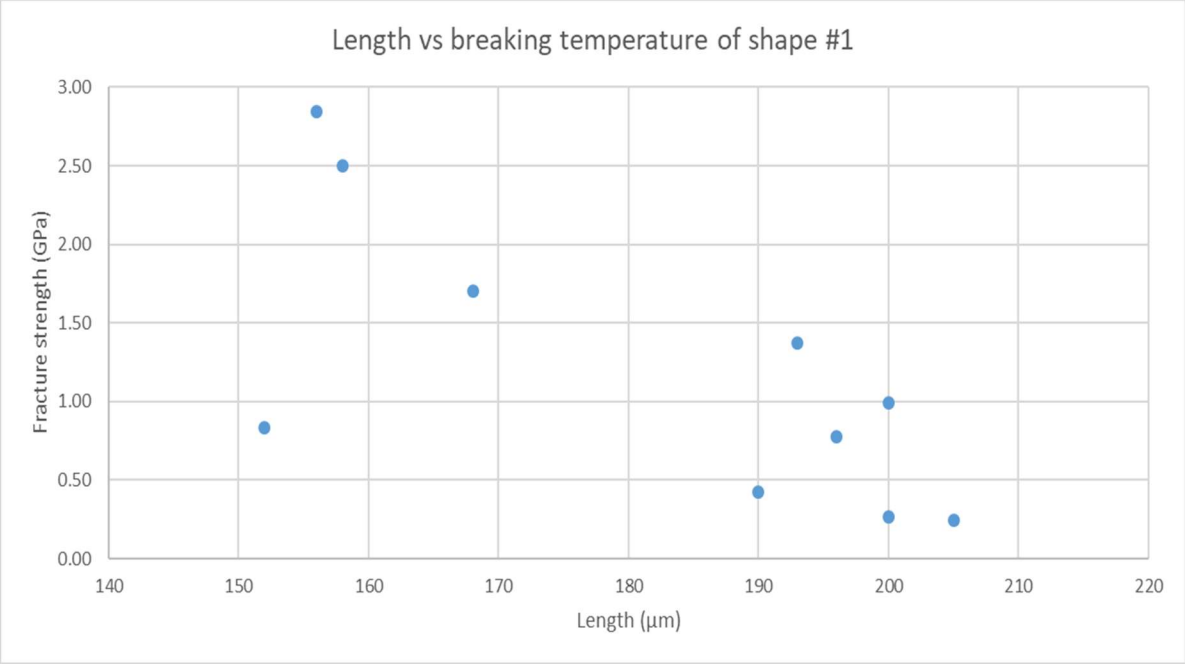

Figure 28. – Variation of the simulated fracture strength of a silicon nitride thin film of shape #1 with respect to length.

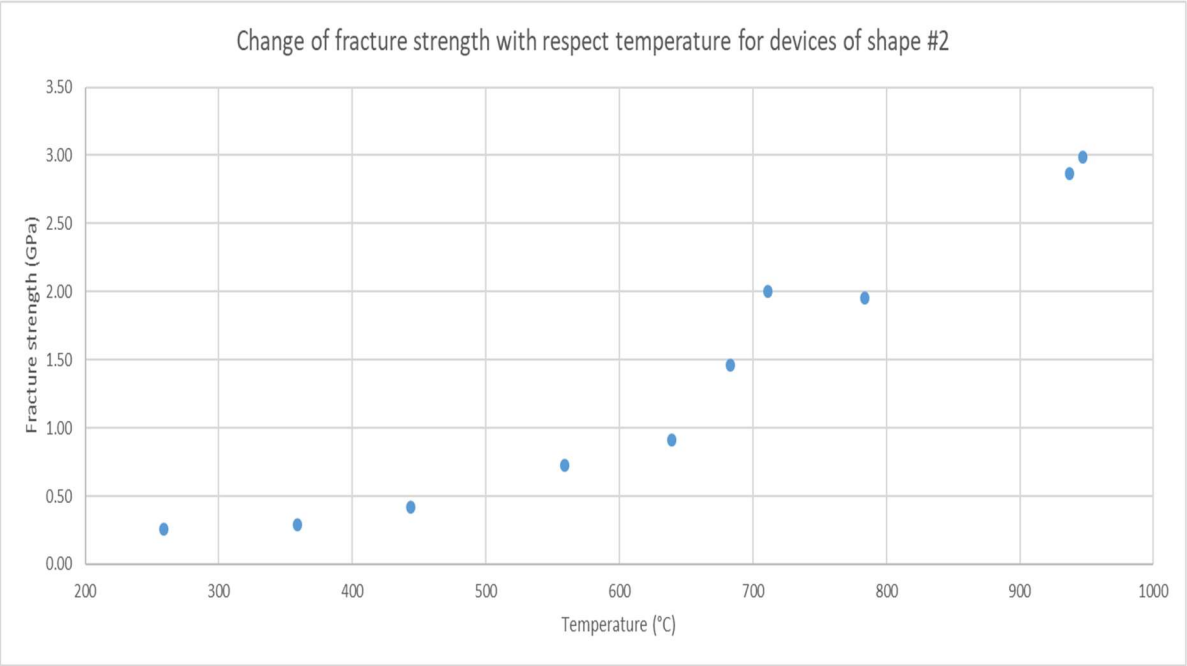

Figure 29. – Variation of the simulated fracture strength of a silicon nitride thin film of shape #2 with respect to temperature.

Table 4. – Shape #2 devices data used for the Weibull survival plots

Temperature (°C)	Length (µm)	Simulation stress (GPa)
259	195	0.26
359	196	0.29
444	189	0.42
559	166	0.73
639	134	0.91
683	186	1.46
711	169	2.00
784	163	1.95
937	147	2.87
947	150	2.99

As for the shape results, in Figure 30, it is possible to observe the change of the fracture with respect to the length of the device. As it was expected, the longer the device is, the lower its fracture strength is; however, it is possible to observe more scatter than for shape #1. As it is the case for shape #1, the scatter is more predominant in the relationship between shape and fracture strength, thus showing a more consistent relationship in its change with temperature

for both shapes.

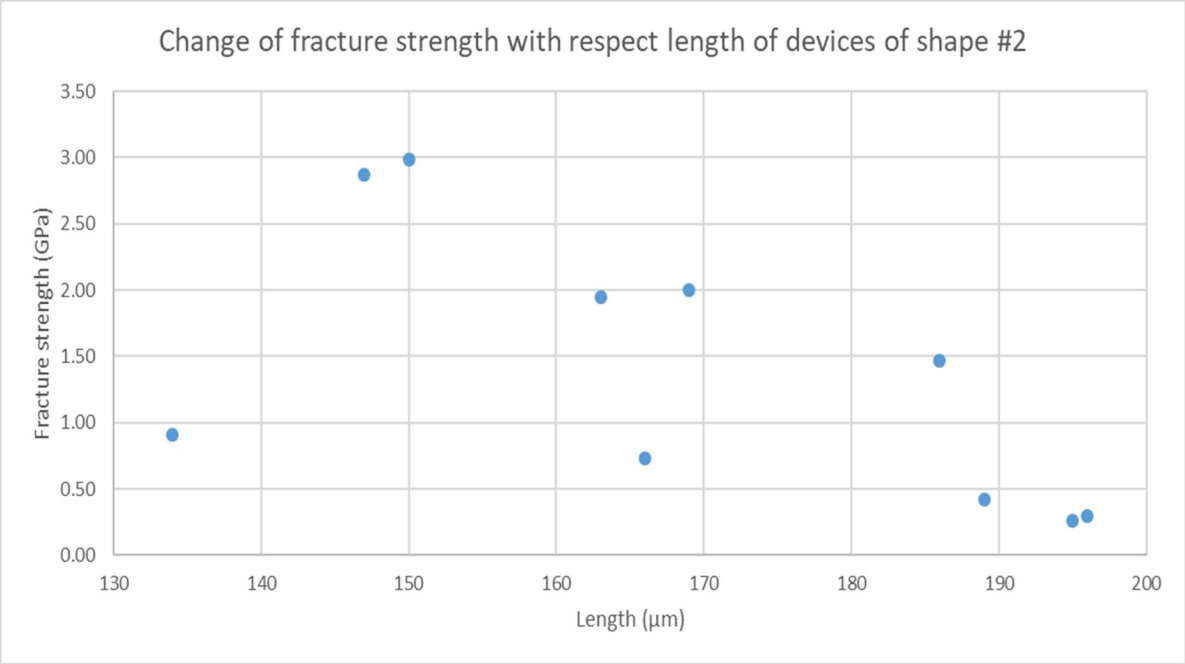

Figure 30. – Variation of the simulated fracture strength of a silicon nitride thin film of shape #2 with respect to length.

The results for the fracture strength change with temperature for devices of shape #1 are shown in Figure 31. In these results, it is observed a semi-constant fracture strength up until about 400 °C when the values of strength start to grow exponentially. The values of stress go from 0.224 GPa up to 2.18 GPa. The same effects observed in previous shapes are applicable for shape #3. There is an increase in the fracture strength of the thin films as temperatures increase. It is possible to observe for this shape a scattering at temperatures that are higher than 900 °C. There is no enough data for the other shapes at these temperatures for a definite conclusion to be reached on this scattering, if it is expected or has a size or shape dependence.

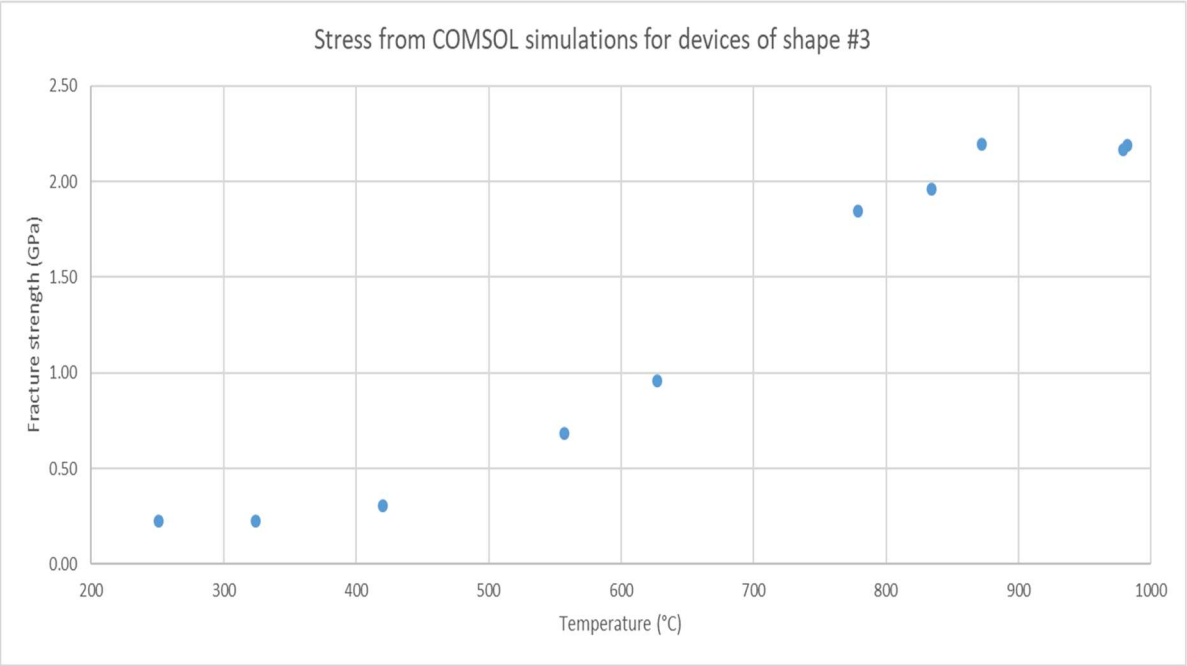

Figure 31. – Variation of the simulated fracture strength of a silicon nitride thin film of shape #3 with respect to temperature.

As for the shape results, in Figure 32, it is possible to observe the change of the fracture with respect to the length of the device. Just as in the other two shapes, the fracture strength and length relationship are maintained. However, this plot shows a more notorious change of fracture as the plot takes the shape of an inverse half parabola. Made evident by the two data points on the left, which have a difference of over 40μm in size with the points to their right, yet their fracture strength is not so different.

Table 5. – Shape #3 devices data used for the Weibull survival plots

Temperature (°C)	Length (μm)	Simulation stress (GPa)
251	172	0.22
324	171	0.23
420	172	0.31
557	169	0.68
627	165	0.96
779	166	1.85
834	142	1.96
872	141	2.19
979	98	2.17
982	98	2.19

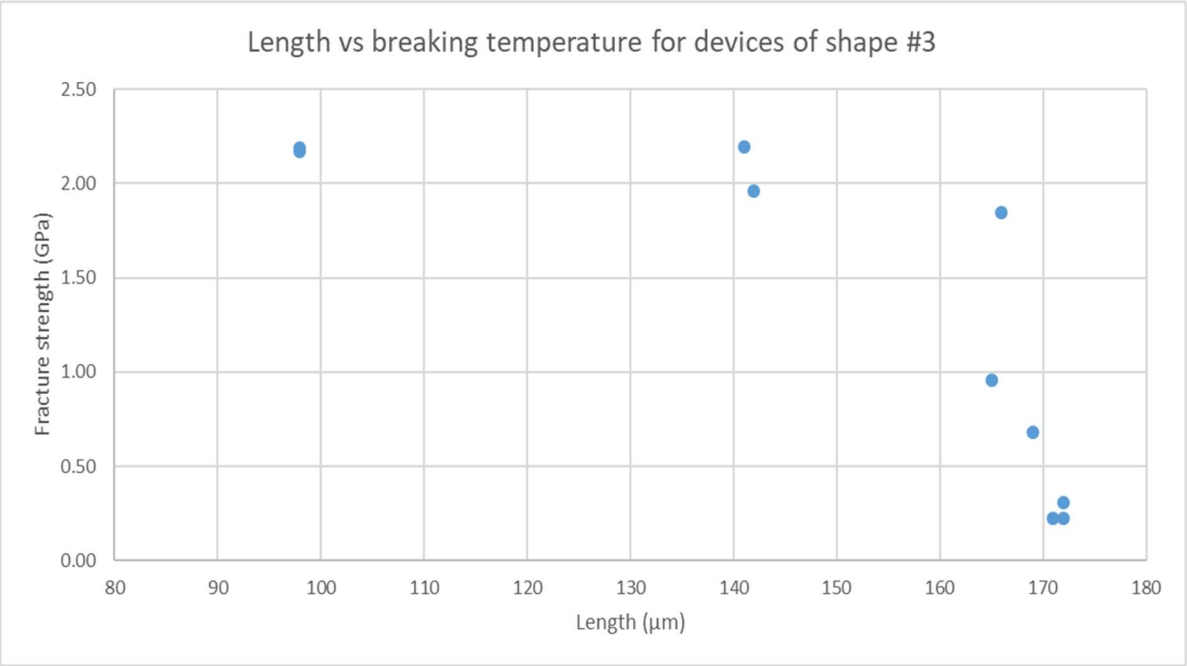

Figure 32. – Variation of the simulated fracture strength of a silicon nitride thin film of shape #3 with respect to length.

In contrast, the results from the three different shapes, in Figure 33 and Figure 34 shows the trend lines followed by the data of Figure 33. The change of the fracture strength with respect temperature of every shape is plotted together. It is observed that the three shapes follow the same trend, which makes the shape effect negligible.

In Figure 35 and Figure 36, a comparison of the curves with the change of the fracture strength with respect geometry for every shape and the trend line for each shape are presented, respectively. Although for each shape, the trend is observable when plotted alone, once they are put together, the scatter is significant, indicating that the stochastic nature of brittle fracture plays a part in the process of fracture at high temperature.

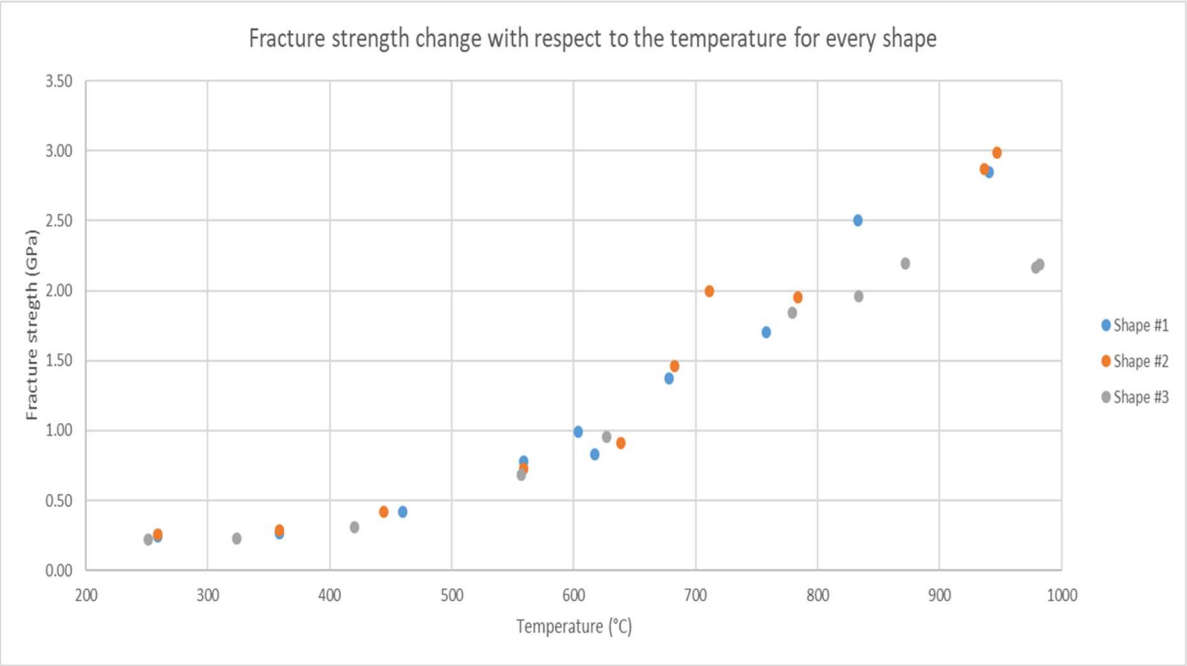

Figure 33. – Simulated fracture strength of all the tested devices. The three curves have an agreeing trend on the behavior of their strength at high temperatures.

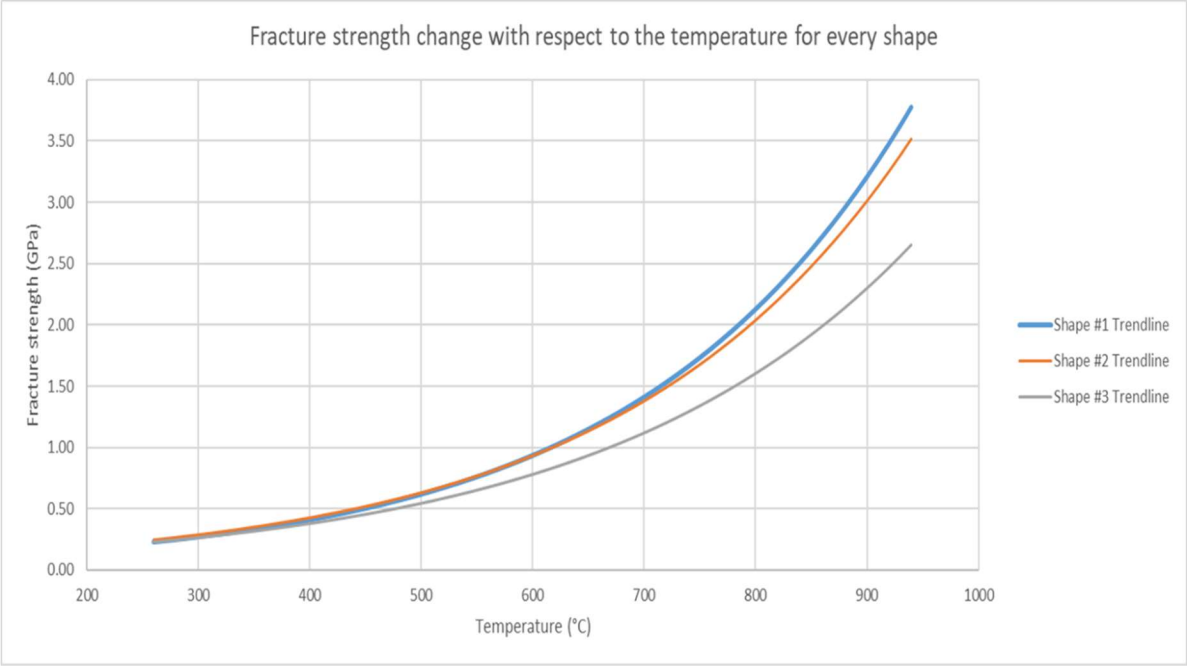

Figure 34. – Trend lines corresponding to the fracture strength change with respect to temperature simulated for the tested devices.

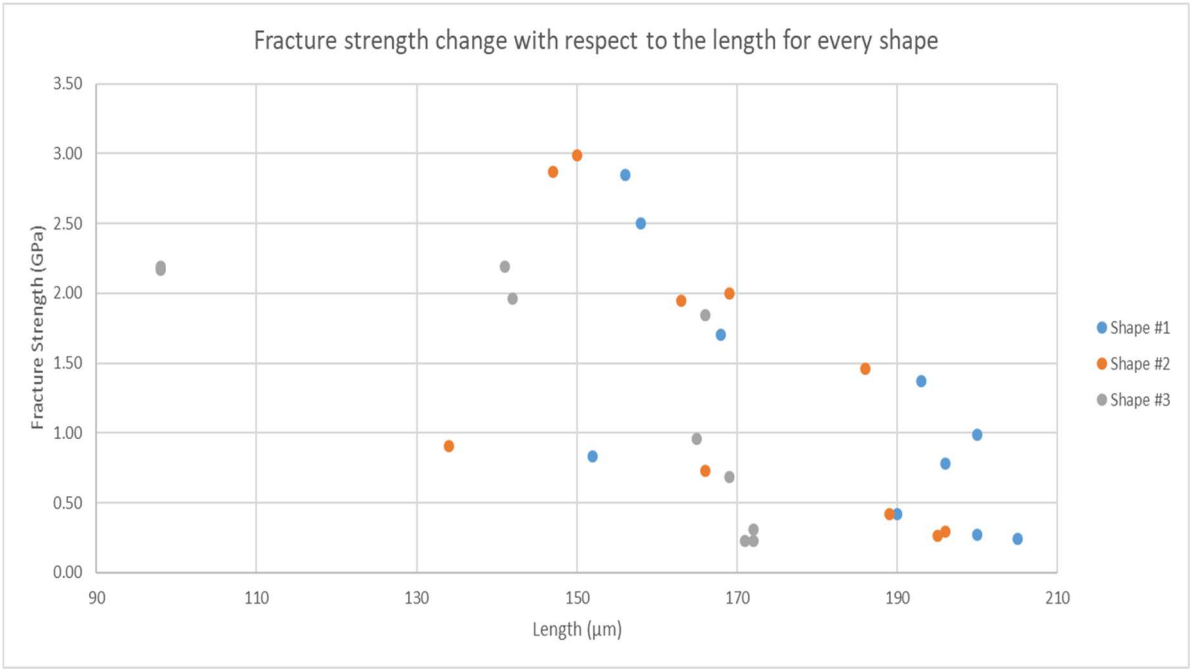

Figure 35. – Change of the simulated fracture strength with respect to the length of the devices for every shape.

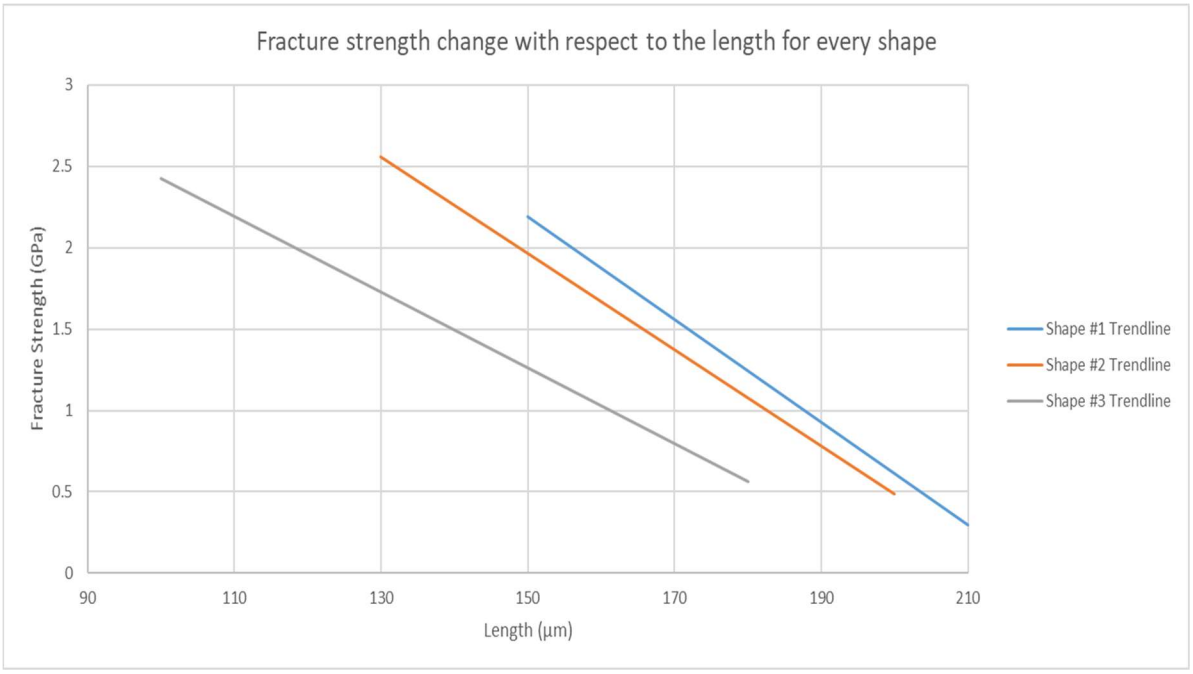

Figure 36. – Trend lines corresponding to the fracture strength change with respect to length simulated for the tested devices.

4.5 Weibull analysis of the fracture data

The data for every shape is processed using the Weibull distribution. The Weibull survivability plot of the data set can be determined by the set of equations presented in Chapter 2 (see section 2.4.2.1). The first step to achieve this is to use linear regression to relate the fracture strength with the probability of failure. For this, the parameters m and σ_0 of the distribution are determined. The parameter m is determined from the linear regression plot slope in Figure 37. Equation (3) is used, and the obtained value for m is 1.26. The value of m is an expression of the degree of scattering of the plot, the lowest the number the least scattering on the data. This value is used in (5) to determine the σ0 parameter, which indicates the stress at which 63.2% of the devices will have failed, obtaining a value of 1.34 GPa. The plot in Figure 37 is also representative of the degree at which the Weibull distribution can represent the studied data set. The data points distributed along with the linear fit, proving that the Weibull distribution and its linear regression can adequately relate the fracture strength data to the breaking temperature data.

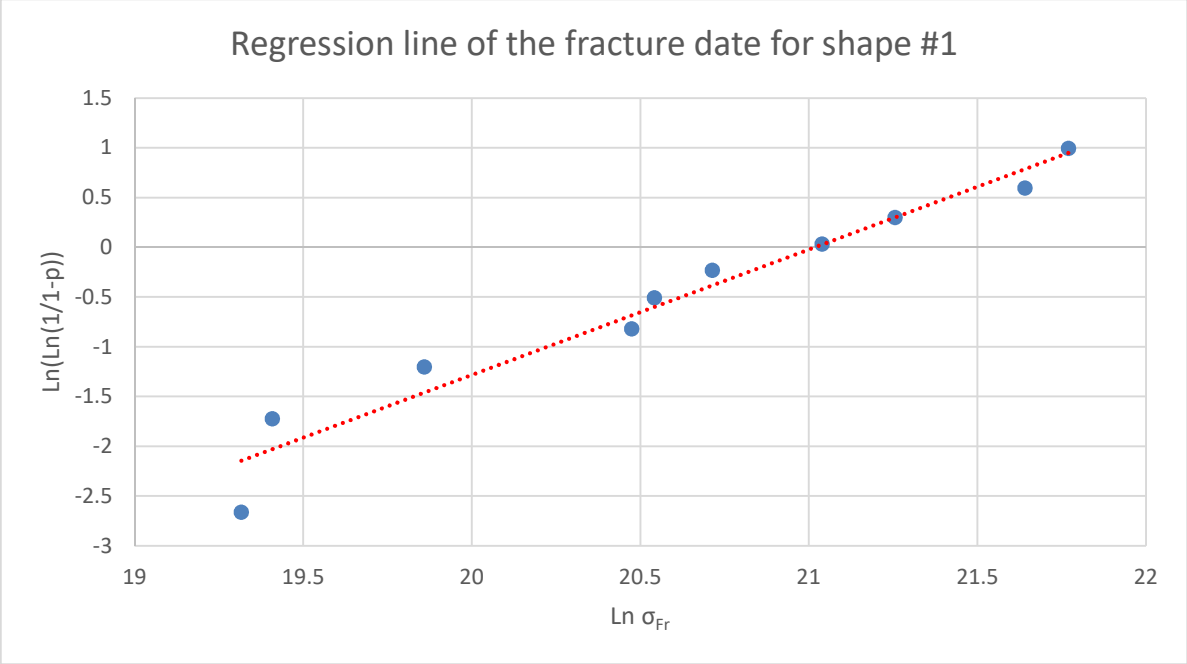

Figure 37. – The simulated fracture strength of the devices of shape #1 represented in a Weibull plot. A linear regression fit demonstrates the adequacy of the use of the distribution.

Using the Weibull parameters of dispersion and characteristic life in equation (2) allows for the calculation of the survival rate of the material when submitted at different stresses. In Figure 38, the survival rate plot is presented where the probability of a device to resist an indicated amount of stress is visualized. In this distribution, it can be determined that there is an 89% probability of survival for the structure when operating to stresses below 0.244 GPa at temperatures underneath 1000 °C. Thus, when a device is fabricated using Si_xN_y for applications where temperatures of 1000 °C are present, it is predicted that the stress of 0.244 GPa or less will not affect the device performance. The device can be defined as being reliable under these conditions.

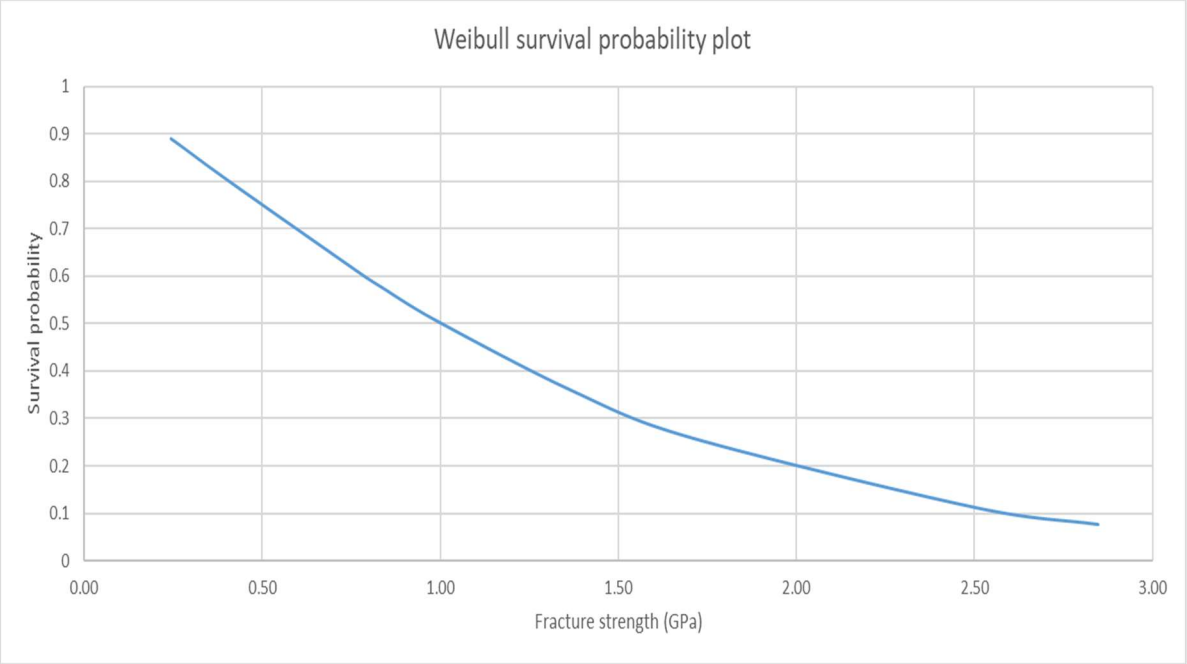

Figure 38. – Survivability plot of the determined values of fracture strength of thin films of shape #1. The devices will have around an 89% probability of being reliable when submitted to stresses of 0.244 GPa at temperatures up to 1000 °C

The parameter *m* is determined from the linear regression plot slope in Figure 39 for devices of shape #2. The values for *m* and σ0 are 1.18 and 1.56 GPa, respectively. Similarly, as it happened for shape #1, the data points distributed along with the linear fit, proving that the Weibull distribution to be the right fit to model this data. The value from m shows as well that

there is a similar dispersion as shape #1. Using the Weibull parameters of dispersion and characteristic life in equation (2), the survival rate of the material is calculated. In Figure 40, the survival rate plot is presented where the probability of a device to resist an indicated amount of stress is visualized. In this distribution, it can be determined that there is an 88% probability of survival for the structure when operating to stresses below 0.26 GPa at temperatures underneath 1000 °C. Thus, when a device is fabricated using Si_xN_y for applications where temperatures of 1000 °C are present, it is predicted that the stress of 0.26 GPa or less will not affect the device performance. The device can be defined as being reliable under these conditions.

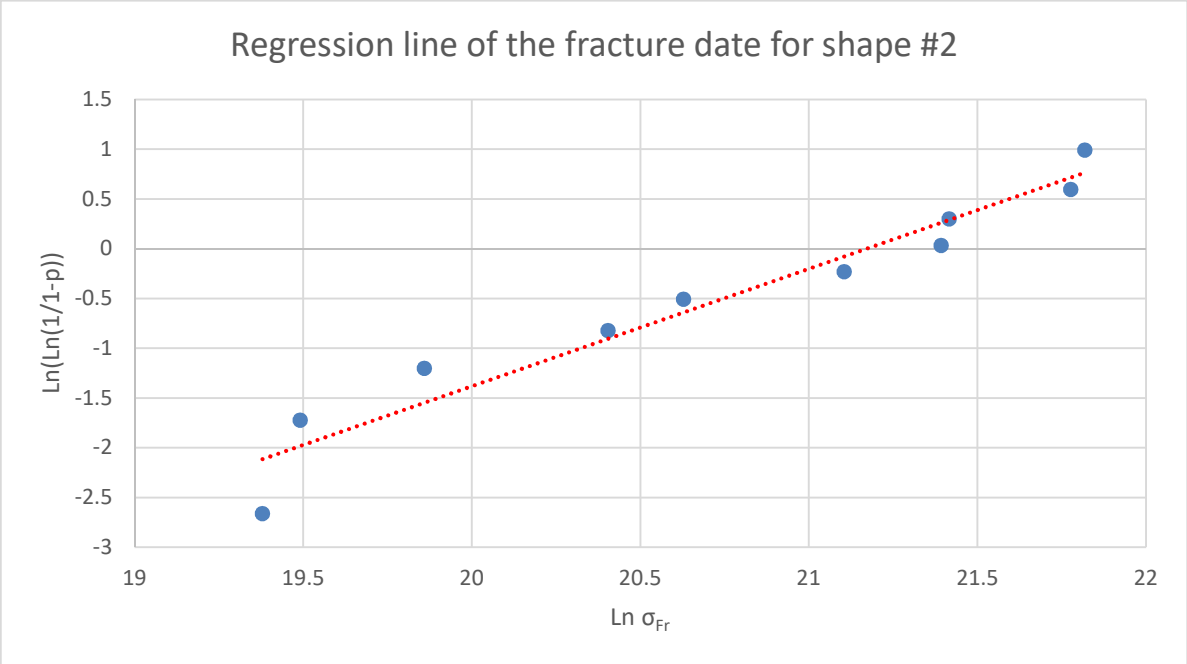

Figure 39. – The simulated fracture strength of the devices of shape #2 represented in a Weibull plot. A linear regression fit demonstrates the adequacy of the use of the distribution.

The parameter m is determined from the linear regression plot slope in Figure 41 for devices of shape #3. The values for m and σ0 are of 1.07 and 1.48 GPa, respectively. Similarly, as it happened for the other two shapes, the data points distributed along with the linear fit with some more concentration at the ends of the fitting line. The value from m shows as well that there is a smaller dispersion of the data for this shape with respect to the other two. Using the

Weibull parameters of dispersion and characteristic life in equation (2) allows for the calculation of the survival rate of the material when submitted at different stresses. In Figure 42, the survival rate plot is presented where the probability of a device to resist an indicated amount of stress is visualized. In this distribution, it can be determined that there is an 87.5% probability of survival for the structure when operating to stresses below 0.22 GPa at temperatures underneath 1000 °C. Thus, when a device is fabricated using SixNy for applications where temperatures of 1000 °C are present, it is predicted that the stress of 0.22 GPa or less will not affect the device performance. The device can be defined as being reliable under these conditions.

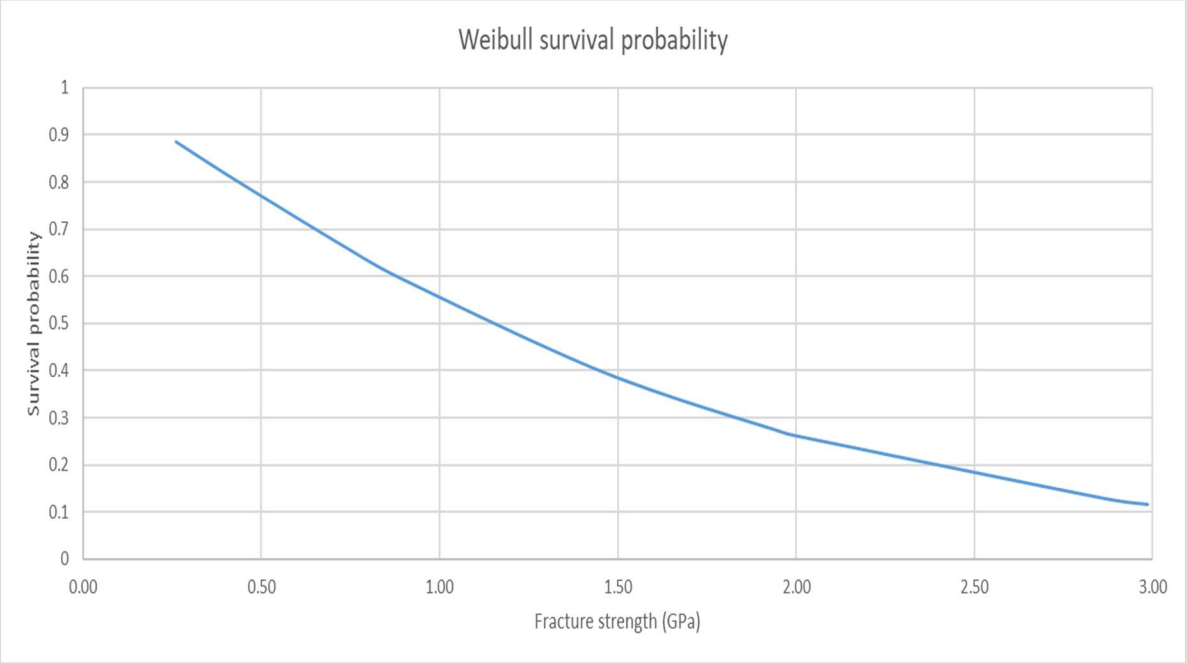

Figure 40. - Survivability plot of the determined values of fracture strength of thin films of shape #2. The devices will have around an 88.5% probability of being reliable when submitted to stresses of 0.26 GPa at temperatures up to 1000 °C

In Table 6, a summary of the values obtained for the Weibull parameters for shape #1, as well as the median, mean, and standard deviation of the distribution, are presented. The spread parameter "m" is very similar for every shape, and the characteristic life parameter goes through a negligible change, which shows consistency between the three shapes deeming the shape change as not affecting the fracture strength.

Table 6. – Weibull parameters for the curve of each tested shape

Parameter	Shape #1	Shape #2	Shape #3
m	1.26	1.18	1.07
σ_0	1.34 GPa	1.56 GPa	1.48 GPa

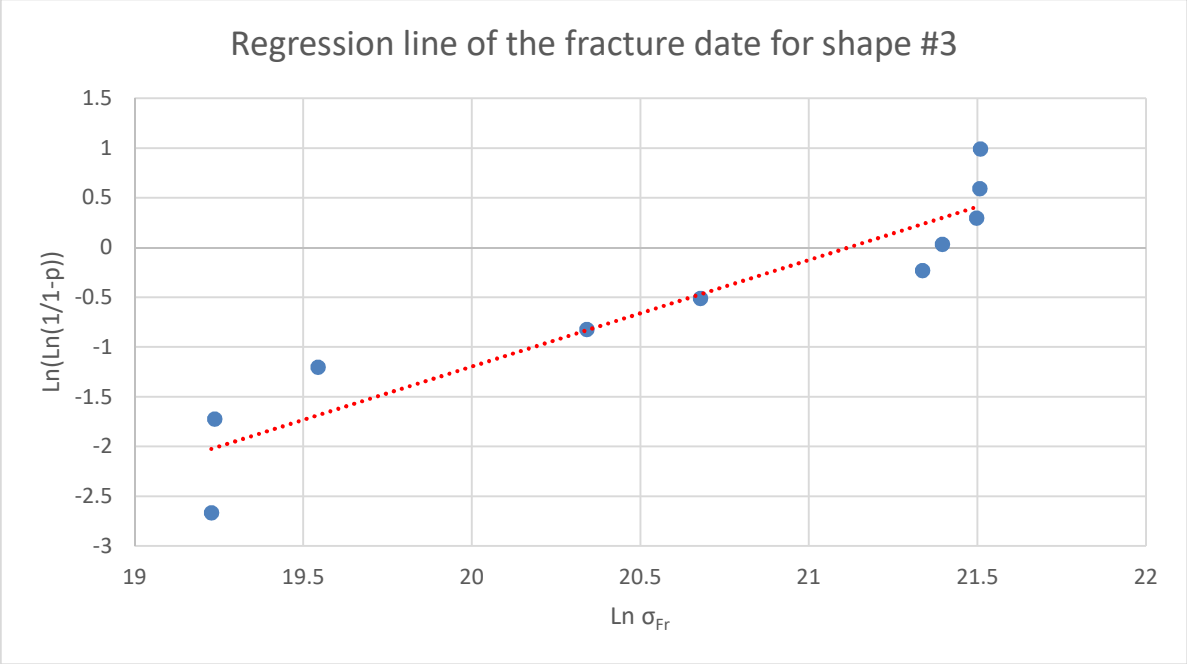

Figure 41. – The simulated fracture strength of the devices of shape #3 represented in a Weibull plot. A linear regression fit demonstrates the adequacy of the use of the distribution.

The failure probability is given by extracting the survivability rate from 1. The results for all the shapes are compared at a 20% probability of failure for a meaningful comparison of the obtained data. It is found that the fracture strength is very similar to every shape. For devices of shape #1, the fracture strength is 0.4 GPa, for devices of shape #2 the fracture strength is 0.44 GPa and for devices of shape #3 the fracture strength is of 0.37 GPa. The values have a variation of only 0.07 GPa, which given their difference in geometry corroborates the impact temperature has on the variation of fracture strength over geometry.

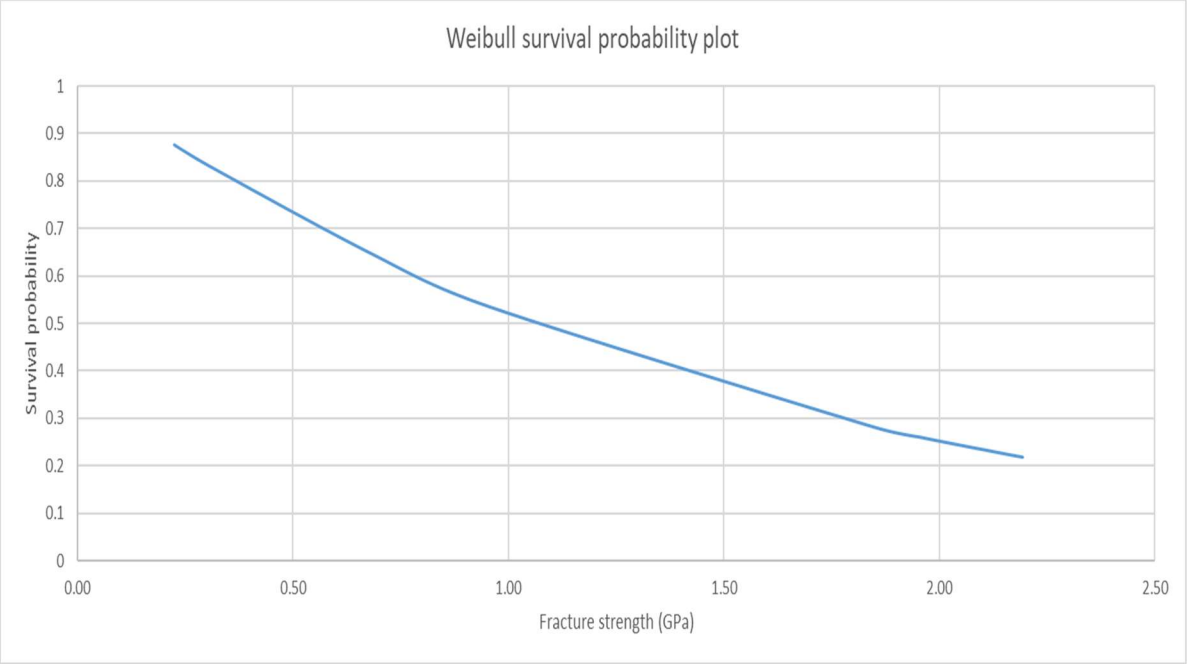

Figure 42. – Survivability plot of the determined values of fracture strength of thin films of shape #3. The devices will have around an 87.5% probability of being reliable when submitted to stresses of 0.22 GPa at temperatures up to 1000 °C.

4.6 Discussion

The lowest values obtained in the presented work range from 0.22 GPa to 0.26 GPa, then the fracture strength begins to increase as temperature rises. Previous values obtained for the fracture strength of silicon nitride thin films at room temperature from literature are used for comparison, however, it is important to keep in mind there is a difference in the temperature in the values obtained in this research and the values obtained by other groups. Cardinale and Tustison found the value of the fracture of silicon nitride thin films to range from 0.39 GPa to 0.42 GPa, and Milek reported a value of 0.46 GPa [55], [56]. The trend observed in the data from this experiment matches the trend for the bulk properties of SixNy by remaining constant up to temperatures of ~400 °C matching the results from other works [7]. In the obtained data, the fracture strength increases as the temperature increase, which opposes the results obtained by other research groups when testing materials at high temperatures. There are reports where the fracture strength of Si_3N_4 has been confirmed to decrease as temperature increases, Qian et al. reported a decrease in α-Si_3N_4 yield strength from 8.7 GPa at 400 °C to 4.0 GPa at 1234

°C [57]. Although the results are from macro-sized samples, the fracture strength is expected to follow the same trend at the micro-scale. Thus, this discussion will be focused on the possible reasons for the fracture strength to have an increasing trend.

The first possible reason for the variation is the difference in geometries from one device to the other, which includes the change of shape and the change of length. In the case of the shape change, it has been shown in the previous section, in Figure 33, how the curves for each of the three shapes follow the same trend. When the results are compared with the Weibull analysis for each shape, a difference of 0.7 GPa was obtained at a 20% failure rate, thus the the can be considered not impactful. The similarity between the three shapes results allows for them to be plotted together, and the resulting curve looks uniform with an expected scatter. In the case of the length change, in Figure 35, it can be observed that there is an effect from its variation in the fracture strength. The expected result is an increase in the value of fracture strength as the devices decrease in size. However, it is possible to observe that the smallest device is not the one with the highest fracture strength. There is also a higher degree of unordered scattering in the data due to the brittleness of the tested material. In the research done by Sharpe et al. and Tsuchiya et al., a change in the values of fracture strength can be observed in their studies for Polysilicon as they vary the length of their specimens. However, from their results, the variation in fracture strength is 100% for Sharpe et al. and 35% for Tsuchiya et al., while for this study, the change is ~2000% [58], [59]. It is also important to mention that the difference in length was 270 μm for Tsuchiya et al., and 3750 μm for Sharpe et al., while in this study, the most significant difference between the length of the devices is 72 μm. Therefore, a drastic increase in the fracture strength due to this variation is highly unlikely.

The previous conclusions create a need to take a closer look into the effect high temperature has in the device materials as individual units and how that affects their collective behavior. As was mentioned in previous chapters, Si_3N_4 should not be affected by the temperature at temperatures below 1000 °C. However, in the case of Si temperatures as low as 500 °C, degrade the mechanical structure of the material, which would be detrimental to the behavior of the device due to the effect this degradation would have on the CTE mismatch interaction. In Figure 43, a diagram detailing the change in the CTE mismatch interaction is shown. The

design of the device is based on tensile stress being applied by the faster expansion of the substrate with respect to the slower expansion of the thin film. However, as the Si substrate mechanically degrades, this tensile stress would also be affected. As temperature increases, the Si becomes softer, which would cause a change at the interface where both materials meet, which will cause that the CTE mismatch decreases its effect. The causes for this deformation can be attributed to thermal deformations in the interface of the materials or even creep. If the temperature and stress are high enough, creep can happen in the material even at low temperatures. Regardless of the presence of creep in the substrate, thermal deformations still will affect the substrate, causing deformation and altering the expansion of the substrate [60]. The deformation of Si has been observed by different research groups at temperatures as low as 300 °C, which would support the theory of thermal deformations occurring in the boundary of both materials [61], [62]. As the simulation is configured, the CTE mismatch has no BC or applied thermal effect; thus, in the simulation, it will be unaffected, which makes the stress to follow the profile of the thermal strain. The thermal strain is given by the difference of coefficient of thermal expansion, which is shown in Figure 44, it can be appreciated that the exponential increase of the fracture strength follows that of an unaltered thermal strain. Thus, the fracture strength has an increasing trend due to the CTE mismatch, not including the effect of the thermal deformation and possible creep in the simulation.

There are two options to countermeasure this effect using the current approach. The first option would consist of changing the substrate material to a material that is not affected by temperatures below 500 °C, like sapphire; however, that would introduce fabrication challenges and drive the cost of the test up. Another concern of this approach is the availability of the material properties variation with respect to the temperature for the selected new material. The second option is to implement a modification in the devices that allows for the monitoring of strain throughout the experiment, which would allow for the accurate modeling of the change in the CTE mismatch as Si deforms. In chapter 6, a more in-depth discussion of these improvements is presented.

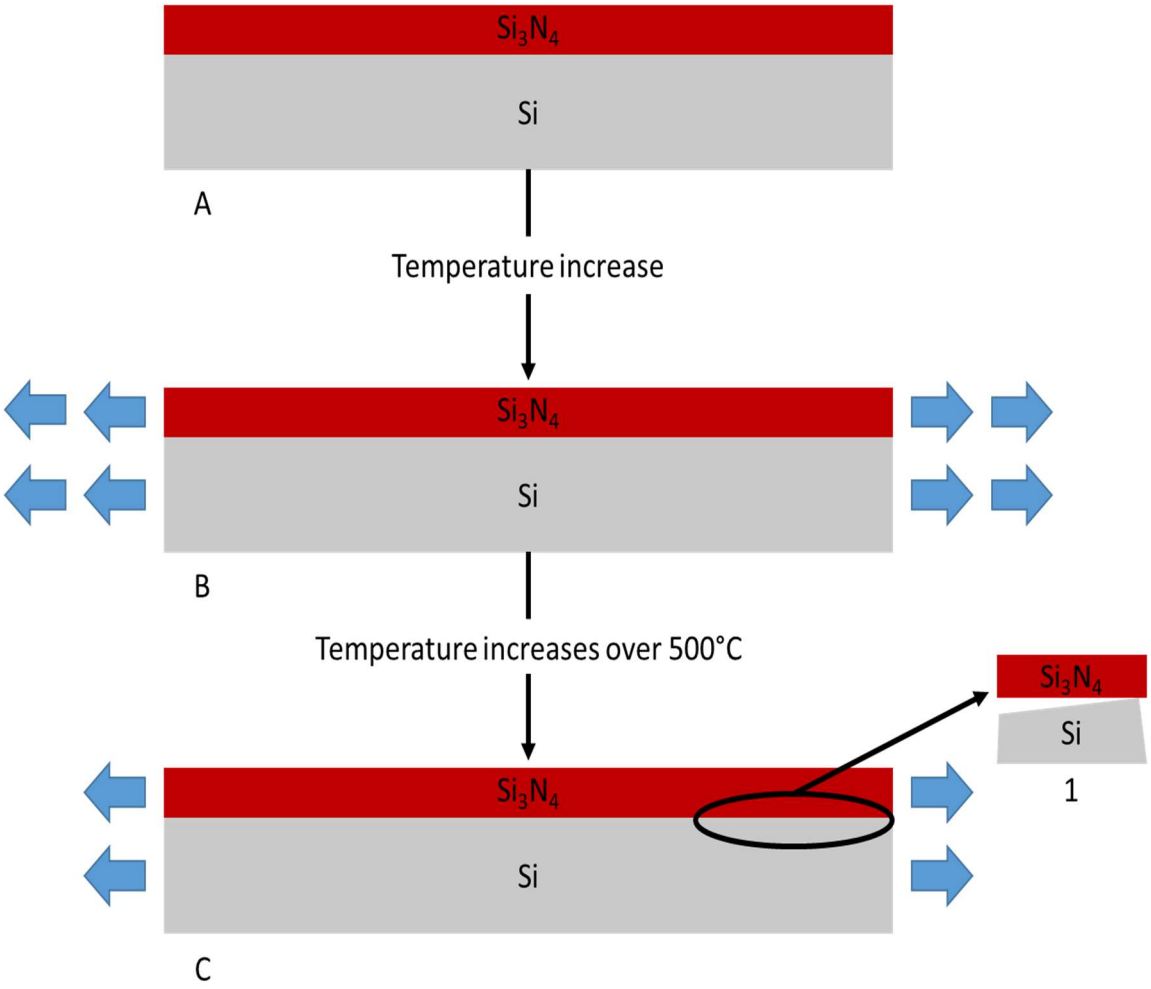

Figure 43. – Diagram of the interaction between thin film and substrate as temperature increases. In A, the room temperature configuration of the material is shown. In B, the displacement of both material layers begins as temperature increases. In C, when the temperature goes beyond 500 °C, the deformation of the material (inset 1) reduces the tensile stress applied to the film.

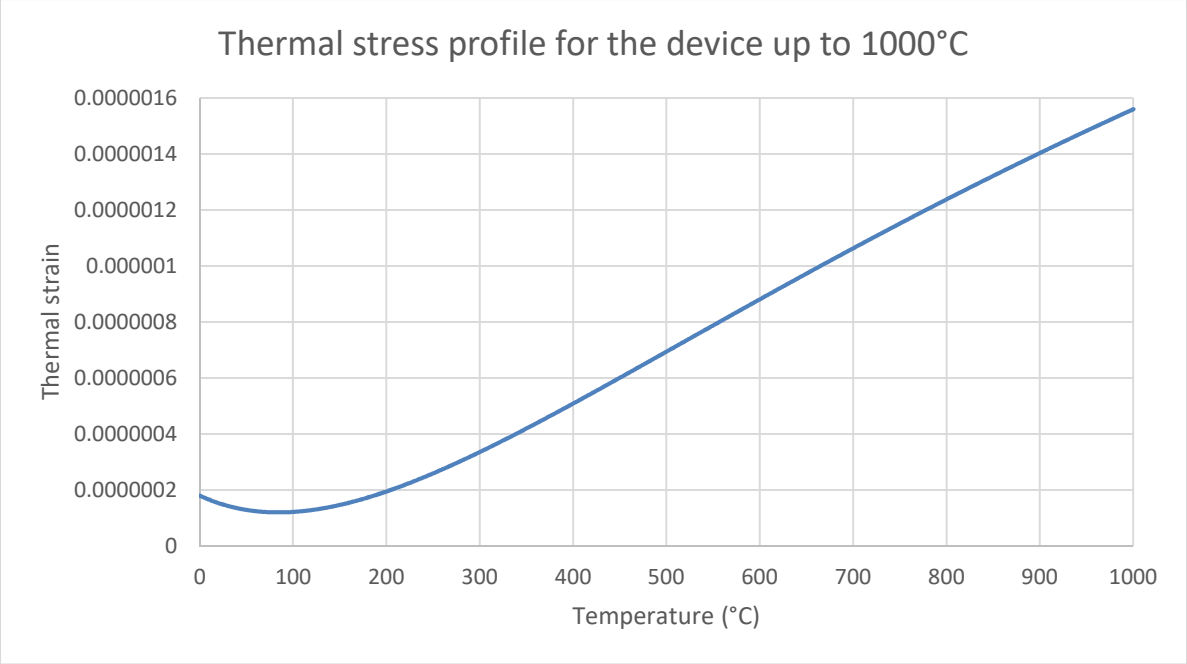

Figure 44. – Thermal strain profile of the tested devices. The trend follows the trend obtained for the fracture strength from the FEA simulations.

Chapter 5
Analytical model and comparison

Parts of this chapter are reprinted in an adapted form with permission from © 2018 IEEE [48]

A. N. Gonzalez, E. Brace, and P. Nieva, "Size and Shape Effect in the Determination of the Fracture Strength of Silicon Nitride in MEMS Structures at High Temperatures," in *2018 IEEE 68th Electronic Components and Technology Conference (ECTC)*, 2018, pp. 2457–2463.

5.1 Analytical model

The difference in shape and dimensions are considered during mechanical analysis. The sum of the total strain, ε_{Total}, applied to the structure during heating defines the basis of mechanical modeling (17). Due to the symmetry of the thin film, the mechanical analysis is done just from a one-quarter section of the thin film. Mechanical strain is calculated from the forces interacting at the interface of the substrate and thin film and the thermal strain due to the thermal expansion of the materials as; the temperature is increased.

$$\varepsilon_{Total} = \varepsilon_{Mechanical} + \varepsilon_{Thermal} \tag{17}$$

The mechanical strain, $\varepsilon_{Mechanical}$, is defined as a primary relationship of the stress, σ_{Film}, on the thin film divided by the film's Young's modulus, E_{Film}, and the thermal strain, $\varepsilon_{Thermal}$, is defined as the difference between the thermal strains parallel to the surface of substrate and thin film, ε_{ThFilm} and ε_{ThSubs} respectively, (18):

$$\varepsilon_{Total} = \frac{\sigma_{Film}}{E_{Film}} + (\varepsilon_{ThFilm} - \varepsilon_{ThSubs}) \tag{18}$$

In equation (18), the thermal strain can be expressed as the change of the coefficient of thermal expansion from room temperature to the breaking temperature for each material of the device. At the same time, the mechanical stress is expressed as the change through the length of the device, L, of the sum of the forces that affect the thin film. The mechanical stress, σ_{Film}, on the thin film is assumed to be distributed uniformly on the film due to the dimensions of the

device. Using these expressions, formulating the strain as the change of length of the structure and solving for the increment of length due to the shift from initial temperature, T_0, to final temperature, T, (18) can be rewritten as (19):

$$\Delta\frac{L}{2} = \int_0^{\frac{L}{2}} \left(\frac{F}{A(x) * E_{Film}} + \left(\int_{T_0}^{T} \alpha_{Film}(T)dT - \int_{T_0}^{T} \alpha_{Subs}(T)dT \right) \right) dL \tag{19}$$

In equation (19) F is the assumed force distributed through the thin film bridge due to the mechanical stress uniform distribution, $\alpha_{Film}(T)$ and $\alpha_{Subs}(T)$ are the CTE of the thin film and the substrate depending on the temperature respectively, and the term $A(x)$ represents the variable cross-sectional area of the thin film bridge. Equation (19) assumes the strain of thin-film and the strain of the substrate to be equal. The parameter $A(x)$ has been substituted by expression of the cross-sectional area of the thin film (20):

$$A(x) = t_{Film} * f(x) \tag{20}$$

Where $f(x)$ represents the variable cross-section of the shapes tested, and it is defined by the width of the gripper section at an arbitrary position "x." Each shape has a different gripper cross-sectional variations; thus, each shape has its $f(x)$ expression. Shape #1 and shape #2 have a similar cross-section, while shape #3 is entirely different. In Figure 45, the cross-sectional area of the different devices is shown, using it as a reference, an expression for the $f(x)$ for each shape can be determined [50]. The equation that defines $f(x)$ for shape #1 is (21):

$$\int_0^{\frac{W_{Gage}}{2}} (f_1(x))^{-1}dx + \int_{\frac{W_{Gage}}{2}}^{\frac{L}{2}} \left(f_2(x, \frac{L}{2}) \right)^{-1} dx \tag{21}$$

Where L is the length of the device, and x is the position on the X-axis on the thin film. The variables f_1 through f_5 are shape factors that define the area under various geometric features, shown in Figure 45, as integrated orthonormal to the X-axis. Variable f1 is set by the radius path length, as shown in Fig. 45 and is determined by (22):

$$f_1(x) = b - \sqrt{\left(\frac{W_{Gage}}{2}\right)^2 + x^2} \tag{22}$$

Where b indicates the Y-direction distance between the middle of the gage section and the radius point of tangency to the flat segment of the gripper, as shown in Figure 45, the term f2 in (21) is given by (23), which is the area under the linear segment of the gripper, shown in Figure 45.

$$f_2\left(x, \frac{L}{2}\right) = \left(\frac{L}{2} - h - b\right) * \frac{x - \frac{L}{2}}{\frac{L}{2} - \frac{W_{Gage}}{2}} + \frac{L}{2} \tag{23}$$

Where *h* is the length of the flat segment of the width. By solving (21), the shape factor for every thin film of shape #1 is determined. For shape #2, the shape factor is given by (24):

$$\int_0^{\frac{W_{Gage}}{2}} (f_1(x))^{-1} dx + \int_{\frac{W_{Gage}}{2}}^{\frac{L}{2}} \left(f_3\left(\frac{L}{2}\right)\right)^{-1} dx \tag{24}$$

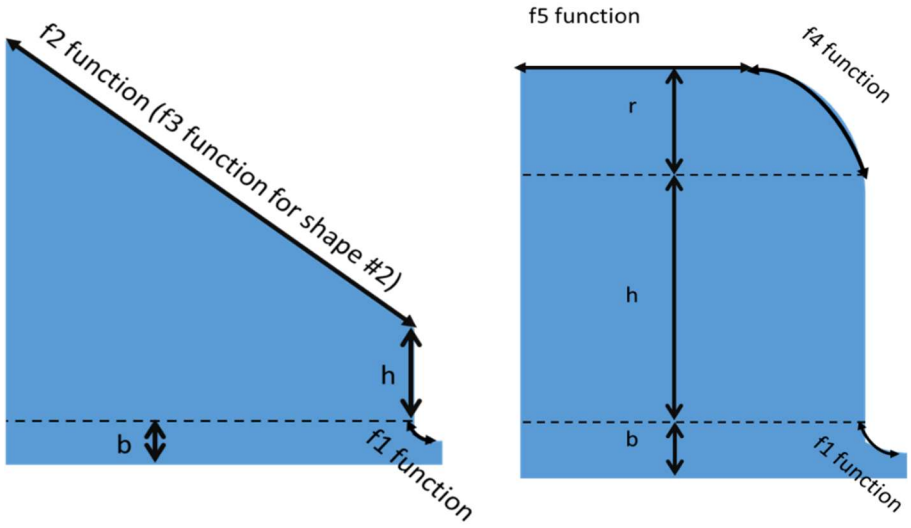

Figure 45. – Gripper section dimensions for each shape are shown in detail. On the left, the profile for shape #1 and shape #2 is shown; on the right, the shape #3 profile is shown.

Where *f3* is defined for this shape similarly to *f2* as given in (25):

$$f_3\left(\frac{L}{2}\right) = \frac{L}{2} - \frac{W_{Gage}}{2} + h + b \tag{25}$$

By solving (24), the shape factor for every thin film of shape #2 is determined. For shape #3, the shape factor is given by (26):

$$\int_0^{\frac{W_{Gage}}{2}} \left(f_1(x)\right)^{-1} dx + \int_{\frac{W_{Gage}}{2}}^{\frac{W_{Gage}}{2}+2b} \left(f_4(x)\right)^{-1} dx + \int_{\frac{W_{Gage}}{2}+2b}^{\frac{L}{2}} \left(f_5\left(\frac{L}{2}\right)\right)^{-1} dx \qquad (26)$$

Where f_4 is defined by the outside edge of the radius, r_a, shown in Figure 45. The radius variable cross-sectional area is given by (27):

$$f_4(x) = h + \sqrt{(2b)^2 - (x - (\frac{W_{Gage}}{2} + 2b)^2} \qquad (27)$$

The constant width gives the term f5 once the radius of f4 reaches its tangential point on the X direction, shown in Figure 45, and is defined by (28):

$$f_5\left(\frac{L}{2}\right) = \frac{L}{2} \qquad (28)$$

By solving (26), the shape factor for shape #3 can be determined. These shape factors will impact the calculated forces on the device and the effective fracture strength of the material. Once the shape functions for every shape are defined, the expression on (19) is solved for the force, F, (29):

$$F = \frac{E_{Film} * t_{Film} * \frac{L}{2} * (\int_{T_0}^{T} \alpha_{Subs}(T)dT - \int_{T_0}^{T} \alpha_{Film}(T)dT)}{\left[\int_0^{\frac{L}{2}} \frac{dx}{f(x)}\right]} \qquad (29)$$

The maximum stress is expected to reach its maximum at the stress concentration gage. Thus, it can be determined that the film stress, σ_{Film}, is equal to σ_{Max}. The stress σ_{Max} is given by (30):

$$\sigma_{Max} = \frac{F}{A} = \frac{F}{t_{Film} * \frac{W_{Gage}}{2}} \tag{30}$$

An expression for the fracture stress using (29) and (30) can be obtained, and it is shown in (31):

$$\sigma_{Fr} = \frac{E_{Film} * t_{Film} * \frac{L}{2} * (\int_{T_0}^{T} \alpha_{Subs}(T)dT - \int_{T_0}^{T} \alpha_{Film}(T)dT)}{\frac{W_{Gage}}{2} * \left[\int_0^{\frac{L}{2}} \frac{dx}{f(x)}\right]} \tag{30}$$

The residual stress from the fabrication of the devices needs to be included as it was done for the FEA model for the analytical expression to be complete. Therefore, the final equation is given by (31):

$$\sigma_{Fr} = \sigma_{res} + \frac{E_{Film} * t_{Film} * \frac{L}{2} * (\int_{T_0}^{T} \alpha_{Subs}(T)dT - \int_{T_0}^{T} \alpha_{Film}(T)dT)}{\frac{W_{Gage}}{2} * \left[\int_0^{\frac{L}{2}} \frac{dx}{f(x)}\right]} \tag{31}$$

Where the term σ_{Fr} is the fracture strength of the material and σ_{res} is the initial residual stress present in the film at room temperature.

5.2 Results

The fracture strength of the thin film can be calculated using (31) by knowing its physical parameters and the temperature at which it breaks. In Figures 43 to 48, the results from the analytical model for each shape are shown. These results indicate a rising trend in the fracture strength of the material, just as it was observed for the FEA results. It also supports the conclusion of the shape being negligible, due to every shape following the same pattern.

In the results for shape #1, in Figure 46, it is possible to see a semi-constant fracture strength

up until temperatures of 450 °C, and then the fracture strength starts to grow exponentially. The growth is slow, taking almost 150 °C of increase to change from 1 GPa to 2 GPA; however, as temperatures increase, the 1 GPa increase happens within 100 °C of change. The values of stress go from 0.704 GPa up to 6.48 GPa. The known trend of decreasing fracture strength as temperature increases is not observed for the results of the analytical model, just as they were not observed for the FEA results.

In Figure 47, the change of the fracture with respect to the length of the device is observed. As it was expected, the longer the device is, the lower its fracture strength is; however, it is possible to observe a considerable amount of scattering for this device. As for the simulated fracture strength, the plot where the change of fracture strength depends on temperature is smoother and not as scattered, and this could confirm that just as in the simulation results, the shape and the length play a secondary role to the temperature.

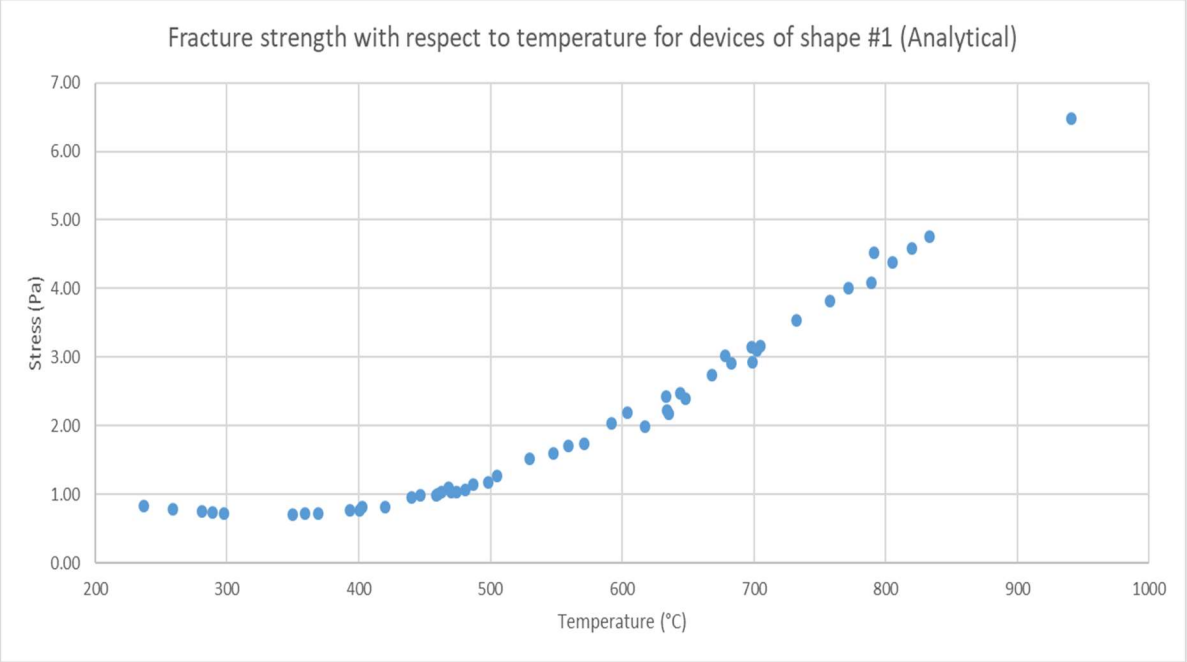

Figure 46. – Variation of the analytical fracture strength of a silicon nitride thin film of shape #1 with respect to temperature.

In the results for shape #2, in Figure 48, a similar pattern is observed with a constant value up to 450 °C, when the strength increases exponentially just like shape #1. However, in the case of this shape, when the temperature increases beyond 600 °C, the growth becomes 2 GPa per 100 °C change. It is interesting to mention that in neither of shape #1 and shape #2 there is much data for temperatures higher than 800 °C, this can be due to the devices with dimensions designed to break in these temperatures to not have been appropriately released during fabrication. The data points with temperatures beyond 800 °C found in these plots can be explained as devices that had no critical flaws despite their lengths.

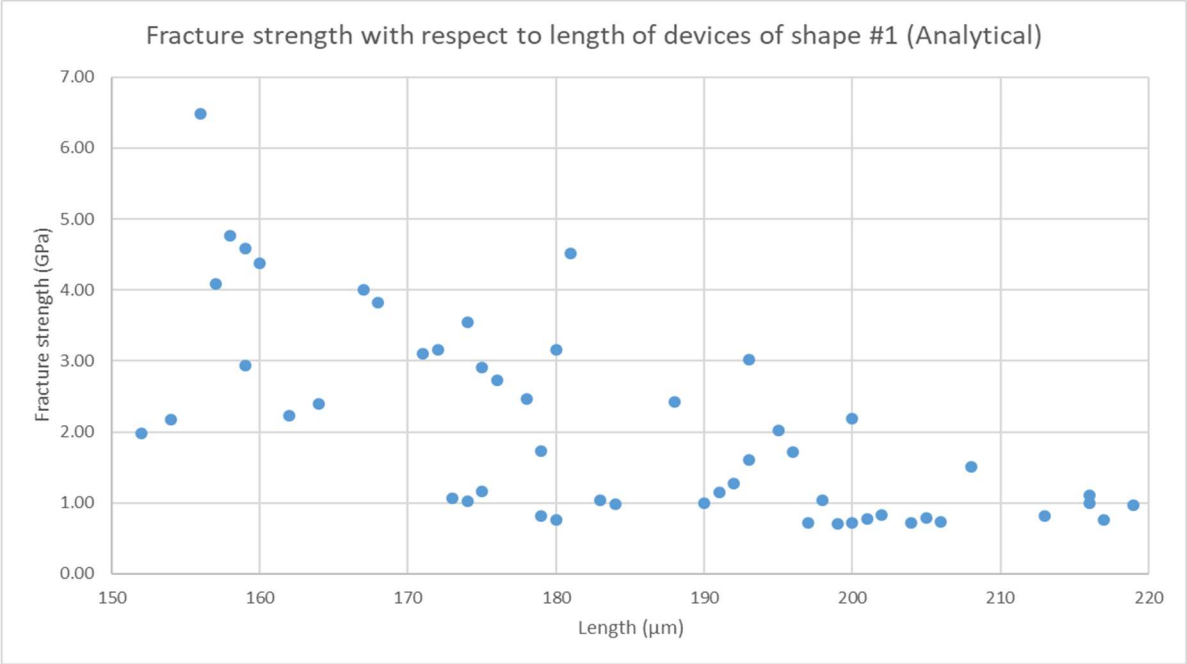

Figure 47. – Variation of the analytical fracture strength of a silicon nitride thin film of shape #1 with respect to length.

In Figure 49, it is possible to observe the change of the fracture with respect to the length of the device. The trend is maintained where the smaller devices break at higher temperatures than the longer devices. However, there is a significant amount of scattering compared to shape

#1, which could mean that this shape is not as stable as shape #1. The temperature plot keeps being smoother than the shape plot not as scattered; however, the change in the magnitude of the fracture strength could be attributed to the transition from evenly shaped devices, like those of shape #1, to unevenly shaped devices, like those of shape #2.

In the results of shape #3, shown in Figure 50, the exponential increase of the fracture strength is evident just above 400 °C. This shape, just like shape #1, has changes of 1 GPa per 100 °C. Opposite to the other two shapes, in this shape, there is a considerable amount of data at temperatures higher than 800 °C, which is consistent with the dimensions of the tested devices due to devices of shape #3 smaller than those of the other two shapes were tested; thus the higher fracture strength was expected.

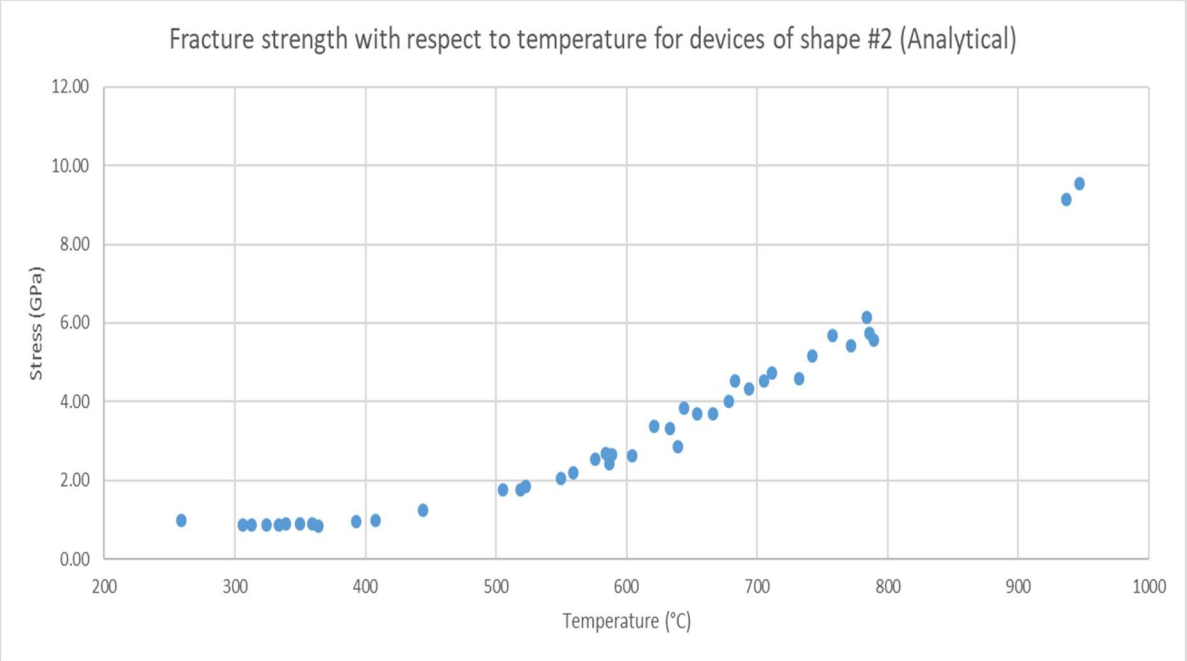

Figure 48. – Variation of the analytical fracture strength of a silicon nitride thin film of shape #2 with respect to temperature.

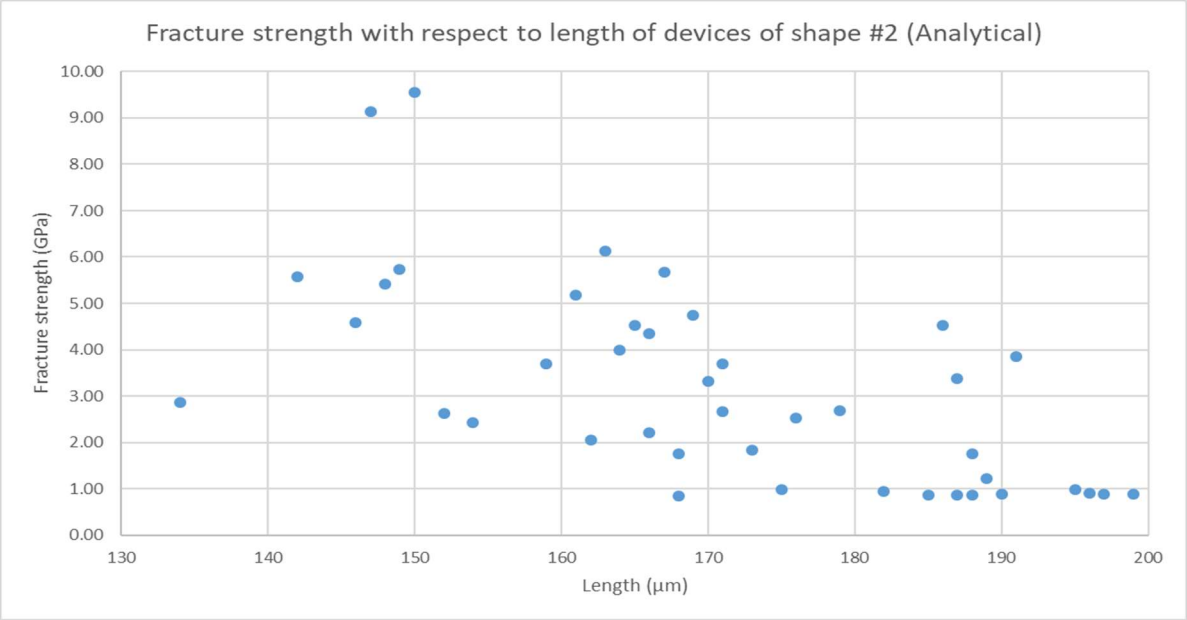

Figure 49. – Variation of the analytical fracture strength of a silicon nitride thin film of shape #2 with respect to length.

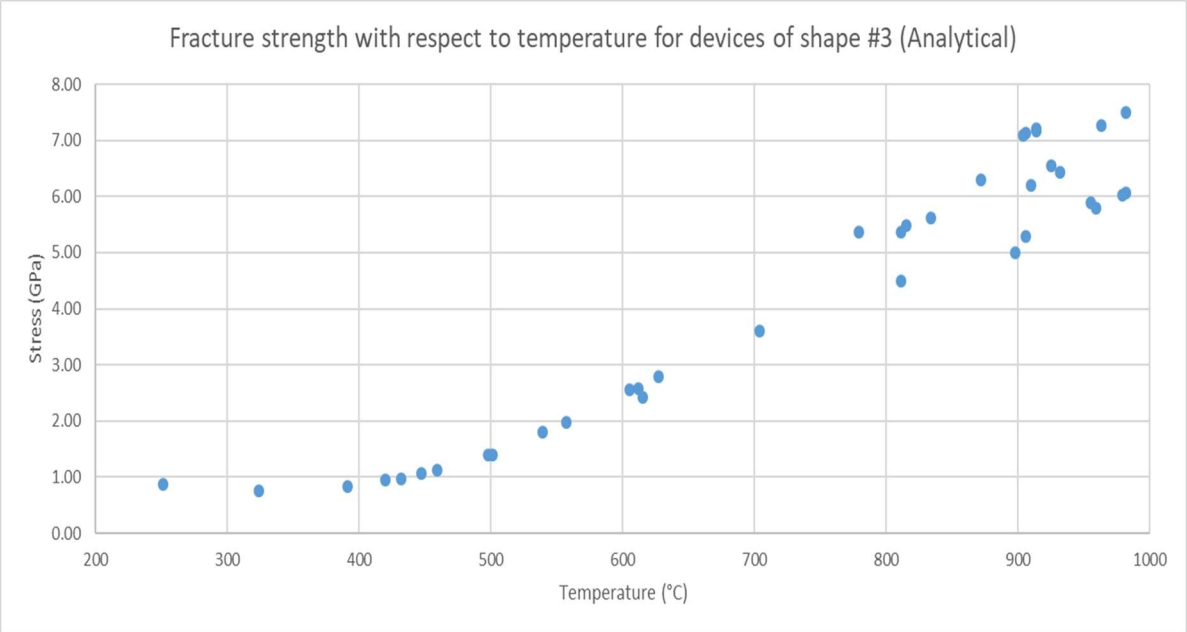

Figure 50. – Variation of the analytical fracture strength of a silicon nitride thin film of shape #3 with respect to temperature.

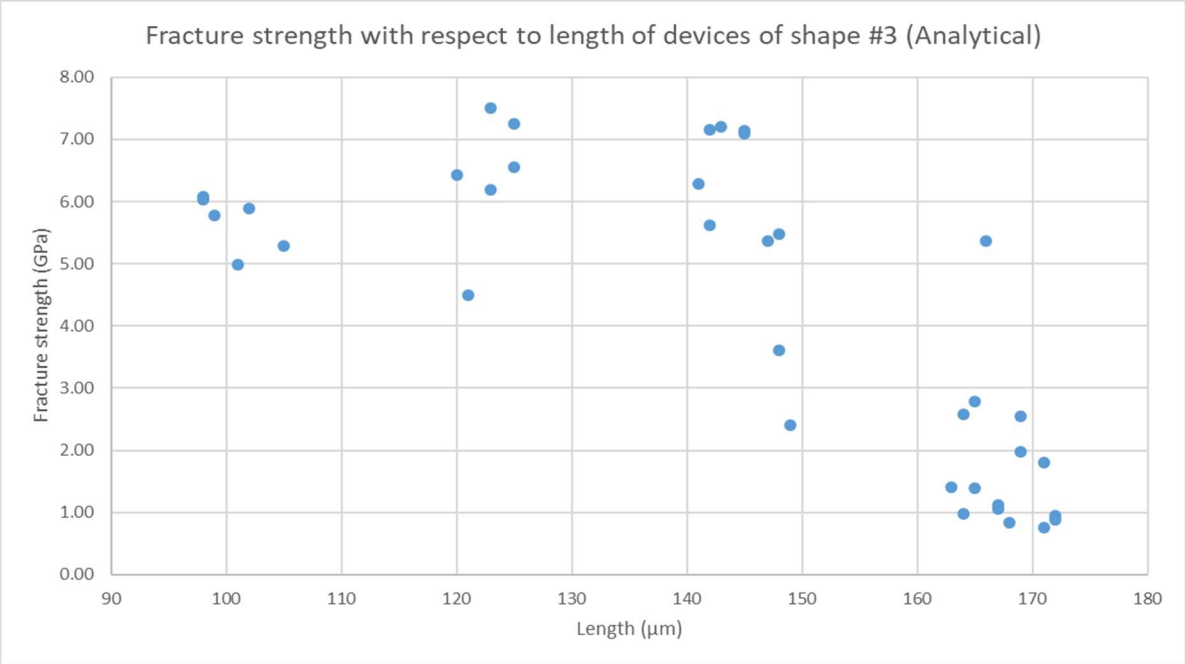

Figure 51. – Variation of the analytical fracture strength of a silicon nitride thin film of shape #3 with respect to length.

Every shape shares the same trend, and the values of fracture strength are not too different from the other; thus, they can be plotted in the same curve to observe the whole data. In Figure 52 and Figure 53, the full curve of the fracture strength for every shape and their corresponding trend lines are plotted, respectively. In this plot, it is possible to find how every shape behaves very similarly at temperatures up to 500 °C; it is then that the devices of shape #2 have a faster rise in their strength values. For the few data points at temperatures above 800 °C, it is possible to observe the trend still is preserved by shape #1 and shape #3, while shape #2, as mentioned before, rises faster. In Figure 54 and Figure 55, the analytical fracture strength with respect to the change of length and its respective trend lines is plotted, respectively. This plot confirms how unpredictable is the effect of the length in the results due to how the smallest devices are not the ones with the highest strength. At the same time, devices of shape #2 have the same fracture strength as those of shape #3 while they double them in size.

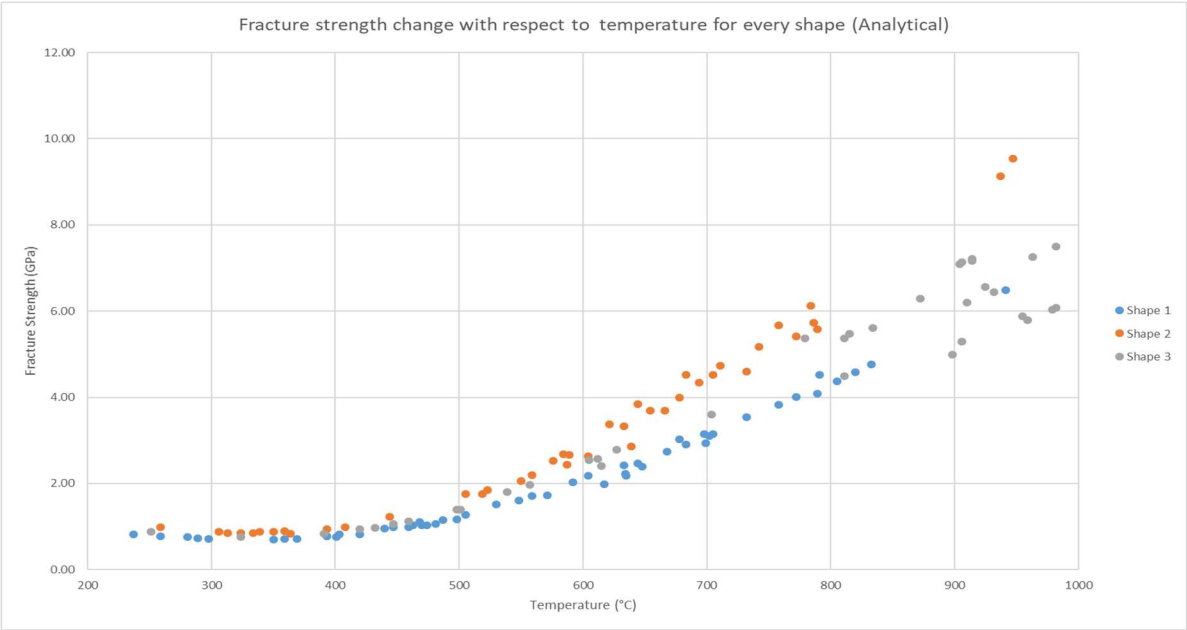

Figure 52. – Calculated fracture strength of all the tested devices. The three curves have an agreeing trend on the behavior of their strength at high temperatures.

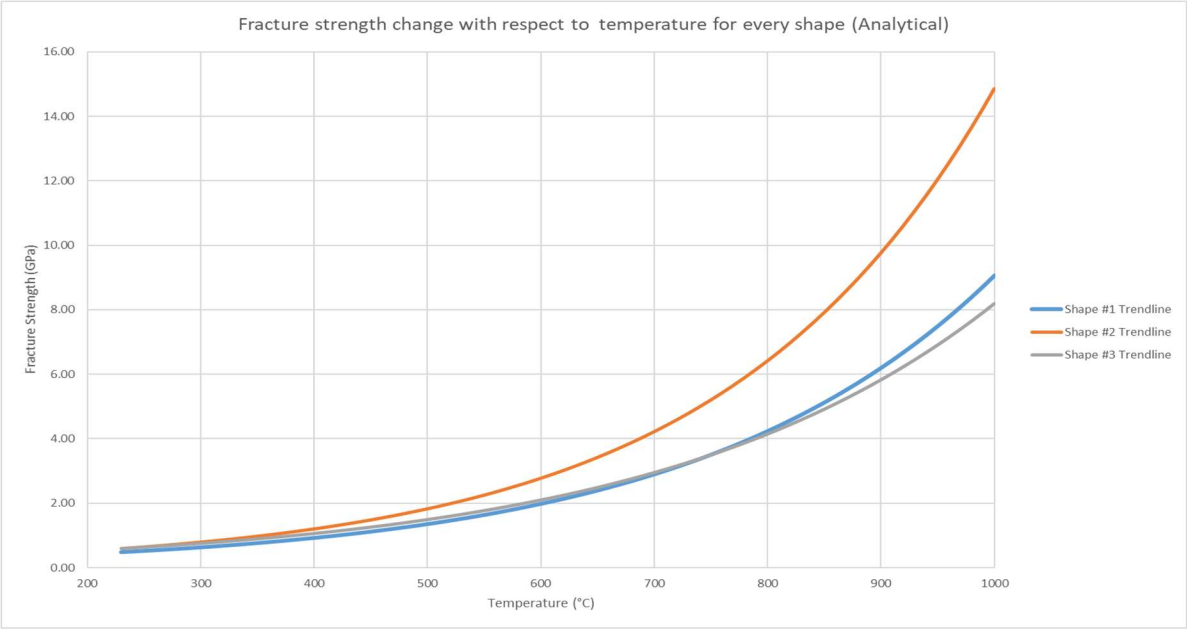

Figure 53. - Trend lines corresponding to the fracture strength change with respect to the simulated temperature for the tested devices.

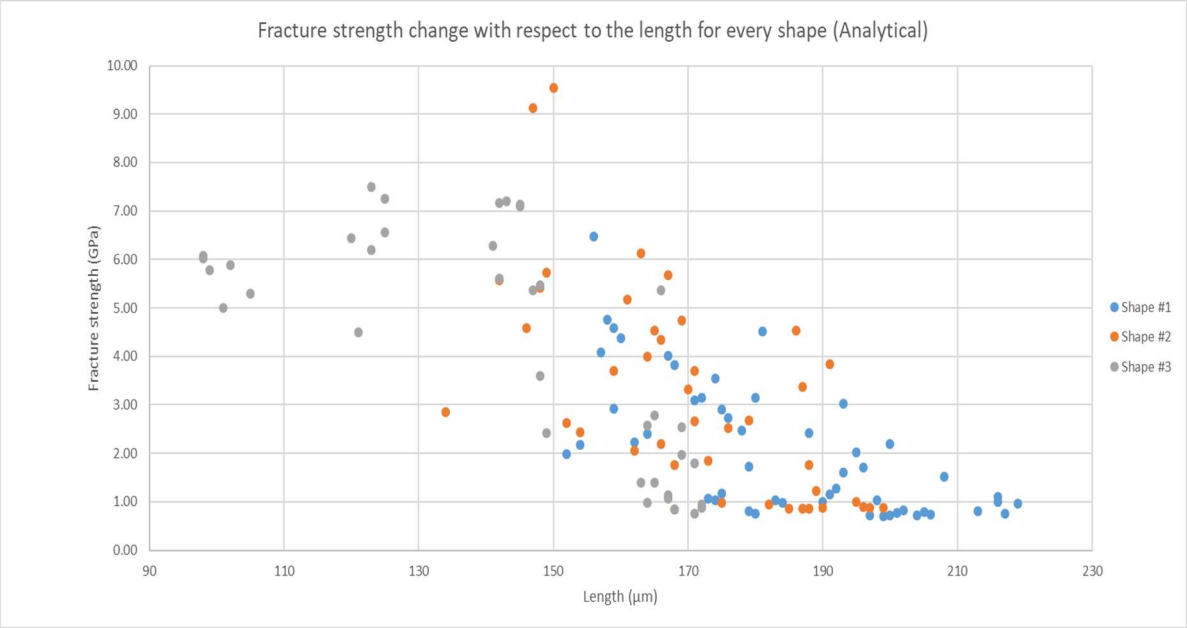

Figure 54. – Change of the simulated fracture strength with respect to the length of the devices for every shape.

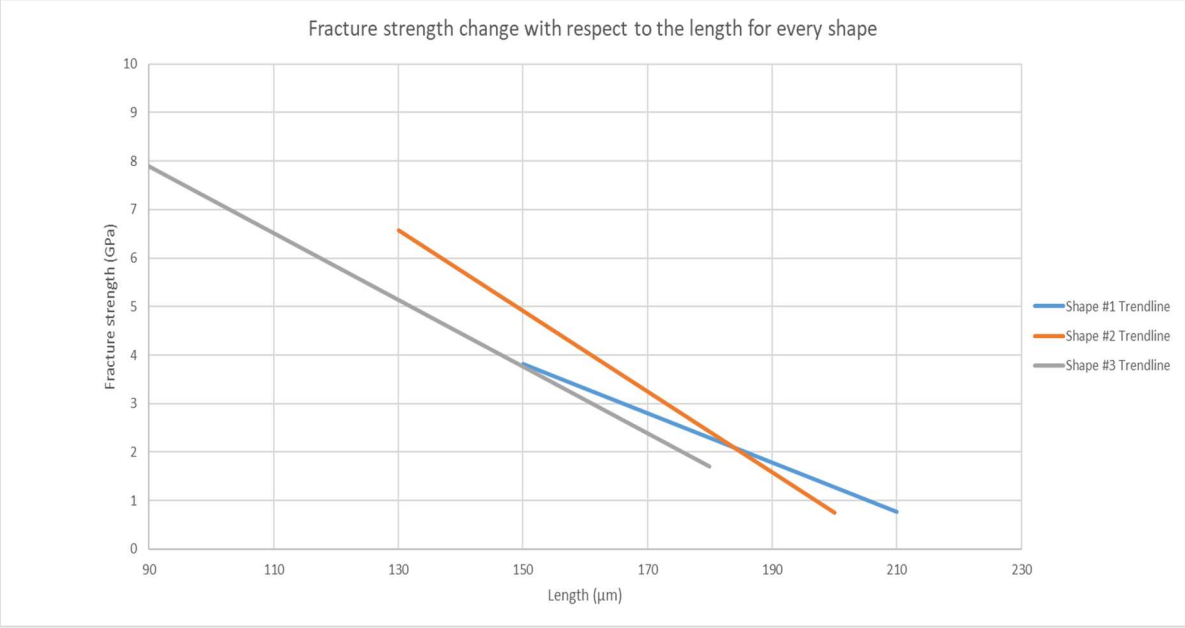

Figure 55. - Trend lines corresponding to the fracture strength change with respect to length simulated for the tested devices.

Just like the results obtained for the simulations, the results from the analytical model need to be analyzed using statistical approaches. Thus, to be able to use this data as a guideline for MEMS design involving Si_xN_y, the results need to be quantified by using a Weibull approach.

5.3 Weibull analysis

The data for every shape is processed using the Weibull distribution. In Figure 56, using the calculated fracture strength in equation (31), a Weibull plot for the fracture strength of shape #1 is built. From the linear regression, the parameter *m* is determined from the plot's slope, obtaining a value of 1.71, which is used to determine the σ0 parameter determining a value of 2.32 GPa. The plot in Figure 56 is also representative of the degree at which the Weibull distribution can represent the studied data set. The data points are distributed along with the linear fit, proving that the Weibull distribution and its linear regression can adequately relate the fracture strength data to the breaking temperature data.

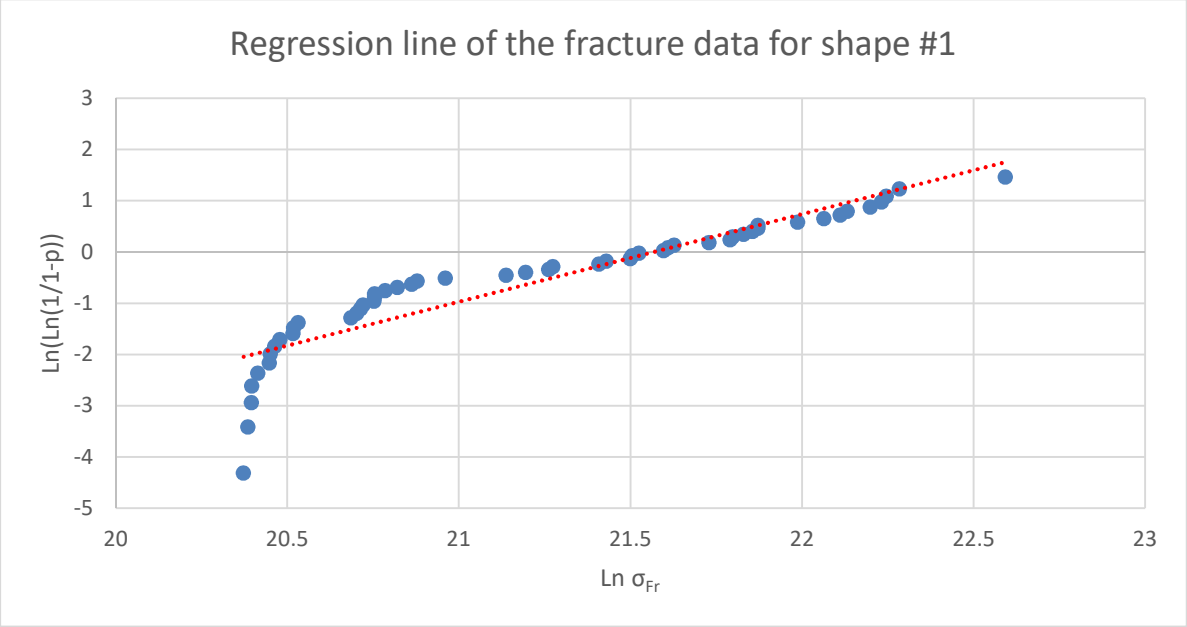

Figure 56. – The scattered fracture strength data of the devices of shape #1 represented in a Weibull plot. A linear regression fit demonstrates the adequacy of the use of the distribution.

In Figure 57, the survival rate plot is presented, in which it can be determined that there is an 88% probability of survival for the structure when operating to stresses below 0.7 GPa at temperatures underneath 1000 °C. Thus, when a device is fabricated using Si_xN_y for applications where temperatures of 1000 °C are present, it is predicted that stress of 0.7 GPa or less will not affect the device performance. The device can be defined as being reliable under these conditions.

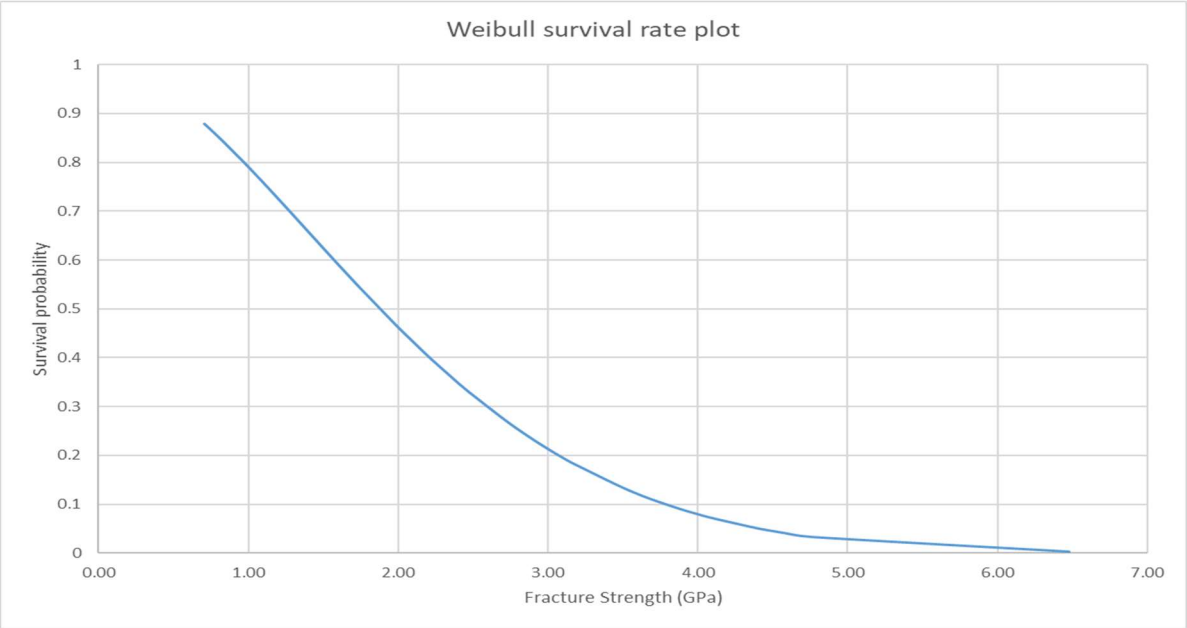

Figure 57. – Survivability plot of the determined values of fracture strength of thin films of shape #1. The devices will have around an 88% probability of being reliable when submitted to stresses of 0.7 GPa at temperatures up to 1000 °C.

The parameter *m* is determined from the linear regression plot slope in Figure 58 for devices of shape #2. The values for *m* and σ0 are 1.53 and 3.57 GPa, respectively. Similarly, as it happened for shape #1, the data points distributed along with the linear fit, proving that the Weibull distribution to be the right fit to model this data. The value from m shows as well that there is a similar dispersion as shape #1. Using the Weibull parameters of dispersion and

characteristic life in equation (2), the survival rate of the material is calculated. In Figure 59, the survival rate plot is presented where the probability of a device to resist an indicated amount of stress is visualized. In this distribution, it can be determined that there is a 90% probability of survival for the structure when operating to stresses below 0.84 GPa at temperatures underneath 1000 °C. Thus, when a device is fabricated using Si_xN_y for applications where temperatures of 1000 °C are present, it is predicted that the stress of 0.84 GPa or less will not affect the device performance. The device can be defined as being reliable under these conditions.

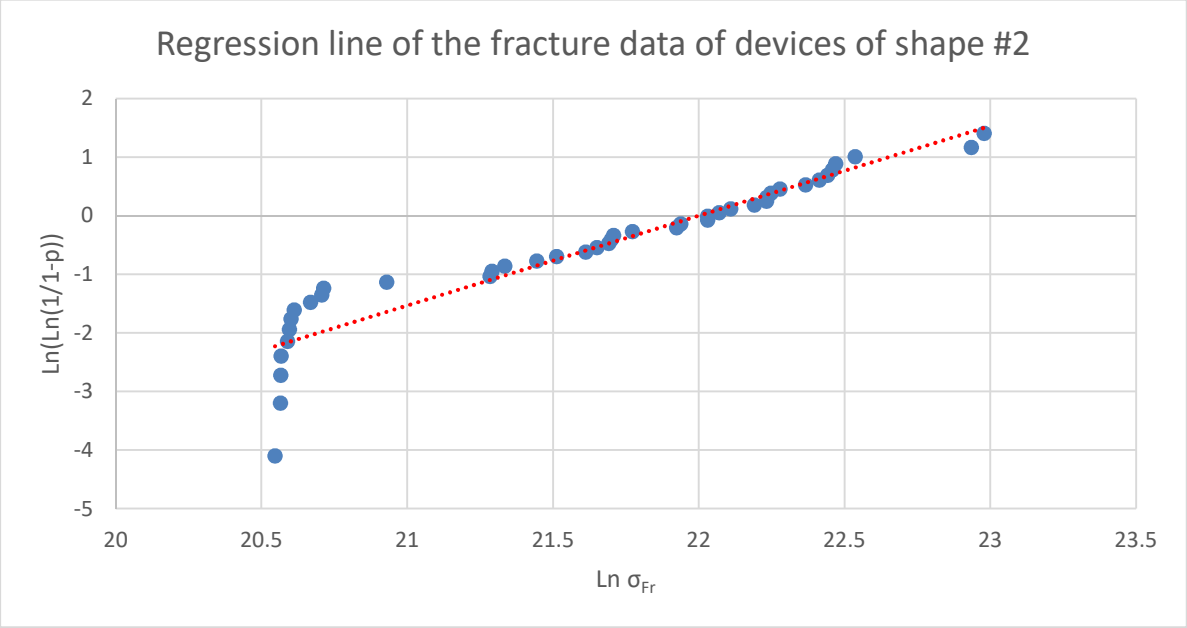

Figure 58. – The scattered fracture strength data of the devices of shape #2 represented in a Weibull plot. A linear regression fit demonstrates the adequacy of the use of the distribution.

The parameter m is determined from the linear regression plot slope in Figure 60 for devices of shape #3. The values for m and σ0 are 1.46 and 4.86 GPa, respectively. Similarly, as it happened for the other two shapes, the data points distributed along with the linear fit with some more concentration at the ends of the fitting line. The value from m shows as well that

there is a smaller dispersion of the data for this shape with respect to the other two. Using the Weibull parameters of dispersion and characteristic life in equation (2) allows for the calculation of the survival rate of the material when submitted at different stresses. In Figure 61, the survival rate plot is presented where the probability of a device to resist an indicated amount of stress is visualized. In this distribution, it can be determined that there is an 87.5% probability of survival for the structure when operating to stresses below 0.76 GPa at temperatures underneath 1000 °C. Thus, when a device is fabricated using SixNy for applications where temperatures of 1000 °C are present, it is predicted that the stress of 0.76 GPa or less will not affect the device performance.

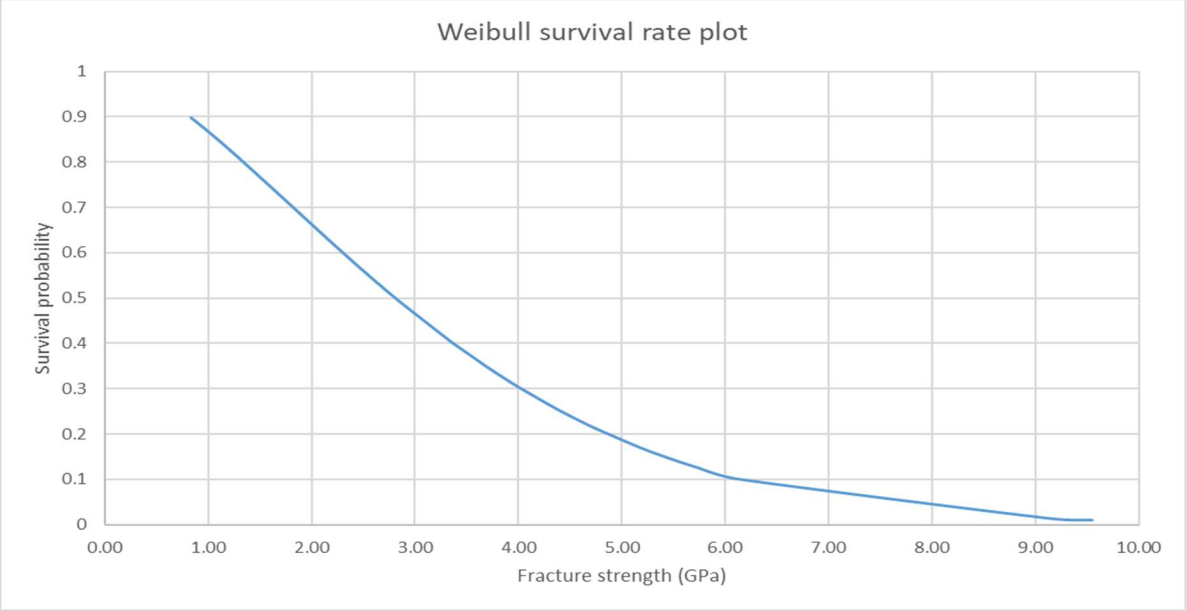

Figure 59. – Survivability plot of the determined values of fracture strength of thin films of shape #2. The devices will have around a 90% probability of being reliable when submitted to stresses of 0.84 GPa at temperatures up to 1000 °C.

In Table 7, a summary of the values obtained for the Weibull parameters for shape #1, as well as the median, mean, and standard deviation of the distribution, are presented. The spread parameter "m" is very similar for every shape; however, the characteristic life parameter keeps

increasing as the shape changes. This increase can be attributed to the displacement of the data due to the longest devices being those of shape #1 and the smallest those of shape #3, which will increase the fracture strength due to having more high-temperature data points.

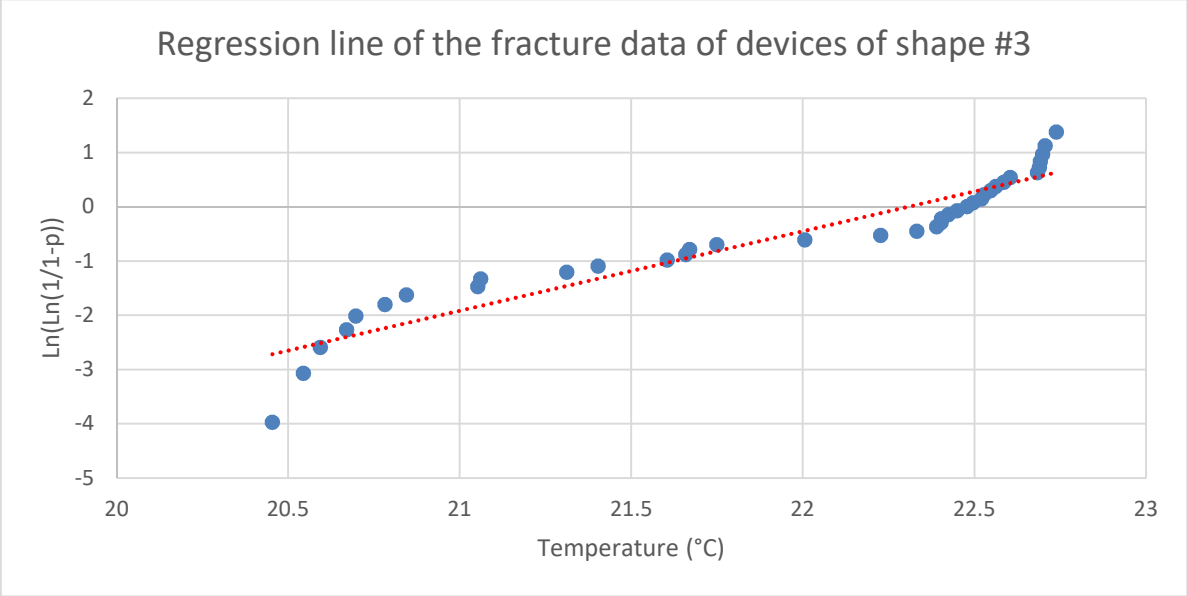

Figure 60. – The scattered fracture strength data of the devices of shape #3 represented in a Weibull plot. A linear regression fit demonstrates the adequacy of the use of the distribution.

Table 7. – Weibull parameters for the devices of every shape

Parameter	Shape #1	Shape #2	Shape #3
m	1.26	1.53	1.46
σ_0	1.34 GPa	3.57 GPa	4.86 GPa

The results for all the shapes are compared at a 20% probability of failure as it was done for the simulation results. It is found that the fracture strength shows a more noticeable variation for every shape. For devices of shape #1, the fracture strength is of 0.97 GPa, for devices of

shape #2 the fracture strength is 1.75 GPa and for devices of shape #3 the fracture strength is of 1.34 GPa. The values have a variation of only 0.78 GPa, which shows the influence the length of the device has for the analytical results.

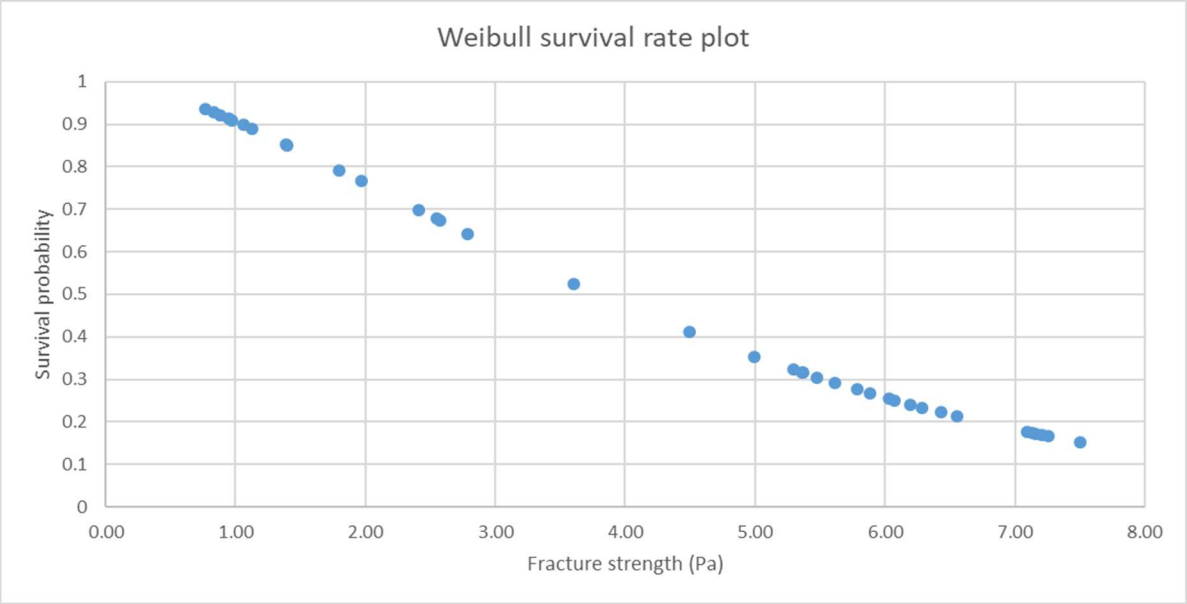

Figure 61. – Survivability plot of the determined values of fracture strength of thin films of shape #3. The devices will have around a 94% probability of being reliable when submitted to stresses of 0.76 GPa at temperatures up to 1000 °C

5.4 Comparison between the simulated and analytical results

The results for both approaches show agreement on the two obtained trends for the fracture strength data. The first trend is the increase of the fracture strength as the size of the devices is decreased, and the second trend is the increase of the fracture strength as temperature increases. However, the magnitudes of the fracture strength determined for both approaches differ significantly, where the values obtained for the analytical method are within the same order of magnitude but have an increase of over 200%. To analyze the reasons for this disparity, in Figures 62 and 63, the plots comparing the change between the analytical and simulated

fracture strength with respect to temperature and their trend lines, respectively. The same data pairings simulated are taken from the analytical values and plotted together. This comparison is made to validate the simulation results with the proposed analytical model, which will help to understand the modifications the current device requires to improve the methodology.

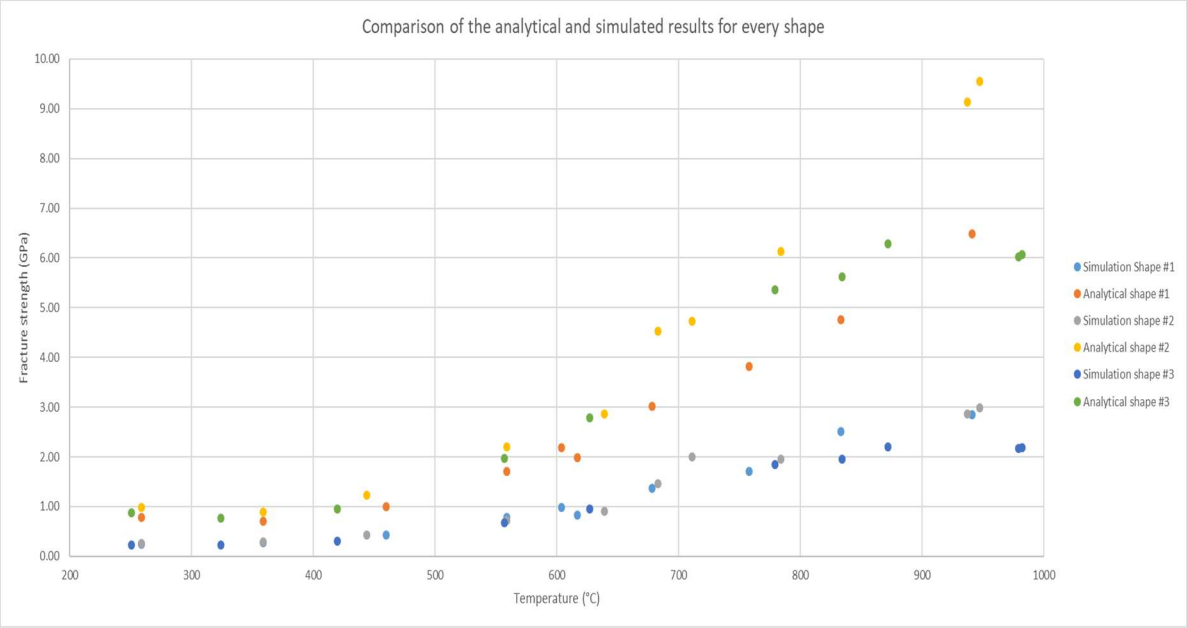

Figure 62. – Comparison between the calculated and simulated fracture strength of all the tested devices with respect to temperature.

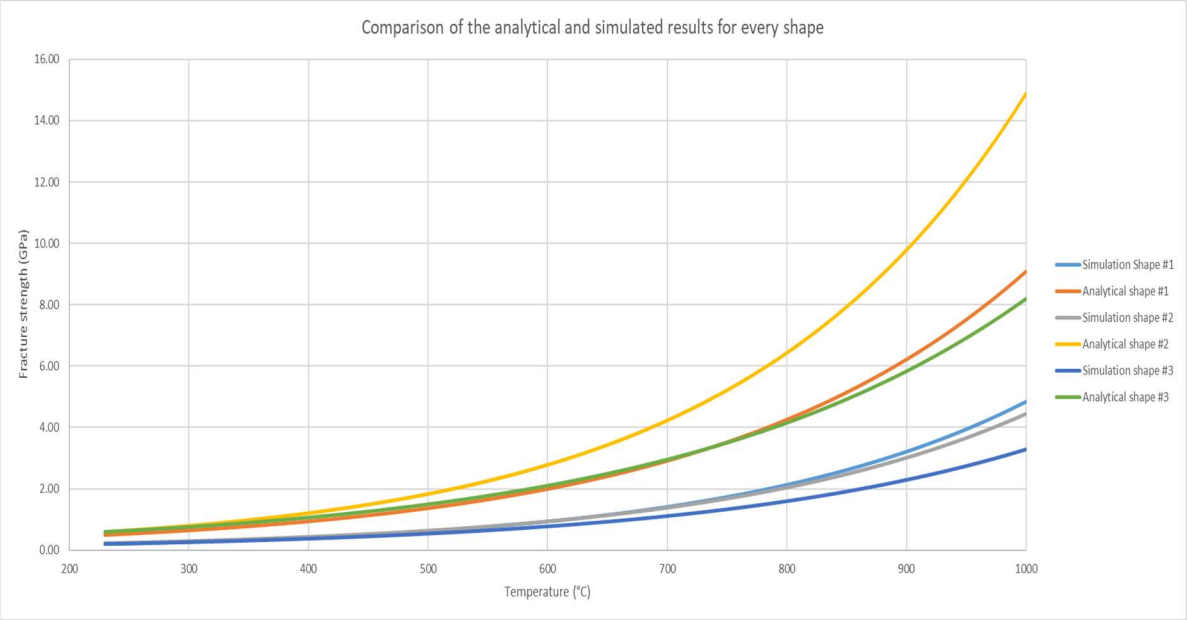

Figure 63. Trend lines corresponding to the comparison of fracture strength change with respect to the temperature for every shape by simulation and analysis.

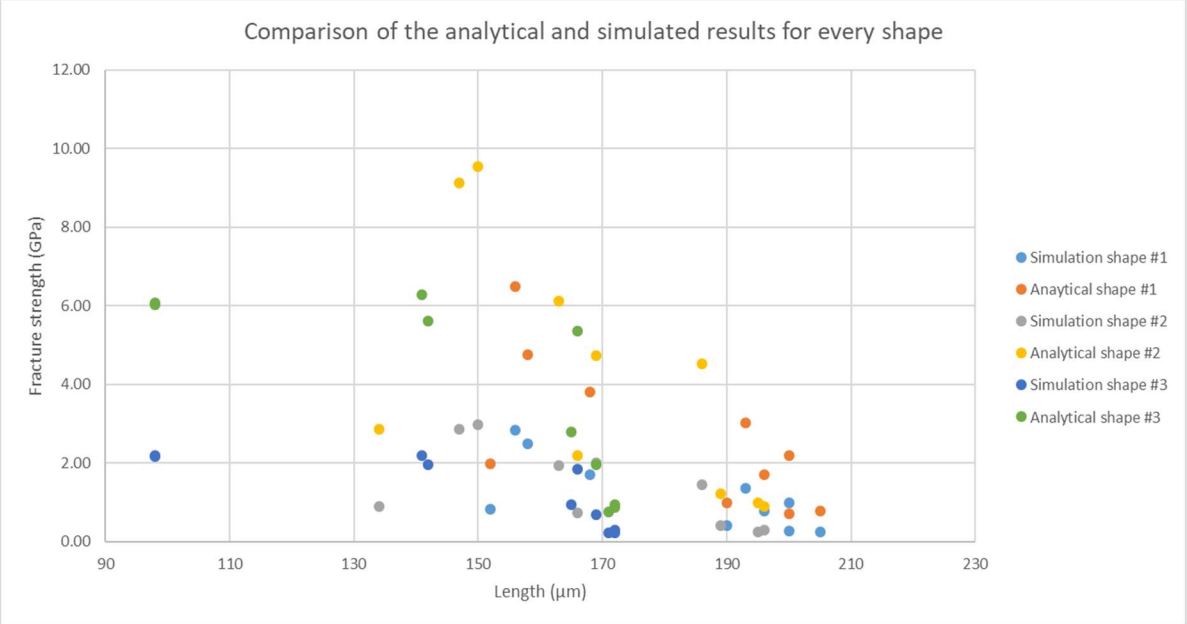

Figure 64. – Comparison between the calculated and simulated fracture strength of all the tested devices with respect to geometry.

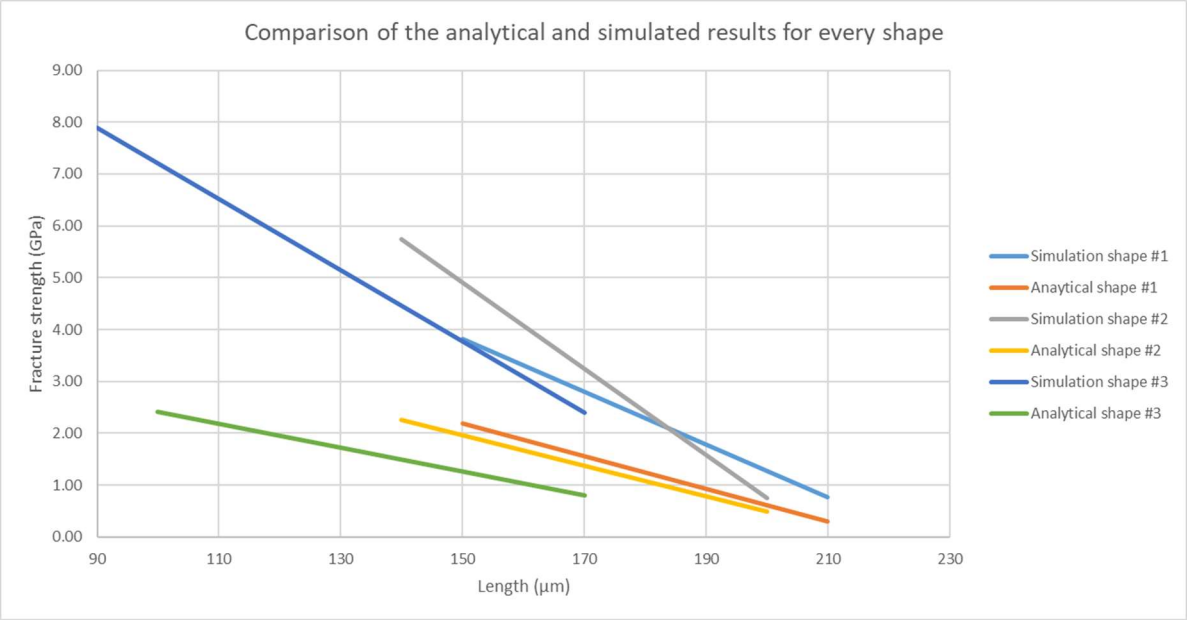

Figure 65. - Trend lines corresponding to the comparison of fracture strength change with respect to the length for every shape by simulation and analysis.

In the graph in Figure 62, the difference in magnitude between both approaches is observed, which shows the values for the simulation are higher than those obtained for the analytical. It is also noticeable that the curves corresponding to each shape follow one another more closely in the simulation results than in the analytical method. There are different reasons for this difference between both results to happen. One of these reasons is the approach taken for the analytical model, which is that of uniaxial stress, not matching the approach taken for the simulation, which has different stress fields in every direction affecting the device. The various stress fields can introduce compressive stresses that change the magnitude of the stress at the gage section of the device, and those are not accounted for in the analytical model. This is observed when plotting the thermal profile of one of the devices. During the first 300 seconds, a temperature decrease is applied to the structure to simulate the 0.39 GPa of residual stress due to fabrication. When the temperature starts to increase the stress drops ~0.2 GPa and it does not reach the value of 0.39 GPa until the device heats up to 430 °C, while for the analytical

results at a temperature of 330 °C the stress has already passed the 0.39 GPa stress value.

Another reason for the difference in magnitudes can be determined from the graph in Figure 64, where the data points for the simulation results are close to the bottom of the chart. In the longer lengths of the data sets, the difference is of about 0.7 GPa. Meanwhile, as the length reduces, the difference in magnitude increases up to 7 GPa, which allows for the conclusion that the current analytical model is developed highly dependent on the geometry change, in particular of the length. Using the analytical model, the data is evaluated for different thicknesses ranging from 0.175 μm up to 3 μm, showing no significant change in the results, thus the length and symmetry change of the devices are the main contributors to this shape dependence. This assumption is also supported by the results obtained, where shape #2, which is asymmetrical, has a higher rate of change in the fracture stress in comparison to the other two shapes which both are symmetrical.

Lastly, as mentioned in the previous chapter, the thermal strain, shown in Figure 44, is modeled to follow the CTE mismatch in both approaches. The thermal strain trend follows the fracture strength curve for the results in both methods. However, this thermal strain will change as the Si substrate undergoes brittle to ductile transition as the temperature increases, which will affect the interaction between the substrate and the thin film. This is a shortcoming of this methodology, which needs to be resolved for future iterations of the device. A strain measurement that takes place during the experiment would allow for a comparison between the calculated and actual strain. This will allow the modeling of the actual thermal strain progression. In the following chapter, the next iteration of devices and new test methodologies required to test them are described and presented.

Chapter 6
Improvement of the methodology to study fracture strength at high temperatures

In previous chapters, the current methods and devices were presented with their obtained results. The most critical shortcoming of the current methodology is the difficulty of determining the strain evolution of the CTE mismatch as the temperature increases. Thus, a method to measure the strain of the thin films is required throughout the experiment. An in-situ strain monitoring approach is needed to keep the objective of the methodology not to have too many elements to the test setup. From the reviewed works in Chapter 2, there is one that stands outdone by Sharpe et al., where a non-invasive in-situ optical methodology is used [15]. The name of this technique is known as interferometric strain/displacement gage (ISDG).

6.1 Interferometric strain/displacement gage

ISDG is a technique where two reflective markers are deposited or indented onto a material, and a laser is shot at these markers to generate a set of refractive fringes that interfere with each other [63] The interference fringes are measured using camera or diode arrangements, and the information is processed using image processing codes to measure the displacement of the fringe. An advantage of this technique is the possibility to measure the strain directly from the test devices [64]. When a laser is shined onto the surface where the markers are placed, interference of the diffracted beams can be measured [65]. The optical principle is based on Young's two-slit interference phenomenon except that in this case, the light is reflected and does not go through a slit. This phenomenon splits into two components, the first one is the diffraction of the laser beam fringes, and the second one is when these fringes interfere one with the other. When light passes through an aperture and spreads, its behavior follows the expression given in (32) :

$$I = I_0 sin^2 \beta_0 / \beta_0^2 \quad (32)$$

Where β is given in (33):

$$\beta_0 = {\pi b sin\theta}/{\lambda} \tag{33}$$

Where λ is the wavelength of the wave, and b is the width of the slit/marker. The beam is aligned using a reference of intensity, I_0, and the intensity that characterizes the exiting beam is given by I and varies with the angle θ that is the angle between a parallel reference line to the light beam and the position to the target where the light is projected [63]. The intensity minimum is reached when β_0 is equal to $\pm\pi$; thus, the width of the pattern is given in (34):

$$sin\theta = \lambda/b \tag{34}$$

When monochromatic light is reflected on the markers, the diffracted beams overlap with each other creating an interference pattern, and the spacing between the fringes in the pattern is determined by (35):

$$I = I_0 cos^2\gamma_0 \tag{35}$$

Where γ is given in (36):

$$\gamma_0 = \pi d sin\theta/\lambda \tag{36}$$

In which, d is the spacing between the two slits/markers. The value of γ_0 is at its minimum when it equals π/2, 3π/2, 5π/2, etc.; thus, the spacing between the interference fringes will be given by (37):

$$sin\theta = \lambda/d \tag{37}$$

Where d is the distance between the reflective markers. Knowing this information, what is needed to be measured is the phase shift of the fringes to be able to calculate the strain through the displacement of the markers. In (38), the strain is calculated from the data obtained through the ISDG methodology:

$$\varepsilon = \frac{(\frac{\Delta \emptyset}{2\pi})\lambda}{d_0 * sin\theta} \quad (38)$$

Where $\Delta\varphi$ is the phase shift of the fringes, and d_0 is the initial distance between the reflective markers. This methodology has been used for years in the testing of materials and has been applied to microstructures. From the studied methods to measure strain in ceramics, this one seems to be one of the best approaches for being straightforward, non-contact and proven accurate through different studies [47], [64]. For this reason, this technique will be implemented onto the structures to be used in this work. The new devices and their fabrication processes are introduced in the following section.

6.2 Device redesign for the in-situ monitoring of strain

The objective of the new devices is to be adaptable to the ISDG methodology; however, the smallest dimensions reported for markers are those made with indentations, while metallic markers require larger dimensions in the sample to be placed. Due to the thickness of the thin films proposed here, an indentation is not feasible to be the marker for the devices. Thus, reflective material has to be deposited on top of the thin film. From the research done by Sharpe et al., it is concluded that one of the best options for markers is metallic materials, and platinum (Pt) is a metal that can withstand very high temperatures without deforming.

A study of the optical interaction between the materials to corroborate the compatibility of the ISDG approach with the structure used in this research was done. It is important to determine if the used materials will be an impediment to obtain a meaningful reflected signal for the measurement reading. The first calculations determine the amount of reflection that will be obtained from the device when the signal is sent. The schematic to show the optical interactions of the device is shown in Figure 66. The light source arrives with a 0° degree angle on top of the structure; the intensity of the source will reflect from the top of the surface of the

device. To calculate this reflection and determine the dominant signal (39) is used [65]:

$$R = \frac{(n_{mat} - 1)^2 + k^2}{(n_{mat} + 1)^2 + k^2} \tag{39}$$

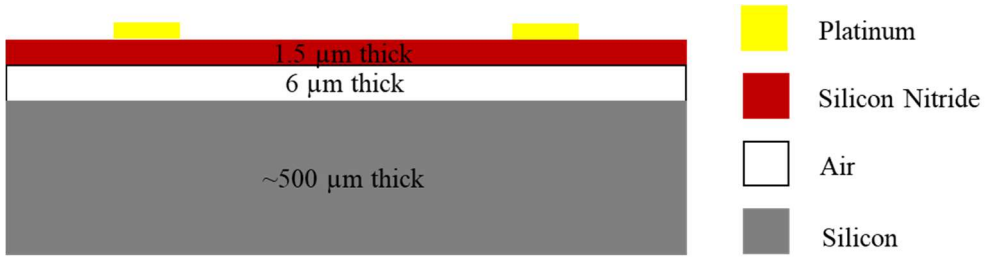

Figure 66. – Schematic of the fabricated device with the addition of metallic markers on its surface for strain monitoring

Where n_{mat} is the refraction index of the material, and k is the extinction coefficient. The light source will contact the platinum markers and the silicon nitride surface and reflect a percentage of the signal and transmit the remaining signal through the material at a 0° degree angle. In that case, the transmitted signal will go through the different layers that are part of the device, and a percentage of the transmitted signal will reflect and be transmitted through the material layers back to the surface of the thin film. This cycle can be observed in Figure 67:

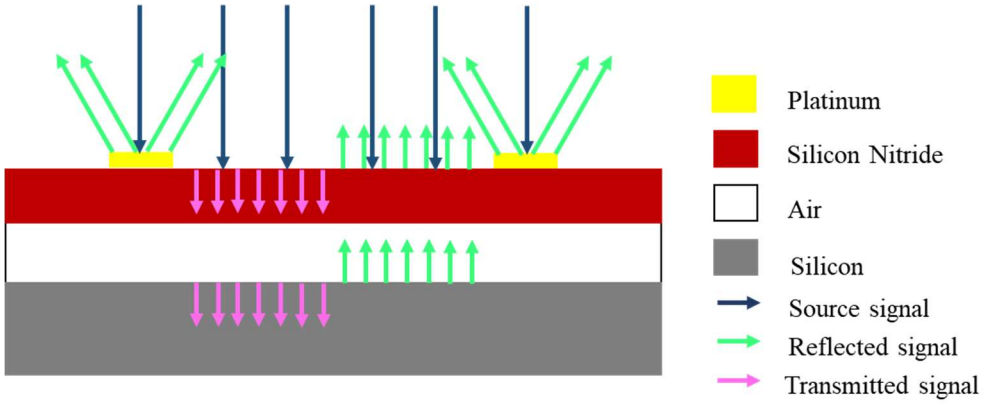

Figure 67. – Optical interactions between the layers that integrate the device.

The reflectivity of each material is calculated using (35), and the results condensed in Table 8.

Table 8. – Optic reflectivity of each layer as the light source is shined on the device metallic markers

Material	Refraction index	Extinction coefficient	Reflectivity
Platinum	0.46704	6.131	0.953 (95.3%)
Silicon Nitride	2.0394	0	0.1169 (11.7%)
Silicon	3.8823	0.019589	0.3485 (34.85%)

The results show that at the beginning of the interaction, the dominant signal is that of the Platinum markers, with 95% of the original intensity being reflected away from the surface of the thin film towards the sensing area of the experiment. An intensity of 2942.32 mW/m^2 is used to visualize these results, which is the intensity of the available laser at the SIMS Lab. When the signal initially makes contact with the platinum markers, they reflect 95.3% of the signal, which corresponds to a value of 2804.03 mW/m^2. The rest of the signal, approximately 5%, is transmitted, which can be neglected due to its small size compared to the other signals. However, when the light source with its initial intensity reaches the silicon nitride not covered by the markers, only 11.7% of the signal will reflect, which corresponds to an intensity of 343.95 mW/m2. The transmitted light which is 88.3% or 2598.36 $mW/m^{2,}$ will travel through the air phase until it reaches the silicon substrate. The transmitted light will again be reflected and transmitted; however, the transmitted and reflected signals that take place from interacting with an air layer are minimal; therefore, it is treated as negligible. Upon reaching the silicon layer, the reflected signal will be 34.85% from the intensity received at the layer, which is 905.5284 mW/m^2. The reflected light will travel back through the air layer and to the silicon nitride boundary and again be reflected by 11.7%, however, the transmitted intensity from that light interaction will be transmitted towards the sensing area and contribute to the intensity collected by the sensors. The transmitted signal is 799.674 mW/m^2, this value is added to the

previous 11.7% reflected from the original signal giving a total of 1143.62 mW/m^2, which represents 39% of the original signal. However, this quantity is way less significant than the signal emitted by the markers, which will not interfere with the fringe pattern from the markers due to the 95.3% signal be picked up over residual reflections from other layers. Therefore, the materials involved in the device are compatible to implement an ISDG approach.

Another critical parameter that affects the design of the new devices is the type of interference this 39% of the back signal would cause. The method to determine it is based on Snell's law expression, which derives (40):

$$2t_{film} * n_{film} * \cos(\theta_{incidentbeam}) = m_0 * \lambda \tag{40}$$

Where t_{film} is the thickness of the film, n_{film} is the refractive index of the film, ϑ is the angle of the light, λ is the wavelength, and m_0 is an integral number. This equation allows determining which thickness for the thin film material will cause the interference of the media to be constructive or destructive. The equation above (40) is for destructive interference, while for constructive interference, the expression is given by (41):

$$2t_{film} * n_{film} * \cos(\theta_{incidentbeam}) = \left(m_0 - \frac{1}{2}\right) * \lambda \tag{41}$$

In this new iteration of devices, a thickness higher than 0.175µm has to be used; otherwise, the structure could collapse when the markers are deposited. Based on the literature, the standard thickness of the markers is 0.5 µm. Therefore, a thickness of 1.5 µm will be proposed for the new devices to guarantee the structure to support the markers, which is also used to determine the value for m. The obtained value of m_0 is 9.66, which is rounded to the closest integer. The value is used to determine the thickness of the film to get destructive or constructive interference. For destructive interference, which is the preferred type due to noise signal canceling itself, a thickness of 1.55 µm is determined. For constructive interference and the case to avoid, the thickness was determined to be 1.47 µm. Thus, a thickness of 1.5 µm

will be used, although the variation of the film thickness due to fabrication tolerances has to be kept to a minimum.

The dimensions for the platinum markers and their separation affect the resolution of the experiment as well as the angles at which the fringes will be visible for the optical sensing equipment. Thus, the critical dimensions for the markers are their width and the separation distance between them. In Figure 68, a schematic with the dimensions of the markers is shown. The schematic is labeled to match the dimensions necessary to solve (34) and (37).

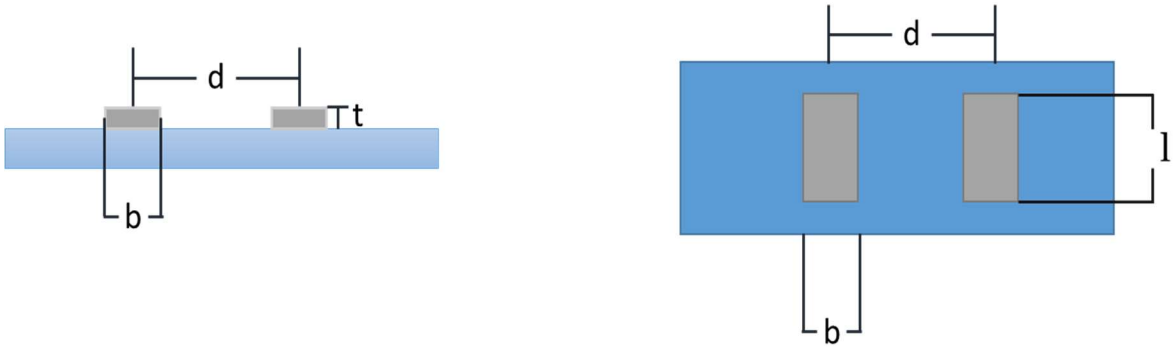

Figure 68. – Schematic of a frontal and a top view of the reflective markers and their dimensions.

The dimensions chosen for the width and separation of the markers are based on the research done by Sharpe et al, which is 10 µm for the width and 100 µm for the distance between markers. These dimensions are chosen to keep the dimensions of the overall device as small as possible. However, a variation in these dimensions will be introduced in the chip to obtain the best resolution from the experimental setup. The width of the markers will have values of 10µm and 40 µm, and the separation of the markers varies from 80 µm up to 133 µm. Less spacing between the markers distance. Using the following equation, the change of percentage in the resolution of the fringes produced by the markers based on their separation is determined:

$$d = \frac{\lambda * D}{x} \tag{42}$$

Using a D of 80000 µm which is an adjustable horizontal distance between the marker and the sensors, a λ of .633 µm and x is set to be calculated based on a percentage change. The scale is extended on both ends, decreasing the resolution in the event the test setup is not able to resolve the standard distance of 100 µm or increasing it to obtain bridges with the smallest dimensions possible. The following table can be put together:

Table 9. – Marker distance to change the resolution from the fringes

Resolution Percentage change (%)	Marker separation distance (µm)
+5	95
+10	91
+15	87
+20	83
+25	80
-5	105
-10	111
-15	118
-20	125
-25	133

With the dimension of the markers defined, the next step is to determine their positioning on the device. In the literature, the markers are placed on the gage section of the tested devices;

however, in the devices presented here, this is impossible due to the tiny size of the gage. If the markers are tried to be placed on the gripper sections, the wide surface area of the section could cause unexpected displacement of the markers, which is not desired. Thus, a double gaged device is proposed, so the markers can be deposited onto the thin film.

Differently from the first devices, the dimensions of length and width of the gage section will depend strictly on the marker, which will reduce the variation of these dimensions considerably. The devices will be fabricated in the three shapes that were studied in this work as a corroboration of the geometry change effect obtained in this first study. A fourth shape will be added to the study, which reduces the dimensions of shape #3, which will attempt to take the devices to a more standard shape of a tensile sample and reduce its size further. In Figure 69, a device of shape #1 is shown with the corresponding dimensions, those that will be defined, and those that will vary depending on the markers. In Table 9, the variable dimensions for the second gage section of these new devices are defined.

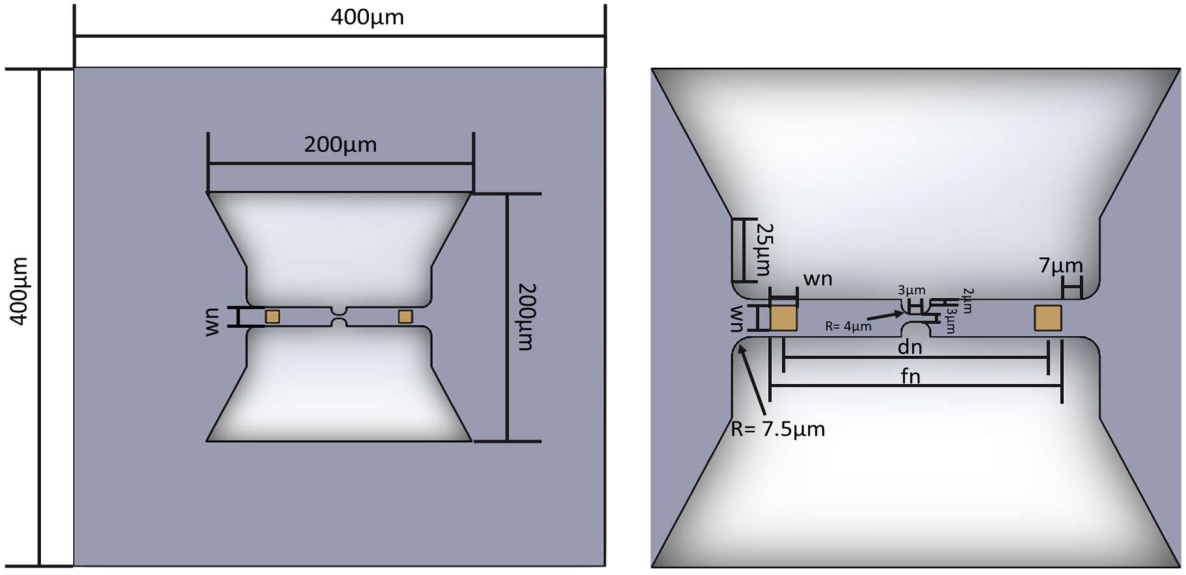

Figure 69. – Dimensions of a new device of shape #1. On the left, the full thin film with the frame that attaches it to the substrate is shown. On the right, the thin film bridge is shown. The variable dimensions that depend on the markers are shown.

The chosen width of the section where the markers are deposited is defined using the same fabrication rules as PolyMUMPS©. The distance from the edge of the marker to the edge of the gage section has to be a minimum 5 µm for the layers to be well defined during deposition. The distance between the furthest edges of the markers is given by the separation and the width of the markers. The remaining dimensions are set to match the first version of the devices while keeping the device area fixed to always be 200 µm square.

Table 10. – Variable dimensions from the second gage section of the new devices

Parameter	Meaning
d_n	Distance between the reflective markers from the center to center
f_n	Distance between the reflective markers from their furthest edge
w_n	Width of the second gage section

6.3 Mechanical properties dependent on temperature

During this work, mechanical properties like Young's modulus and CTE have been used in both the simulation and the analytical model. The change these two properties have with respect to the increase of the temperature has to be properly modeled for their inclusion in the post-analysis of the data. However, in the case of MEMS, these properties vary due to their fabrication process. Devices from the same material but fabricated in different fabrication runs can have their properties to change, and even within the same fabricated wafer, parameters like the residual stress will vary across the wafer [66]. Thus, it is in the best interest of the methodology to include several chips across the wafer with devices to measure these properties.

A very well-known approach will be used to measure Young's modulus of the thin film. Using cantilever beams and driving a vibration through them, a resonant frequency can be determined. The devices will be tested using a vibrometer and a piezo shaker. The piezo shaker

will excite the devices, and the laser of the vibrometer will be positioned on the tip of the beams. The beams vibration will be used to determine the beams resonance frequency and subsequently, Young's modulus of the material with the expression in (43):

$$E_{Si_xN_y} = \frac{38.34 * \rho * f^2 l^4}{t_{cantilever}^2} \tag{43}$$

Where ρ is the density, f is the resonant frequency, $t_{cantilever}$ the device thickness, and l is the length of the devices [67]. To calculate the appropriate length of the devices the frequencies at which the piezo shaker operates are used as the resonant frequency, which is from 20 kHz to 40 kHz. The Young's modulus at room temperature of silicon nitride is calculated using (15) and the lengths at which the testing will be successful range from 93 µm up to 133µm. However, just as with the fracture strength devices, the space in the chip allows for multiple devices to be placed in it. Thus, the dimensions of the beams are 40 µm of width, 1.5 µm of thickness and a length ranged from 73 µm up to 163 µm.

For the CTE devices, the approach used by Gang et al. will be adapted to this chip [68]. The CTE devices will be of two types, a single layer cantilever beam made of Si_3N_4 and a bimorph made of Si_3N_4 and Pt. The out of plane deflection of the single beam and the bimorph will be used to determine their CTE. The angular deflection of the beams is measured using an interferometric optical approach is used. The beams used in the designed chips are designed with the same length as those from Gang et al. study. The Si_3N_4 beams have a thickness of 1.5 µm, a width of 40 µm a length of 200 µm up to 400 µm in increments of 25 µm for both the single cantilever and the first layer of the bimorph devices. The second layer of the bimorph made of Pt has a 10 µm difference concerning the width and length of the Si_3N_4 beams and a thickness of 0.5 µm.

6.4 Device fabrication

MEMS fabrication is often a customized process to develop a single type of structure. In this

research, a fabrication process that will result in every structure proposed in this chapter is proposed. The process has been tested using software to simulate every step in the process. The results from the fabricated devices are shown in Figure 70, where the fracture strength thin films are shown. The following are the fabrication steps to achieve all these devices on the same wafer, a process flow of the device fabrication is included in Appendix A.

1. An n-type Si wafer of 4" of diameter and 500 μm of thickness is cleaned using a Radio Corporation America (RCA) necessary process, which removes ionic and organic contaminants and removes the thin oxide layer from the wafer. The wafer is then soft baked for 20 minutes at 110 °C
2. A positive photoresist is spin-coated on top of the wafer, and the wafer is then soft-baked at 90 °C for 3 minutes and then cooled down for 2 minutes. The wafer is placed in a mask aligner, and the wafer is then exposed to ultraviolet (UV) light using the first mask (Cavity). The wafer is then developed to reveal the areas in the wafer to be removed. The wafer is etched using deep reactive ion etching (DRIE) to form cavities of 6 μm in it.
3. The remains of the photoresist are removed using acetone, and the wafer is cleaned using RCA one more time. A layer of oxide is deposited on the wafer using plasma-enhanced chemical vapor deposition (PECVD). The cavities are overfilled, and the wafer is completely coated.
4. A chemical mechanical polishing (CMP) machine is used to flatten the surface of the wafer and remove any excess of oxide until it is only contained in the cavities.
5. A 1.5 μm Si_3N_4 layer is deposited on top of the wafer using PECVD. A photoresist is spin-coated on top of the wafer and the wafer as done in step 2. The wafer is placed in the mask aligner, and the wafer is then exposed to UV light using the second mask (Structures). The wafer is then developed to reveal the areas in the wafer to be removed. The residual stress can be characterized across the wafer after the Si_3N_4 film deposition.
6. The Si_3N_4 layer is patterned using reactive ion etching (RIE). This step will pattern the thin films, and cantilevers of the chip.

7. Metallic reflective markers of 0.5 µm of thickness are deposited using a lift-off process and the third mask (Markers) on the patterned Si_3N_4 film. In this same step, the second layer of the bimorph for the CTE measurements is deposited and patterned.
8. Finally, the devices are released from the oxide layer inside the cavity by using a Hydrofluoric acid (HF) wet etch.

The result from the fabrication is a whole chip with devices to characterize the thin film material at high temperatures. The fabrication process is purposefully designed for its easy adaptation to any material for the wafer and the thin film as long as they are compatible with the existing MEMS fabrication methodologies. These devices will take this methodology to the next stage allowing the upgrade of the simulations and the analytical model here proposed with the inclusion of the experimental thermal strain measured in-situ.

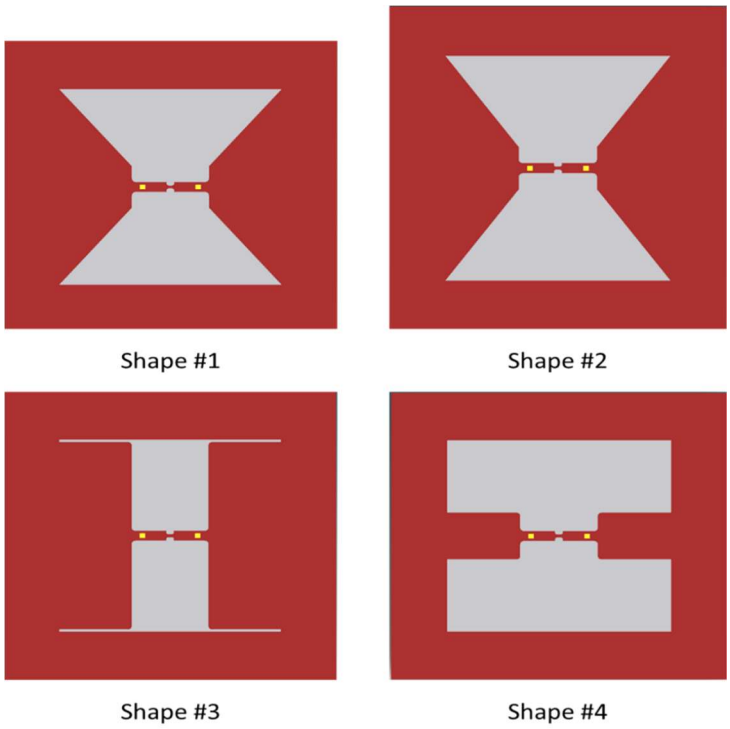

Figure 70. – Devices to test the fracture strength of Si_3N_4 thin films. The four proposed shapes for the next generation of devices are shown in this schematic.

Chapter 7
Conclusions and future work

7.1 Summary and conclusions

The overall objective of this thesis is to introduce a methodology t measure the fracture strength of thin films at high temperatures. The new methodology is presented by characterizing the fracture strength of a rich silicon nitride thin film. Besides, an FEA simulation and an analytical model that describes the behavior of the device under elastic circumstances during testing are developed. Finally, adequate improvements to the devices are introduced to improve the experiment and the results of the proposed approach.

After introducing the motivations and objectives in Chapter 1, and presenting a background review in Chapter 2, Chapter 3 introduced the devices used in this experiment and focused on three aspects for their design. The first aspect is the simplicity of the testing set up, which is addressed by using devices that provide their stress. A CTE mismatch approach is chosen as the stress source for the device, which only needs of temperature to be activated. The second aspect is the speed of the tests, for which devices with a stress concentration section of 3µm length and 3 µm width. The small dimensioning and thin thickness of 0.175 µm make for the fracture of the devices to be localized and quick. The third aspect is the number of tested devices per experiment, which for other approaches is of one; thus, arrays of devices are used due to the stress approach allows for multiple breaking temperatures to be recorded simultaneously. In this chapter, the thin-film material selection to silicon nitride and the range of temperature going from 20 ºC up to 1000 ºC are decided on based on the lack of information on the characterization of silicon nitride in this temperature range. The devices are designed to have three different shapes and lengths ranging from 152 µm to 217 µm for shape #1, from 134 µm to 199 µm for shape #2 and 98 µm to 172 µm for shape #3. The geometry variation is used to predict the temperature at which the devices will break; thus, assuring the devices to break before the 1000 ºC threshold. Finally, the fabrication process using LPCVD surface

micromachining was presented as an adequate process to manufacture these devices.

Chapter 4 presented the methodology used to determine the change of fracture strength with respect to temperature and geometry. The experiment to obtain the breaking temperature of each device is described, and the results were plotted, showing an increasing breaking temperature as the length of the devices reduces. A set of ten points of each shape is taken and modeled using CAD to simulate them in an FEA software, and a two-step analysis is done. The first step simulates the residual stress of the devices, measured as 0.39 GPa, and pre-stresses the thin film. The second step applies a change of temperature with a constant ramp from room temperature up to 1000 ºC. The obtained stress at the gage section of the devices during their breaking temperature is determined, and the results were plotted showing the change of fracture strength with respect to temperature and length. Contrary to what it was expected, the fracture strength increases with the increase of temperature. It was determined this is due to the simulation not accounting for the thermal deformation on the Si substrate at temperatures close and beyond 500ºC. In the case of the shape, the expected trend was obtained with the smallest devices having, on average, a higher fracture strength. It was also observed that the change of shape and length have a negligible impact compared to the temperature effect. The results for each shape were in the ranges of 0.24 GPa to 2.84 GPa for shape #1, 0.26 GPa to 2.98 GPa for shape #2 and 0.22 GPa to 2.18 GPa for shape #3. A Weibull distribution is used to determine a survival probability of ~90% for every device at their lowest fracture strength threshold.

Chapter 5 focused on the analytical proposed to describe the behavior of the device during the experiment. The analytical model is based on the stresses the device goes under along its X-axis. The model takes into consideration the geometry variation of the devices by introducing a shape factor into it. The mechanical properties used in this model, such as CTE and Young's modulus, are expressed in terms of the temperature; thus, the variation of these properties as temperature increases is considered. The model is finalized using the thermal

strain, and the residual stress from the thin film and the fracture strength is determined for the data obtained from the experiment. The advantage of the analytical model is the quick analysis of every obtained data point. The results from the analytical model showed the same trends as the simulation results, and these results were plotted showing the change of fracture strength with respect to temperature and length. Just as it was found for the simulation results, the fracture strength increases with the increase of temperature, which is due to the analytical model, just like the simulation, not accounting for the thermal deformation on the Si substrate at temperatures close and beyond 500 ºC. In the case of the shape, the same trend as with the simulation is obtained; however, it was also observed that the change of shape and length does have an impact on the magnitude of the fracture strength. The change from the relationship 1:1 of the width and length has a higher impact than the change of geometry in the results. The results for each shape were in the ranges of 0.7 GPa to 6.48 GPa for shape #1, 0.84 GPa to 6.48 GPa for shape #2 and 0.76 GPa to 6.07 GPa for shape #3. A Weibull distribution is used to determine a survival probability of over 90% for every device at their lowest fracture strength threshold. The results from both approaches are compared, and it is concluded that although the trend matches and the analytical model is a good representation of the experiment and the simulation, the change of length and shape have a heavier influence on the results of the analytical than those seen in the simulation. However, from both approaches, the same conclusion is reached, which is the need for strain monitoring in the devices to be able to characterize the strain evolution as the temperature rises properly.

Chapter 6 presented the necessary improvements in the next generation of devices to solve the addressed issues in the previous sections. An interferometric strain/displacement gage optical measurement is implemented into the devices for non-invasive in-situ strain monitoring. The strain is measured using reflective markers on the surface of the device and using a laser to create interferometric patterns from the refracted beams on both markers. The basic equations to verify the adaptability of the preexisting device to the ISDG approach are laid out, showing that a signal of 95.3% of the used intensity can be obtained from reflection

on Pt markers. The thickness for the thin films is set to be 1.5 μm in order to avoid the interference from noise due to reflection of the light on the areas not covered by reflective markers. A double gage device is used to preserve a small stress concentration section in the first gage section, while the second gage section is wide enough to deposit the metallic markers. The dimensions of the markers and their separation distance are defined based on the literature and the change of the resolution of the fringes to ensure the cameras can resolve the signal reflected from the markers. The markers are set to be square with a 10 μm length and 100 μm of separation. The length of the marker is varied up to 40 μm and the separation fluctuates from 80 μm to 133 μm to match a ±25% resolution change on the signal. The dimensions of the devices are adjusted to accommodate the markers, following the basic rules of the enclosure from other fabrication foundries. The devices are set to be square with a length of 200 μm with the length of the gage section that accommodates the markers changing. The devices are designed in the previously used three shapes, and to explore further the influence of geometry, a fourth shape is introduced with a smaller gripper section due to the device being handled as an array and not a standalone sample. The methodology is then extended to the design of a full chip with the purpose of characterizing the CTE and Young's modulus of the thin film material. Young's modulus cantilever beams are designed to be characterized using a piezo shaker and a vibrometer, the lengths of the beams are designed based on the frequencies at which the shaker can be actuated. The dimensions of the beams are 40 μm of width, 1.5 μm of thickness and a length ranged from 73 μm up to 163 μm. For the CTE devices, a single cantilever beam of silicon nitride and a bimorph of silicon nitride and platinum are proposed. The individual cantilever beams will allow for the measurement of the silicon nitride CTE and then use it to determine the CTE of platinum from the bimorph cantilevers for its use in result calculations. The beams have a thickness of 1.5 μm, a width of 40 μm a length of 200 μm up to 400 μm in increments of 25 μm for both the single cantilever and the first layer of the bimorph devices and the platinum layer on top is enclosed by 10 μm on every side with a 0.5 μm thickness. A fabrication process that can successfully manufacture all these structures is proposed, and its feasibility is shown by simulating it in a mask design software. This fabrication process is

designed to be adaptable to other materials, such as polysilicon and silicon carbide, making it an excellent alternative to the current approaches.

The presented work provides a direction for future work that would take this testing methodology to its next stage. The understanding of the missing parameters needed to improve this approach are determined in this thesis, a new iteration of devices to measure the fracture strength of thin films at high temperatures. Comparing the results obtained, repeatability, and cost of the methodology with other approaches would demonstrate its advantages compared to current methods.

7.2 Recommendations for future work

The success of the developed testing methodology will depend on the improvement of the devices. The new proposed devices need to be fabricated, and the optical interferometry set up to determine the strain in real-time during needs to be assembled. The optical approach might pose an issue to the measurement of more than one device per experiment. Thus, research on the feasibility of implementing a motorized base to move the devices during the test to be able to measure at least groups of five needs to be done. The testing of the CTE devices, Young's modulus devices, and measurement of the residual stress across the wafer will improve how these properties are accounted for in the simulations and the analytical model. Therefore, the testing setups for each of these devices have to be implemented.

The simulation can be improved by modeling the substrate in more detail and not only focus on the silicon nitride exclusively. The silicon substrate may be modeled as anisotropic, and while the silicon nitride can be assumed as an elastic domain in the simulation, the silicon substrate has to be modeled to account for non-elastic deformations as temperature increases above 500ºC. A simulation contained in one single study instead of doing two simulation steps would be beneficial for the straightforwardness of the methodology.

In terms of improving the analytical model, the strain monitoring will allow for the determination of the phenomena occurring on the thin film bridge as temperature increases. The goal for the future of this methodology is to be able to do every result analysis just with the analytical model, which allows the quick evaluation of every obtained data point. This approach can also allow for a better understanding of thermal deformation on silicon and creep.

This test must be done with other combinations of substrate/thin-film materials to broaden the applications of the methodology. The method has the potential of being a fracture test or a creep test depending on the temperature profile used and the combination of the materials. Holding the temperature constant for a group of devices while recording the strain over extended times is something achievable by these new proposed devices; thus, this methodology, if continued, can be a powerful tool for material characterization at high temperatures.

Bibliography

[1] A. Navarrete, A. Ghannoum, and P. Nieva, “Creep of brittle MEMS structural materials: A review.”

[2] A. Navarrete, E. Brace, and P. Nieva, “A study of the fracture strength of silicon nitride thin films at high temperatures by means of the difference of coefficient of thermal expansion.”

[3] S. W. Freiman and J. J. M. Jr, *The Fracture of Brittle Materials: Testing and Analysis*. John Wiley & Sons, 2019.

[4] K. D. Wise, “Integrated sensors: interfacing electronics to a non-electronic world,” *Sens. Actuators*, vol. 2, pp. 229–237, Jan. 1981, doi: 10.1016/0250-6874(81)80043-1.

[5] S. Middelhoek and A. C. Hoogerwerf, “Smart sensors: when and where?,” *Sens. Actuators*, vol. 8, no. 1, pp. 39–48, Sep. 1985, doi: 10.1016/0250-6874(85)80023-8.

[6] S. D. Senturia, “Microsensors vs. integrated circuits: a study in contrasts,” in *International Technical Digest on Electron Devices Meeting*, 1989, pp. 3–7, doi: 10.1109/IEDM.1989.74217.

[7] J. Jeong, S. Chung, S. H. Lee, and D. Kwon, “Evaluation of elastic properties and temperature effects in Si thin films using an electrostatic microresonator,” *J. Microelectromechanical Syst.*, vol. 12, no. 4, pp. 524–530, Aug. 2003, doi: 10.1109/JMEMS.2003.811733.

[8] W. Spengen, R. Modlinski, R. Puers, and A. Jourdain, “Failure Mechanisms in MEMS/NEMS Devices,” in *Springer Handbook of Nanotechnology*, B. Bhushan, Ed. Berlin, Heidelberg: Springer Berlin Heidelberg, 2007, pp. 1663–1684.

[9] H. E. Evans, *Mechanisms of Creep Fracture*. Elsevier Applied Science, 1984.

[10] M. Mehregany, “SiC MEMS: opportunities and challenges for applications in harsh environments - ScienceDirect.” [Online]. Available: https://www.sciencedirect.com/science/article/pii/S0257897299003746. [Accessed: 02-Apr-2019].

[11] F. W. DelRio, R. F. Cook, and B. L. Boyce, “Fracture strength of micro- and nano-scale silicon components,” *Appl. Phys. Rev.*, vol. 2, no. 2, p. 021303, May 2015, doi: 10.1063/1.4919540.

[12] A. L. Hartzell, M. G. da Silva, and H. Shea, *MEMS Reliability*. Springer US, 2011.

[13] “Reliability and Fatigue Analysis in Cantilever-Based MEMS Devices Operating in Harsh Environments.” [Online]. Available: https://www.hindawi.com/journals/jqre/2014/987847/abs/. [Accessed: 01-Oct-2019].

[14] P. J. Burkhardt and R. F. Marvel, “Thermal Expansion of Sputtered Silicon Nitride Films,” *J. Electrochem. Soc.*, vol. 116, no. 6, pp. 864–866, Jun. 1969, doi: 10.1149/1.2412081.

[15] W. N. Sharpe, M. A. Eby, and G. Coles, “Effect of Temperature on Mechanical Properties of Polysilicon,” in *Transducers ’01 Eurosensors XV*, 2001, pp. 1338–1341.

[16] K. M. Nikbin, “The Fracture Mechanics Concepts of Creep and Creep/Fatigue Crack Growth,” in *Component Reliability under Creep-Fatigue Conditions*, 1998, pp. 177–242.

[17] F. T. Hartley, S. Arney, and F. Sexton, “Chapter 09: Microsystems reliability, test and metrology,” ITRS, pp. 337–394.

[18] R. Swaminathan, H. Bhaskaran, P. A. Sandborn, G. Subramanian, M. A. Deeds, and K. R. Cochran, “Reliability assessment of delamination in chip-to-chip bonded MEMS packaging,” *IEEE Trans. Adv. Packag.*, vol. 26, no. 2, pp. 141–151, May 2003, doi: 10.1109/TADVP.2003.817344.

[19] A. R. Maligno, D. C. Whalley, and V. V. Silberschmidt, “Thermal fatigue life estimation and delamination mechanics studies of multilayered MEMS structures,” *Microelectron. Reliab.*, vol. 52, no. 8, pp. 1665–1678, Aug. 2012, doi: 10.1016/j.microrel.2012.03.023.

[20] W. Merlijn van Spengen, “MEMS reliability from a failure mechanisms perspective,” *Microelectron. Reliab.*, vol. 43, no. 7, pp. 1049–1060, Jul. 2003, doi: 10.1016/S0026-2714(03)00119-7.
[21] S. Kamiya, Y. Ikeda, J. Gaspar, and O. Paul, “Effect of humidity and temperature on the fatigue behavior of polysilicon thin film,” *Sens. Actuators Phys.*, vol. 170, no. 1, pp. 187–195, Nov. 2011, doi: 10.1016/j.sna.2011.06.007.
[22] J. A. Walraven, “Failure Analysis Issues in Microelectromechanical Systems (MEMS),” *Microelectron. Reliab.*, vol. 45, no. 9, pp. 1750–1757, Sep. 2005, doi: 10.1016/j.microrel.2005.07.088.
[23] D. J. Fonseca and M. Sequera, “On MEMS Reliability and Failure Mechanisms,” *Journal of Quality and Reliability Engineering*, 2011. [Online]. Available: https://www.hindawi.com/journals/jqre/2011/820243/. [Accessed: 21-May-2019].
[24] N. Lobontiu and E. Garcia, *Mechanics of Microelectromechanical Systems*. Springer US, 2005.
[25] A. Ettouhami, A. Essaid, N. Ouakrim, L. Michel, and M. Limouri, “Thermal buckling of silicon capacitive pressure sensor,” *Sens. Actuators Phys.*, vol. 57, no. 3, pp. 167–171, Dec. 1996, doi: 10.1016/S0924-4247(97)80109-4.
[26] K. Tuck, A. Jungen, A. Geisberger, M. Ellis, and G. Skidmore, “A Study of Creep in Polysilicon MEMS Devices,” *J. Eng. Mater. Technol.*, vol. 127, no. 1, pp. 90–96, Feb. 2005, doi: 10.1115/1.1839214.
[27] Y. Li and Z. Jiang, “An Overview of Reliability and Failure Mode Analysis of Microelectromechanical Systems (MEMS),” in *Handbook of Performability Engineering*, K. B. Misra, Ed. London: Springer London, 2008, pp. 953–966.
[28] N. E. Dowling, *Mechanical behavior of materials: engineering methods for deformation, fracture, and fatigue*, 4th ed. Boston, MA: Pearson, 2012.
[29] E. Rocha-Rangel, “Fracture Toughness Determinations by Means of Indentation Fracture,” *Nanocomposites Unique Prop. Appl. Med. Ind.*, Aug. 2011, doi: 10.5772/18127.
[30] J. Pelleg, “Creep in Ceramics,” in *Creep in Ceramics*, J. Pelleg, Ed. Cham: Springer International Publishing, 2017, pp. 41–61.
[31] N. Pugno, B. Peng, and H. D. Espinosa, “Predictions of strength in MEMS components with defects—a novel experimental–theoretical approach,” *Int. J. Solids Struct.*, vol. 42, no. 2, pp. 647–661, Jan. 2005, doi: 10.1016/j.ijsolstr.2004.06.026.
[32] “Fracture strength of ultrananocrystalline diamond thin films—identification of Weibull parameters,” *J. Appl. Phys.*, vol. 94, no. 9, pp. 6076–6084, Oct. 2003, doi: 10.1063/1.1613372.
[33] D. Kececioglu, *Reliability Engineering Handbook (Vol. 1)*. Upper Saddle River, NJ, USA: Prentice-Hall, Inc., 1991.
[34] S. Nakao, T. Ando, M. Shikida, and K. Sato, “Mechanical properties of a micron-sized SCS film in a high-temperature environment,” *J. Micromechanics Microengineering*, vol. 16, no. 4, pp. 715–720, 2006, doi: 10.1088/0960-1317/16/4/007.
[35] T. Namazu and Y. Isono, “Fatigue Life Prediction Criterion for Micro–Nanoscale Single-Crystal Silicon Structures,” *J. Microelectromechanical Syst.*, vol. 18, no. 1, pp. 129–137, Feb. 2009, doi: 10.1109/JMEMS.2008.2008583.
[36] M. Elhebeary and M. T. A. Saif, “A novel MEMS stage for in-situ thermomechanical testing of single crystal silicon microbeams under bending,” *Extreme Mech. Lett.*, vol. 23, pp. 1–8, Sep. 2018, doi: 10.1016/j.eml.2018.06.009.
[37] F. R. N. Nabarro, F. de Villiers, and F. de Villiers, *Physics Of Creep And Creep-Resistant Alloys*. CRC Press, 2018.

[38] A. H. Cottrell, “The time laws of creep,” *J. Mech. Phys. Solids*, vol. 1, no. 1, pp. 53–63, Oct. 1952, doi: 10.1016/0022-5096(52)90006-9.
[39] O. H. Wyatt, “Transient Creep in Pure Metals,” *Nature*, vol. 167, no. 4256, p. 866, May 1951, doi: 10.1038/167866a0.
[40] S. K. Yao, D. H. Xu, B. Xiong, and Y. L. Wang, “The plastic and creep behavior of silicon microstructure at high temperature,” in *2013 Transducers Eurosensors XXVII: The 17th International Conference on Solid-State Sensors, Actuators and Microsystems (TRANSDUCERS EUROSENSORS XXVII)*, 2013, pp. 159–162, doi: 10.1109/Transducers.2013.6626726.
[41] M. van Gils, J. Bielen, and G. McDonald, “Evaluation of Creep in RF MEMS Devices,” in *2007 International Conference on Thermal, Mechanical and Multi-Physics Simulation Experiments in Microelectronics and Micro-Systems. EuroSime 2007*, 2007, pp. 1–6, doi: 10.1109/ESIME.2007.360033.
[42] B. Derby and M. F. Ashby, “Power-laws, and the A□n correlation in creep - ScienceDirect.” [Online]. Available: https://www.sciencedirect.com/science/article/pii/0036974884901820. [Accessed: 02-Apr-2019].
[43] J. Ginsztler and R. P. Skelton, Eds., *Component Reliability under Creep-Fatigue Conditions*. Wien: Springer-Verlag, 1998.
[44] J. J. Meléndez-Martínez and A. Domínguez-Rodríguez, “Creep of silicon nitride,” *Prog. Mater. Sci.*, vol. 49, no. 1, pp. 19–107, Jan. 2004, doi: 10.1016/S0079-6425(03)00020-3.
[45] C. H. Carter, R. F. Davis, and J. Bentley, “Kinetics and Mechanisms of High-Temperature Creep in Silicon Carbide: I, Reaction-Bonded,” *J. Am. Ceram. Soc.*, vol. 67, no. 6, pp. 409–417, 1984, doi: 10.1111/j.1151-2916.1984.tb19726.x.
[46] “Dislocation Motion - an overview | ScienceDirect Topics.” [Online]. Available: https://www.sciencedirect.com/topics/engineering/dislocation-motion. [Accessed: 11-Oct-2019].
[47] W. N. Sharpe, “Tensile Testing of MEMS Materials at High Temperatures,” *Applied Mechanics and Materials*, 2005. [Online]. Available: https://www.scientific.net/AMM.3-4.59. [Accessed: 02-Apr-2019].
[48] A. A. N. Gonzalez, E. Brace, and P. Nieva, “Size and Shape Effect in the Determination of the Fracture Strength of Silicon Nitride in MEMS Structures at High Temperatures,” in *2018 IEEE 68th Electronic Components and Technology Conference (ECTC)*, 2018, pp. 2457–2463, doi: 10.1109/ECTC.2018.00370.
[49] P. Nieva, H. Tada, P. Zavracky, G. Adams, I. Miaoulis, and P. Wong, “Mechanical and Thermophysical Properties of Silicon Nitride Thin Films at High Temperatures Using In-Situ Mems Temperature Sensors,” in *Symposium AA – Materials Science of Microelectromechanical Systems (MEMS)…*, 1998, vol. 546, p. 97 (6 pages), doi: 10.1557/PROC-546-97.
[50] P. Nieva, “The Analysis and Performance of MICROMECHANICAL TEMPERATURE SENSORS designed for RAPID THERMAL PROCESSING,” MSc, Northeastern University, Boston, Massachusetts, 1999.
[51] A. Navarrete and P. Nieva, “Determination of the fracture strength of silicon nitride thin films at high temperatures through finite element analysis.”
[52] N. Ono, K. Kitamura, K. Nakajima, and Y. Shimanuki, “Measurement of Young’s Modulus of Silicon Single Crystal at High Temperature and Its Dependency on Boron Concentration Using the Flexural Vibration Method,” *Jpn. J. Appl. Phys.*, vol. 39, no. 2R, p. 368, Feb. 2000, doi: 10.1143/JJAP.39.368.

[53] R. J. Bruls, H. T. Hintzen, G. de With, and R. Metselaar, "The temperature dependence of the Young's modulus of MgSiN2, AlN and Si3N4," *J. Eur. Ceram. Soc.*, vol. 21, no. 3, pp. 263–268, Mar. 2001, doi: 10.1016/S0955-2219(00)00210-7.
[54] T. Tsuchiya, "Tensile testing of silicon thin films," *Fatigue Fract. Eng. Mater. Struct.*, vol. 28, no. 8, pp. 665–674, 2005, doi: 10.1111/j.1460-2695.2005.00910.x.
[55] G. F. Cardinale and R. W. Tustison, "Fracture strength and biaxial modulus measurement of plasma silicon nitride films," *Thin Solid Films*, vol. 207, no. 1, pp. 126–130, Jan. 1992, doi: 10.1016/0040-6090(92)90112-O.
[56] *Silicon Nitride for Microelectronic Applications - Part 1 | John T. Milek | Springer*. .
[57] J. Qian *et al.*, "Yield Strength of α-Silicon Nitride at High Pressure and High Temperature," *J. Am. Ceram. Soc.*, vol. 88, no. 4, pp. 903–906, 2005, doi: 10.1111/j.1551-2916.2005.00163.x.
[58] W. N. Sharpe, K. M. Jackson, K. J. Hemker, and Z. Xie, "Effect of specimen size on Young's modulus and fracture strength of polysilicon," *J. Microelectromechanical Syst.*, vol. 10, no. 3, pp. 317–326, Sep. 2001, doi: 10.1109/84.946774.
[59] T. Tsuchiya, O. Tabata, J. Sakata, and Y. Taga, "Specimen size effect on tensile strength of surface-micromachined polycrystalline silicon thin films," *J. Microelectromechanical Syst.*, vol. 7, no. 1, pp. 106–113, Mar. 1998, doi: 10.1109/84.661392.
[60] W. Jiang, D. Xu, S. Yao, B. Xiong, and Y. Wang, "Simulation of plastic deformation of sculptured diaphragm silicon microstructure," *Microelectron. Eng.*, vol. 152, pp. 26–34, Feb. 2016, doi: 10.1016/j.mee.2015.12.011.
[61] J. Castaing, P. Veyssière, L. P. Kubin, and J. Rabier, "The plastic deformation of silicon between 300°C and 600°C," *Philos. Mag. A*, vol. 44, no. 6, pp. 1407–1413, Dec. 1981, doi: 10.1080/01418618108235821.
[62] S. Korte, J. S. Barnard, R. J. Stearn, and W. J. Clegg, "Deformation of silicon – Insights from microcompression testing at 25–500°C," *Int. J. Plast.*, vol. 27, no. 11, pp. 1853–1866, Nov. 2011, doi: 10.1016/j.ijplas.2011.05.009.
[63] W. N. Sharpe, "An interferometric strain-displacement measurement system," Aug. 1989.
[64] W. N. Sharpe, "Mechanical properties of MEMS materials," in *2001 International Semiconductor Device Research Symposium. Symposium Proceedings (Cat. No.01EX497)*, 2001, pp. 416–417, doi: 10.1109/ISDRS.2001.984532.
[65] Francis A. Jenkins & Harvey E. White, *Fundamentals of Optics*. .
[66] G. J.r, P. L.n, and W. P. M. N. S.-H.p, "Residual Stress Dependency on Wafer Location of Thin Film PECVD Silicon Nitride," *TechConnect Briefs*, vol. 1, no. 2011, pp. 108–111, Jun. 2011.
[67] A. M. Torgalkar, "A resonance frequency technique to determine elastic modulus of hydroxyapatite," *J. Biomed. Mater. Res.*, vol. 13, no. 6, pp. 907–920, Nov. 1979, doi: 10.1002/jbm.820130609.
[68] W. Fang, H.-C. Tsai, and C.-Y. Lo, "Determining thermal expansion coefficients of thin films using micromachined cantilevers," *Sens. Actuators Phys.*, vol. 77, no. 1, pp. 21–27, Sep. 1999, doi: 10.1016/S0924-4247(99)00019-9.

Appendix A

Fabrication process flow

1

2

3

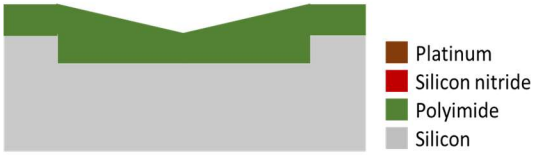

4

5

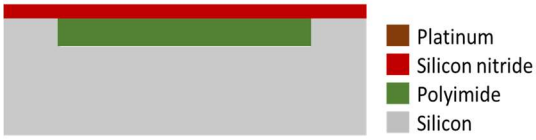

6

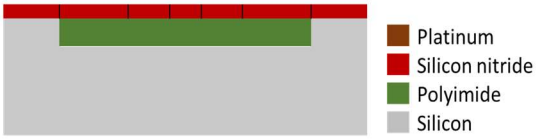

7

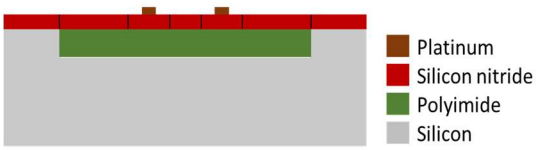

8